Search for 3rd Generation Vector Leptoquarks in the Di-τ Di-jet Channel in $p\bar{p}$ Collisions at $\sqrt{s} = 1.96$ TeV

By

STANLEY SCOTT FORRESTER

B.S. (University of the State of New York, Albany) 1987

M.S. (San Francisco State University) 2001

DISSERTATION

Submitted in partial satisfaction of the requirements for the degree of

DOCTOR OF PHILOSOPHY

in

Physics

in the

OFFICE OF GRADUATE STUDIES

of the

UNIVERSITY OF CALIFORNIA

DAVIS

Approved:

_____

_____

_____

Committee in Charge

2006

Curriculum Vitae

Stan Forrester joined the US Navy as a nuclear power plant operator in 1985 and received his first introduction to physics at the Navy's Nuclear Power School (NNPS). In 1989, while on active duty he completed a Bachelor of Science Degree in Liberal Arts from the University of the State of New York, Albany. He left the service in 1998 and returned to school. While at San Francisco State University he was selected the Mario Savio Fellow for the year 1999 and completed a Master of Science in Physics in 2000. Upon graduation he was accepted to the University of California, Davis where he pursues his research at the Fermi National Accelerator Laboratory under the direction of Professor Maxwell Chertok. Stan Forrester is an 11 year Navy veteran, a husband, a father and a damn fine cook.

Acknowledgments

I would like to extend my most sincere thanks to my advisor, Maxwell Chertok, and to our group leader, Richard Lander, for their advice, support and guidance. I would also like to acknowledge several colleagues: Alexei Safonov, Aron Soha, John Rodgers Smith and Sasha Baroiant for help over the rough spots. To my fellow vector leptoquarkers at other institutions: Takashi Akimoto, Teruki Kamon, Yukihiro Kato, Sung-Won Lee and Soushi Tsuno. I would also like to thank my instructors past and present at the University of California, Davis and San Francisco State University: John Burke, Susan Lea and Ronald Adler. I would also like to acknowledge my first physics instructor Ensign Zabloki of at the Navy's Nuclear Power School. To my parents Paul and Mary Forrester for their support and encouragement. To Ruth and Timmy because without you this entire enterprise would have been pointless.

Abstract

We search for third generation vector leptoquarks ($VLQ3$) produced in colliding $p\bar{p}$ beams operating at $\sqrt{s} = 1.96$ TeV at the CDF experiment in Run II of the Fermilab Tevatron. We use $322\ pb^{-1}$ of data to search for the $VLQ3$ signal in the di-tau plus di-jet channel. For the first time, the full matrix element is used in the Monte Carlo simulation of this signal. With no events observed in the signal region, we set a 95% C.L. upper limit on the $VLQ3$ pair production cross section of $\sigma < 344fb$, assuming Yang-Mills couplings and $Br(VLQ3 \rightarrow b\tau) = 1$, and a lower limit on the $VLQ3$ mass of $m_{VLQ3} > 317\ \mathrm{GeV}/c^2$. If theoretical uncertainties on the cross section are applied in the least favorable manner the results are $\sigma < 360fb$ and $m_{VLQ3} > 294\ \mathrm{GeV}/c^2$. The Minimal coupling $VLQ3$ result is an upper limit on the cross section of $\sigma < 493fb$ ($\sigma < 610fb$) and the lower limit on the mass is $m_{VLQ3} > 251\ \mathrm{GeV}/c^2$ ($m_{VLQ3} > 223\ \mathrm{GeV}/c^2$) for the nominal ($1\sigma$ varied) theoretical expectation.

Contents

List of Figures x

List of Tables xiv

1 Introduction **1**

2 Theoretical Perspective **4**

2.1 The Standard Model 4

2.1.1 The Standard Model Particles 5

2.1.2 Symmetry 8

2.1.3 Global Gauge Transformations 9

2.1.4 Local Gauge Transformations 10

2.1.5 Quantum Chromodynamics 13

2.1.6 Electroweak Unification 15

2.1.7 Spontaneous Symmetry Breaking 19

2.2 Beyond the Standard Model 23

2.2.1 Unification 23

2.2.2 Leptoquarks 25

3 GRACE/GR@PPA **31**

3.1 Extension of GRACE to $pp/p\bar{p}$ collisions 31

3.2 Total Cross Section 33
3.3 Anomalous Couplings 35

4 Experimental Apparatus **37**
4.1 The Tevatron Collider 38
4.1.1 Accelerator Complex 39
4.1.2 The Antiproton Source 39
4.1.3 Tevatron Accelerator 42
4.2 CDF 46
4.2.1 Tracking 50
4.2.1.1 The Silicon Detector 54
4.2.1.2 The Central Outer Tracker 67
4.2.2 Calorimetry 70
4.2.3 Muon Systems 74
4.2.4 Luminosity Counters 77
4.3 Data Acquisition 78
4.3.1 Level-1 Trigger System 79
4.3.2 Level-2 Trigger System 80
4.3.3 Level-3 Trigger System 81
4.3.4 Data Acquisition 81

5 Silicon Operations **84**
5.1 Silicon Organization 85
5.2 Silicon Maintenance Group 89
5.3 Power Supplies and Interlocks 90
5.4 Monitoring 91
5.5 Wire Bond Failure 91

5.6 Radiation and Longevity 92

6 Trigger and Dataset **98**

6.1 Overview 99

6.2 Electron + Track Trigger 101

6.3 Muon + Track Trigger 102

6.4 Signal Monte Carlo 103

7 Offline Selection **106**

7.1 Offline Efficiency 107

7.2 Geometric Acceptance 109

7.2.1 Electron Acceptance 109

7.2.2 Muon Acceptance 112

7.2.3 Hadronic Tau Acceptance 112

7.2.4 Lepton-Tau Separation 113

7.2.5 Scale Factors 113

7.3 Lepton-Jet Separation 115

7.4 Identification Requirements 115

7.4.1 Jets 115

7.4.2 Electron Identification 116

7.4.3 Muon Identification 117

7.4.4 Lepton Isolation 118

7.4.5 Lepton Trigger Efficiency 118

7.4.6 Tau-Jet Separation 120

7.4.7 Tau Identification 120

7.4.8 Tau Isolation 122

8 Backgrounds **124**

8.1 Top Quark Pairs 125

8.2 $Z^0/\gamma \to \tau^+\tau^-$ 125

8.3 $Z^0/\gamma \to e^+e^-$ and $Z^0/\gamma \to \mu^+\mu^-$ 126

8.4 $W + jets$ 126

8.5 Diboson 128

8.6 QCD 128

8.7 $\gamma + jets$ 130

9 Event Level Selection **133**

9.1 Opposite Sign 134

9.2 Conversion Removal 134

9.3 Cosmic Removal 135

9.4 Z Mass Window Removal 135

9.5 $\not\!\!E_T$ and $\not\!\!E_T$ Corrections 136

9.6 Control Regions 139

9.7 H_T Cut 140

9.8 Jet Multiplicity 144

9.9 Control Region Checks 147

10 Systematic Uncertainties **164**

10.1 Luminosity Measurement 164

10.2 Production Cross Section 164

10.3 Parton Distribution Functions 165

10.4 Jet Energy Scale 167

10.5 Initial and Final State Gluon Radiation 174

10.6 Missing Transverse Energy, $\not\!\!E_T$ 174

10.7 Summary 175

11 Results **179**

11.1 SAFE Region 181

11.2 Signal Region 181

11.3 Signal Extraction 182

11.4 Summary 185

12 Prospects **195**

12.1 CDF at Large Integrated Luminosities 195

12.2 Large Hadron Collider 197

13 Conclusions **199**

List of Figures

2.1 Diagram of a boson (γ) exchange between two electrons. 8

2.2 Higgs Potential 21

2.3 Evolution of α_S. α_W and α_e under SM and MSSM. 24

2.4 Higgs self energy corrections diagrams 25

2.5 Leptoquark production from $q\bar{q}$ fusion. 28

2.6 Feynman diagrams for $VLQ3$ production, gluon-gluon fusion. . . . 29

3.1 Pair Production Cross Section 36

4.1 Fermilab Accelerator complex. 40

4.2 Effect of electron cooling on the antiproton momentum profile. . . 42

4.3 Aerial view of the Fermilab Tevatron and Accelerator complex. . . 43

4.4 Tevatron Initial Instantaneous Luminosities 45

4.5 Tevatron Weekly Integrated Luminosities 46

4.6 Primary vertex z_0 position. 48

4.7 The CDF coordinate system with respect to the Tevatron. 49

4.8 An illustration of the η coordinate of various components. 50

4.9 CDF detector longitudinal view. 51

4.10 CDF detector in the assembly hall during construction. 52

4.11 Placement of CDF tracking system components 56

4.12 Radial placement of Silicon Detector detector components. 57
4.13 Layer 00 end view 58
4.14 SVX II during assembly 59
4.15 Silicon readout electronics. 63
4.16 Photograph of the SVX3d chip 64
4.17 Port Card shown with five mounted DOIMs 64
4.18 Schematic of the DOIM system 65
4.19 Photograph of transmitter DOIM (Port Card end) 66
4.20 Photograph of receiver DOIM (FIB end) 66
4.21 60° of the East COT endplate. 68
4.22 Layout of a single COT supercell. 70
4.23 Particle adsorption is the various instruments in CDF. 74
4.24 Muon systems η and ϕ coverage 76
4.25 Various cross sections encountered at CDF. 82
4.26 CDF deadtimeless trigger system. 83

5.1 Silicon hardware integration fraction. 86
5.2 Silicon Detector Working Group Logo 87
5.3 Three photographs of illustrating resonant wire-bond failure. . . . 93
5.4 SVX Layer 0 required depletion voltage as a function of integrated luminosity. 96
5.5 Integrated radiation dose to silicon detector. 97

7.1 Tau track isolation cones 123

8.1 Distribution of ISO for QCD backgrounds for $e\tau_h$ channel 130
8.2 I_{track} Sideband (2 to 10 GeV) for QCD backgrounds ($\mu\tau_h$) 131

9.1 Illustration of the Signal, Safety and Control regions. 140
9.2 H_T 320 GeV/c^2 $VLQ3$ signal MC vs background. 141
9.3 $S/\sqrt{S+B}$ vs H_T 143
9.4 Exponential fit to backgrounds in H_T distribution, $\tau_e\tau_h$. 144
9.5 Exponential fit to backgrounds in H_T distribution, $\tau_\mu\tau_h$. 145
9.6 Mass dependence of geometric acceptance. 147
9.7 Electron E_T in the Control Regions 149
9.8 Muon p_T in the Control Regions 150
9.9 Hadronic tau p_T in the Control Regions ($e\tau_h$) 151
9.10 Hadronic tau p_T in the Control Regions ($\mu\tau_h$) 152
9.11 Leading jet E_T in the Control Regions ($e\tau_h$) 153
9.12 Leading jet E_T in the Control Regions ($\mu\tau_h$) 154
9.13 Second jet E_T in the Control Regions 155
9.14 Missing E_T in the Control Regions ($e\tau_h$) 156
9.15 Missing E_T in the Control Regions ($\mu\tau_h$) 157
9.16 M_T in the Control Regions ($e\tau_h$) 158
9.17 M_T in the Control Regions ($\mu\tau_h$) 159
9.18 H_T in the Control Regions ($e\tau_h$) 160
9.19 H_T in the Control Regions ($\mu\tau_h$) 161
9.20 Number of tau prongs in the Control Regions ($e\tau_h$) 162
9.21 Number of tau prongs in the Control Regions ($\mu\tau_h$) 163

10.1 Z + Jets systematic effect on Cross section (Yang-Mills) 170
10.2 Zoomed Z + Jets systematic plot (Yang-Mils) 171
10.3 Z + Jets systematic effect on cross section (Minimal Coupling). . 172
10.4 Zoomed Z + Jet systematics plot (Minimal Coupling). 173

11.1 Lepton p_T or E_T in the Safety Region 186
11.2 Hadronic tau p_T in the Safety Region 187
11.3 Leading jet E_T in the Safety Region 188
11.4 Second jet E_T in the Safety Region 189
11.5 Missing E_T in the Safety Region 190
11.6 M_T in the Safety Region 191
11.7 H_T in the Safety Region 192
11.8 Number of tau prongs in the Safety Region 193
11.9 Fit Results 194

List of Tables

2.1 The Standard Model fermions 5

2.2 The Standard Model bosons 5

2.3 Quantum numbers for 1st gen. leptons. 17

2.4 Quark quantum numbers. 17

2.5 Leptoquark Species 27

3.1 Cross Section for vector leptoquark pair production 35

4.1 Silicon sensor properties by SVX II layer. 60

4.2 Calorimeter resolution parameters. 72

4.3 Calorimeter materials. 73

7.1 Summary of $\tau_e\tau_h$ Acceptance at $m_{VLQ3} = 320$ GeV/c^2 110

7.2 Summary of $\tau_\mu\tau_h$ Acceptance at $m_{VLQ3} = 320$ GeV/c^2 111

7.3 Electron Tau Separation and Isolation Efficiencies 113

7.4 Muon Tau Separation and Isolation Efficiencies 114

7.5 Electron Identification Requirements and Efficiencies 117

7.6 Muon Identification Requirements and Efficiencies 118

7.7 Trigger Efficiencies 119

7.8 Tau ID Requirements and Efficiencies $\tau_e\tau_h$ 121

7.9 Tau ID Requirements and Efficiencies, $\tau_\mu\tau_h$ 121

8.1 Lepton fake rates from jets. 124
8.2 Scale Factors for W + jets Background 127
8.3 Background Sample Details 132

9.1 Grand Summary of Efficiencies 146
9.2 Summary of Efficiencies Near Mass Limit 146

10.1 Systematic Uncertainty on Full Selection Due to PDF Choice . . . 168
10.2 Summary of Systematics on Cross Section 169
10.3 Systematic Uncertainty Due to Jet Energy Scale 176
10.4 Systematic Uncertainty Due to Missing Transverse Energy 176
10.5 Systematics Summary for Electron Channel 177
10.6 Systematics Summary for Muon Channel 178

11.1 Regions Defined for the Fitting Procedure 182
11.2 Mass and Cross Section Limit Results 185

Chapter 1

Introduction

"O, God Thy Sea Is So Great And My Boat Is So Small."

Prayer of the Breton fisherman

There are many ways that one can construct a theory that explains how the universe is put together, but there is only one way in which it actually is put together. All of the clever mechanisms by which we seek to unify our understanding of the structure and working of the universe can be bought about must be tested against the original. Few of these theories survive contact with experiment. Currently high energy experimental particle physics and exotic particle physics is theory driven. We look for the particles that various theoretical frameworks indicate must exist. With that perspective, I will simply state that high energy experimental particle physics and exotic particle searches in particular, are if not about slaying theoretical dragons, are at least about removing the label *Terra Incognito* from the energy scales as they become accessible.

In the early 1990's five quarks had been experimentally observed and a sixth, the top quark, was expected to complete the inventory of the quark model. The

discovery of the top quark [1] confirmed a long suspected symmetry between the structure of the quark and lepton sectors of the Standard Model. A discovery is a rather dramatic example of experiment feeding back into the theoretical model, but searches prior to the actual observation were no less important constraints on the theories of the day.

This analysis presents the world's best mass and cross section limits for one particular mechanism by which the quark and lepton sectors of the Standard model could unify at a sufficient energy. The 3rd generation vector leptoquarks arise from several different theoretical models and the constraints from this study feed directly back into the development of those models. It should also be stated that while vector leptoquark searches have been conducted before, this analysis for the first time probes the leptoquark sector above the mass of top quark.

The search for vector leptoquarks in the 3rd generation is documented here. The chapter you are reading is the introduction. Chapter 2 begins with a very brief overview of the Standard Model of particle physics. The concepts of Gauge theories and spontaneous symmetry breaking are discussed. Physics beyond the Standard Model, or rather avenues to be explored, are covered and a theoretical motivation for the search for vector leptoquarks in the 3rd generation is presented. This search required the application of a matrix element generator to the simulation of vector leptoquarks in the CDF environment. GRACE/GR@PPA is the result and Chapter 3 covers the relevant details of the new matrix element generator used in the $VLQ3$ search. The physical apparatus of the CDF detector and the Tevatron are the subject of Experimental Apparatus, Chapter 4. The Silicon Operations, Chapter 5 covers the maintenance and operational details required to ensure high quality data from that single instrument. This section is included to give the reader an idea of the full time effort required to keep the

CDF detector running and writing data to tape. Maintenance and upkeep of the Silicon Detector was also the service project of the author for nearly 2 years. The data and the on-line means of selecting events to be written to the various data streams is the subject of Chapter 6. One of those data streams feeds the *Lepton + Track* dataset applicable to this analysis. Chapter 7 covers the offline selection of events and the criteria by which the physical limitations of the CDF detector and the limitations of particle candidate reconstruction are accounted for. The various backgrounds which could hide or even mimic our $VLQ3$ signal are the detailed in Chapter 8. Event level selection is where we first begin to consider the global quality of the events, as discussed in Chapter 9. This chapter includes some discussion of background suppression. Chapter 10 covers the systematic uncertainties associated with this analysis and the negative result of the search is discussed in Chapter 11. The prospects for $VLQ3$ searches both in the future of CDF and at the Large Hadron Collider in CERN Switzerland are covered in Chapter 12.

Chapter 2

Theoretical Perspective

This chapter focuses on the Standard Model (SM) description of high energy particle physics. We review both the particles which make up the Standard Model and its theoretical underpinnings. This is followed by a very brief introduction to symmetry and spontaneous symmetry breaking. A review of the Standard Model as it stands today provides the motivation for studies into physics beyond the Standard Model where we discuss unification in general. Lastly a very specific means of unifying the quark and leptonic realms of physics is discussed in the form of leptoquarks, specifically vector leptoquarks in the 3rd generation, $VLQ3$.

2.1 The Standard Model

The Standard Model is the effective low energy theory of particle physics encompassing our current understanding of how the universe works at the smallest scale [2, 3, 4]. While a deeper understanding of the Standard Model is rooted in the principles of symmetry a brief survey the particle content of the Standard Model is in order.

	Quarks		Leptons	
Charge Q	+ $\frac{2}{3}$	- $\frac{1}{3}$	-1	0
1st Generation	u	d	e	ν_e
2nd Generation	c	s	μ	ν_μ
3rd Generation	t	b	τ	ν_τ

Table 2.1: The Standard Model fermions arranged into rows of like generation and columns of like electrical charge.

	Charge Q	Mass (GeV/c^2)	Mediates Force	Symmetry Group
Photon γ	0	0	electromagnetic	$U(1)$
$W^{\pm}$	± 1	80.4	Weak	$SU(2)$
Z^0	0	91.187	Weak	$SU(2)$
gluon	0	0	Strong	$SU(3)$

Table 2.2: The Standard Model bosons for the electromagnetic, weak nuclear and strong nuclear forces. The SM symmetry group is specified. The graviton (not shown) has not been observed.

2.1.1 The Standard Model Particles

The universe is composed of a comparatively small number of species of particle. There are 12 spin 1/2 elementary particles called fermions which are subject to interactions mediated by the spin 1 gauge bosons [5]. The elementary particles, Table 2.1, are divided into 3 generations which resemble each other in all their properties except mass. Within each generation are a pair of quarks and a pair of leptons. The gauge bosons (Table 2.2) mediate the electromagnetic, weak and strong interactions between the fermions.

The vast majority of the visible matter of the universe is comprised of particles

from the first generation of the Standard Model. The leptons are the electron e and electron neutrino ν_e. The e has an electrical charge (Q) of -1 while the ν_e is chargeless. The quarks, an up quark Q = -1/3 and down quark Q = +2/3 complete the first generation. Anti-particles for each are denoted by a bar over the particle symbol, e.g. the $\bar{e}$ is a positron, an antielectron also denoted e^+. These antiparticles are simply Standard Model particles which carry the same mass but opposite charge, for instance the $\bar{u}$ carries Q = -2/3.

Quarks are electrically charged and therefore subject to electromagnetic force just as the electron is. Quarks carry an additional kind of charge called color. Color carrying particles are known as *hadrons*. They and the composite particles they make up are subject to the strong nuclear force.

Color is a three valued charge typically labeled "red" (r), "green" (g) and "blue" (b). Free particles with a net color charge are not experimentally observed and are confined within colorless composite particles. Hadrons containing three quarks are *baryons* while composites an antiquark and a quark are *mesons* [6].

This experimental observation is codified in a selection rule called the colorless hypothesis, which requires that only composite particles carrying one of each of the three values of color or some combination of color and anticolor are allowed. The neutron n, is a baryon containing a udd combination of quarks. A proton p on the other hand contains a uud combination. In each of these composites each quark carries a different value of color and thus the whole is colorless. Mesons contain a quark and an antiquark, e.g. the quark content of π^+ is $u\bar{d}$ and π^- contains $d\bar{u}$ quarks. Being composed of a quark and an antiquark the meson carries both color and anticolor and are thus colorless as well.

The second and third generations of leptons and quarks are heavier versions of their lighter cousins. Leptons of the second generation are the muon μ and

muon neutrino ν_μ. Charm and strange quarks complete the quark sector. The third generation is composed of the tau τ, tau neutrino ν_τ, and the bottom b and the top t quarks.

The fermion content of the Standard Model is displayed in Table 2.1. From this table several intriguing symmetries are visible to even the most casual observer. There are three generations of four particles, which with the exception of mass have properties mirrored by particles in the other generations. There are also equal numbers of quarks and leptons. An additional similarity between the quark and lepton sectors is that the difference in charge between pairs of quarks and pairs of leptons is one fundamental unit of charge.

The Standard Model is completed by the spin 1 *gauge particles*. The electromagnetic force is mediated through the exchange of the massless and electrically neutral photon γ. A diagram of the electromagnetic interaction between two electrons mediated by a photon can be seen in Figure 2.1. Similarly, the massive weak bosons W^+, W^-, Z^0 mediate the weak nuclear force while eight gluons, color carrying, massless and electrically neutral mediate the strong nuclear force. Because gluons and two of the weak bosons carry the charges of their respective fields these bosons interact with their own fields. This has consequences for the structure of the theory which describes them. Gluons are confined just as quarks are. While gluons carry both color and anticolor charge, it is not the same color and they are thus not colorless [5].

While it is proposed that the gravitational force is mediated by a massless gauge particle called the graviton, it has not yet been observed. As a result the Standard Model does not yet include the gravitational interaction. When the graviton is experimentally confirmed, the Standard Model will be expanded to include that interaction as well.

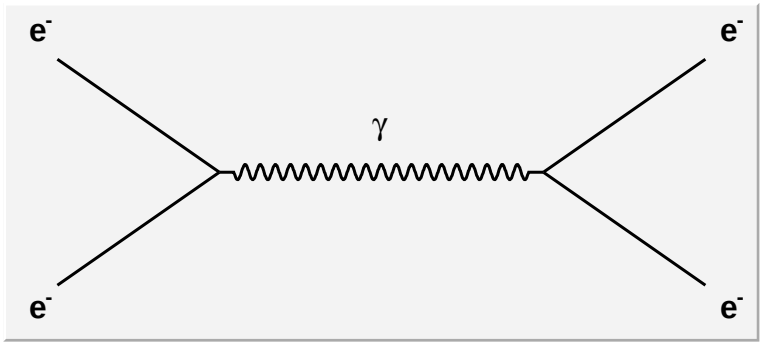

Figure 2.1: A pure electromagnetic interaction between two electrons e^- mediated by a photon γ.

We have covered the particle content of the Standard Model, but the Standard Model consists of more than a catalog of fundamental particles. The Standard Model is also underpinned by an understanding of how these particles interact and are related to each other. In the following sections we will cover the concept of symmetry, the application of which was instrumental to unifying our understanding of the electromagnetic and weak nuclear forces, now referred to as electroweak unification. The next section will use this foundation to cover a very brief introduction to "Beyond the Standard Model" physics such as the quest for grand unification, or rather the unification of the strong, electromagnetic, weak and gravitational forces into one theoretical framework. Most of these approaches require the existence of additional particles at high energy. The last section in this chapter covers one such, the leptoquarks that would play a role in mediating interactions between quarks and leptons.

2.1.2 Symmetry

The Standard Model is based upon the very successful *gauge theory* approach to describing fundamental interactions. In essence a gauge theory posits a phase invariance in the Lagrangian describing the physical phenomena involved.

A system is symmetric if when subject to a transformation some critical characteristic of the system is left unchanged. The rotation of a triangle in the plane by $2\pi/3$ is an example of a *discrete symmetry*, meaning that the set of transformations $\mathcal{S}$ contains a finite number of elements. In this case the set $\mathcal{S}$ consists of the rotations through an angle of $\{0, 2\pi/3, 4\pi/3\}$. The symmetry group for the rotations in the plane of a circle is an example of a continuous symmetry group. Phase transformations which we will soon apply to our description of quantum fields are another continuous symmetry.

Particle physics deals primarily with internal symmetries associated with quantum numbers. In general internal symmetries depend on space-time coordinates these are called local gauge symmetries or *gauge theories* [5, 6]. Typically we start with the Lagrangian for a free particle (fermion). We then require gauge invariance of the expression, accomplished through the introduction of boson fields. These fields and their quanta are the subject of the Standard Model.

2.1.3 Global Gauge Transformations

A *global gauge transformation* is a phase shift of a particle wave function ψ of the form

$$\psi \rightarrow \psi' = e^{i\theta}\psi, \tag{2.1}$$

where θ is explicitly not a function of space-time coordinates.

The Dirac Lagrangian [7] describes a free electron,

$$\mathcal{L}_{Dirac} = i\hbar c\bar{\psi}\gamma^{\mu}\partial_{\mu}\psi - mc^2\bar{\psi}\psi, \tag{2.2}$$

where $\hbar$ and c are respectively Planck's constant divided by 2π and the speed of

light. The factors γ^μ with the index μ running from 0 to 3 are the four gamma matrices, a set of 4 matrices of the form

$$\gamma^0 = \begin{pmatrix} 0 & 1 \\ 1 & 0 \end{pmatrix}, \qquad \gamma^i = \begin{pmatrix} 0 & -\sigma^i \\ \sigma^i & 0 \end{pmatrix}, \tag{2.3}$$

and the σ^i are in turn the set of three Pauli spin matrices

$$\sigma^1 = \begin{pmatrix} 0 & 1 \\ 1 & 0 \end{pmatrix}, \sigma^2 = \begin{pmatrix} 0 & -i \\ i & 0 \end{pmatrix}, \sigma^3 = \begin{pmatrix} 1 & 0 \\ 0 & -1 \end{pmatrix}. \tag{2.4}$$

A local gauge transformation of the wave functions ψ and $\bar{\psi}$ in the Dirac Lagrangian, Equation 2.2, introduces a factor of $e^{i\theta}$ associated with ψ but which is balanced by a factor of $e^{-i\theta}$ associated with $\bar{\psi}$. The form of the Dirac Lagrangian is preserved and so we say the Lagrangian is invariant under this kind of transformation.

2.1.4 Local Gauge Transformations

The more interesting case is the *local gauge transformation* [6, 7]

$$\psi \rightarrow \psi' = e^{iq\alpha(x^\mu)}\psi, \tag{2.5}$$

sometimes referred to as a gauge transformation of the second kind. Here the phase shift θ takes on an explicit dependence on space-time coordinates and out of which a charge factor has been pulled for later convenience, $\theta(x^\mu) = q\alpha(x^\mu)$.

Inserting the transformed wave function ψ into a Lagrangian containing normal derivatives gives rise to terms containing the derivatives of $\alpha(x^\mu)$ which are

not present in the original expression,

$$\partial_\mu e^{iq\alpha(x^\mu)}\psi = e^{ia\alpha(x^\mu)}[\partial_\mu + iq(\partial_\mu\alpha(x^\mu))]\psi. \tag{2.6}$$

That is to say, the form of the Lagrangian is not invariant.

Invariance is restored through the introduction of gauge vector boson fields. This is accomplished by replacing the normal derivative with a *covariant derivative*, $\mathcal{D}_\mu$ defined as normal derivative plus a field term which will compensate for the additional terms in Equation 2.6,

$$\begin{aligned} \mathcal{D}_\mu &\equiv \quad \partial_\mu - iq\partial_\mu\alpha(x^\mu), \\ \mathcal{D}_\mu &\equiv \qquad \partial_\mu - iqA_\mu, \end{aligned} \tag{2.7}$$

where $A_\mu = \partial_\mu\alpha(x^\mu)$.

Collecting the field terms the Lagrangian takes the form

$$\mathcal{L} = \mathcal{L}_{Dirac} - iq\bar{\psi}A_\mu\psi. \tag{2.8}$$

The additional term $-iq\bar{\psi}A_\mu\psi$ couples the particle field described by ψ and charge q with the gauge boson field A_μ. The Lagrangian is however not complete. For any fields introduced in this manner we must also introduce kinetic and potential energy terms to the Lagrangian [5].

The Proca Lagrangian for a spin 1 vector field supplies the kinetic energy term $\frac{1}{16\pi}F^{\mu\nu}F_{\mu\nu}$, where $F^{\mu\nu} = \partial^\mu A^\nu - \partial^\nu A^\mu$. For the electromagnetic field $F^{\mu\nu}$ corresponds to the electromagnetic field strength tensor. The potential term from the same Lagrangian is proportional to $m^2A^\nu A_\nu$ which is not invariant under local gauge transformation. The theory is rescued by the fact that the gauge boson for

the electromagnetic field, the photon (γ) is massless thus eliminating this term. Our new improved Lagrangian is invariant under local gauge transformation,

$$\mathcal{L}_{\mathcal{QED}} = i\hbar c\bar{\psi}\gamma^{\mu}\partial_{\mu}\psi - mc^2\bar{\psi}\psi - iq\bar{\psi}A_{\mu}\psi + \frac{1}{16\pi}F^{\mu\nu}F_{\mu\nu}. \tag{2.9}$$

To summarize, Equation 2.5 is an example of a single parameter local gauge transformation, a $U(1)$ symmetry of the Lagrangian. The expression resulting from the application of this transformation in conjunction with requiring invariance of the Lagrangian is Equation 2.9. This is the Lagrangian used to describe the quantized electromagnetic field, Quantum Electrodynamics or QED for short.

In the next two sections we take these ideas and apply them to a larger symmetry group $SU(3)_{color} \times SU(2)_L \times U(1)_Y$ which more accurately describes the SM. Section 2.1.5 covers Quantum Chromodynamics (QCD) or the physics of the $SU(3)_{color}$ symmetry. The remaining portion, $SU(2)_L \times U(1)_Y$ described in Section 2.1.6 unifies our understanding of the fields and quanta associated with the electromagnetic and weak nuclear forces.

It is one of the self assigned tasks of particle physicists to unite these two separate sets of fundamental processes, QCD and Electroweak physics under a single unified description. Past success, the unification of QED and Weak Nuclear physics, motivates the attempt to repeat that success with QCD. The experimental search for the $VLQ3$ or rather the search for any field carrying both baryon number and lepton number is about one of the approaches to unification. Equally, the absence of a leptoquark within accessible energy scales places constraints on models that require their existence. The failure to find a leptoquark-like particle at any energy scale will tell us nearly as much about the shape of a unified theory as finding the particle itself.

2.1.5 Quantum Chromodynamics

The physics of quarks is described by Quantum Chromodynamics (QCD) or the quantum theory of the $SU(3)$ color symmetry. In contrast to the electromagnetic charge the color charge carried by quarks comes in three varieties. These are labeled *red* r, *green* g and *blue* b. A neutral electrical charge is achieved with $q(-q)$. In the QCD case, a neutral color charge is achieved through a combination of color anticolor such as $r\bar{r}$ or through a combination of all three colors such as rgb. The most notable thing about QCD is that particles carrying a net color charge are confined, i.e. are not experimentally observed, but can be detected as the constituent particles of larger composite particles. The quantum of the QCD field is the gluon. It is massless, electrically neutral and carries two color charges one each of color and anticolor. As a consequence gluons interact not only with quarks but with each other as well.

The invariant QCD Lagrangian is built using the same procedure as the QCD case:

1. Impose a symmetry on the free Lagrangian.
2. Define a covariant derivative with a compensating field for each degree of freedom possessed by the symmetry.
3. Add kinetic terms for the new fields.
4. Define a field strength tensor in terms of the introduced fields.
5. Write down the resulting Lagrangian.

In general, a symmetry $SU(n)$ possesses $n^2 - 1$ generators or degrees of free-

dom, each of which is associated with a quantized particle field. For the case of $SU(3)_{Color}$, $n^2 - 1$ or eight gluon fields arise from the eight generators. These generators are the Gell-Mann λ matrices shown in Equation 2.12. A degree of freedom accompanies each generator expressed as a separate field A_μ^α and so the local gauge transformation takes on the form,

$$\psi \rightarrow \psi' = exp\left(\frac{-ig_s\lambda_\alpha\phi^\alpha(x^\mu)}{\hbar c}\right)\ \psi, \tag{2.10}$$

where g_s is the strong coupling constant.

The covariant derivative for QCD is then

$$\mathcal{D}_\mu \equiv \partial_\mu - ig_s\lambda_\alpha \cdot A_\mu^\alpha, \tag{2.11}$$

where $\partial_\mu\phi^\alpha(x^\mu) = A_\mu^\alpha$ and there is an implied summation on the index α over the eight λ_α and gluon field's A_μ^α. The λ_α are 3×3 traceless hermitian matrices [8]:

$$\lambda_1 = \begin{pmatrix} 0 & 1 & 0 \\ 1 & 0 & 0 \\ 0 & 0 & 0 \end{pmatrix}, \quad \lambda_2 = \begin{pmatrix} 0 & -i & 0 \\ -i & 0 & 0 \\ 0 & 0 & 0 \end{pmatrix}, \quad \lambda_3 = \begin{pmatrix} 1 & 0 & 0 \\ 0 & -1 & 0 \\ 0 & 0 & 0 \end{pmatrix},$$

$$\lambda_4 = \begin{pmatrix} 0 & 0 & 1 \\ 0 & 0 & 0 \\ 1 & 0 & 0 \end{pmatrix}, \quad \lambda_5 = \begin{pmatrix} 0 & 0 & -i \\ 0 & 0 & 0 \\ i & 0 & 0 \end{pmatrix}, \quad \lambda_6 = \begin{pmatrix} 0 & 0 & 0 \\ 0 & 0 & 1 \\ 0 & 1 & 0 \end{pmatrix},$$

$$\lambda_7 = \begin{pmatrix} 0 & 0 & 0 \\ 0 & 0 & -i \\ 0 & i & 0 \end{pmatrix}, \quad \lambda_8 = \frac{1}{\sqrt{3}} \begin{pmatrix} 1 & 0 & 0 \\ 0 & 1 & 0 \\ 0 & 0 & -2 \end{pmatrix}. \tag{2.12}$$

Upon attaching a field strength tensor for the gluons to the QCD Lagrangian, the expression becomes,

$$\mathcal{L}_{QCD} = i\hbar c\bar{\psi}\gamma^\mu\partial_\mu\psi - mc^2\bar{\psi}\psi - q\bar{\psi}\gamma^\mu\lambda A_\mu\psi \cdot A_\mu + \frac{1}{16\pi}\mathbf{F}^{\mu\nu}_{\alpha} \cdot \mathbf{F}^{\alpha}_{\mu\nu}. \tag{2.13}$$

Note that here the field strength tensor takes the form

$$F^\alpha_{\mu\nu} = \partial_\mu A^\alpha_\nu - \partial_\nu A^\alpha_\mu + g_s f^{\alpha\beta\gamma} A_{\mu\beta} A_{\nu\gamma}. \tag{2.14}$$

The additional term at the end results from the fact that $SU(3)$ is a *non-abelian* group. This means that the generators of $SU(3)$ do not commute with each other. The structure constants of $SU(3)$, $f^{\alpha\beta\gamma}$ are defined by the commutator of the generators [8].

$$[\lambda^\alpha, \lambda^\beta] = 2if^{\alpha\beta\gamma}\lambda^\gamma \tag{2.15}$$

2.1.6 Electroweak Unification

The work of Glashow, Salam and Weinberg [2, 3, 4] unified our descriptions of electromagnetism and the weak nuclear interactions by demanding local gauge invariance under the composed group $SU(2)_L \times U(1)_Y$ symmetry. The subscript L refers to the *handedness* and the Y to the *hypercharge*.

The weak interaction described by the symmetry group $SU(2)_L$ couples only

with the left-handed projections of the fermion fields. To obtain the handed projections of a particle field the chirality operator γ^5 is applied. For the electron we have,

$$e_L^- = \frac{1}{2}(1-\gamma^5)e^-$$
$$e_R^- = \frac{1}{2}(1+\gamma^5)e^-.$$

The four solutions of the Dirac Equation were a pair of left and right-handed particles and a second pair of left and right-handed antiparticles. In this, the Weyl representation, the fermions are paired (e_L^-, e_R^+) and (e_R^-, e_L^-) where the Left-handed fermions transform as doublets under $SU(2)_L$ [7],

$$f_L \rightarrow e^{iT^\alpha\theta_\alpha} f_L;\ f_L = \begin{pmatrix} \nu_L \\ e_L \end{pmatrix}, \begin{pmatrix} u_L \\ d_L \end{pmatrix}, \ldots \tag{2.16}$$

and right-handed fermions transform as singlets

$$f_R \rightarrow f_R;\ f_R = (e_R, u_R, d_R, \ldots)\,. \tag{2.17}$$

The set of three operators $\mathbf{T}^\alpha$ in Equation 2.16 are the $SU(2)$ generators of weak isospin, $T^\alpha = \frac{1}{2}\sigma_\alpha$ where the σ_α are the three Pauli spin matrices, Equation 2.4. The commutation relation for the weak isospin generators is

$$[T^\alpha, T^\beta] = e_{\alpha\beta\gamma}T^\gamma. \tag{2.18}$$

The single parameter generator of $U(1)_Y$ commutes with the set T^α.

Lepton	T	T^3	Q	Y
ν_L	$\frac{1}{2}$	$\frac{1}{2}$	0	-1
e_L	$\frac{1}{2}$	$-\frac{1}{2}$	-1	-1
e_R	0	0	-1	-2

Table 2.3: Electromagnetic charge, Weak Isospin, and Hypercharge for the first generation of leptons.

Quark	T	T^3	Q	Y
u_L	$\frac{1}{2}$	$\frac{1}{2}$	$\frac{2}{3}$	$\frac{1}{3}$
d_L	$\frac{1}{2}$	$-\frac{1}{2}$	-$\frac{1}{3}$	$\frac{1}{3}$
u_R	0	0	$\frac{2}{3}$	$\frac{4}{3}$
d_R	0	0	-$\frac{1}{3}$	$\frac{2}{3}$

Table 2.4: Electromagnetic charge, Weak Isospin, and Hypercharge for quarks.

Fermion quantum numbers given in Tables 2.3 and 2.4 must satisfy the Gell-Mann Nishijima formula, Equation 2.19 which relates the electromagnetic charge, the third component of the weak isospin and the hypercharge [5],

$$Q = T^3 + \frac{1}{2}Y. \tag{2.19}$$

Now that we have the generators of both $SU(2)_L$ and our previous understanding of $U(1)_Y$ we can simply write down the covariant derivative for electroweak theory. The derivative is

$$\mathcal{D} = \partial_\mu + igT^\alpha W_\alpha + ig'\frac{Y}{2}B_\mu, \tag{2.20}$$

where the g and g' are coupling constants corresponding to $SU(2)_L$ and $U(1)_Y$

respectively and there is an implied summation over $\alpha = \{1, 2, 3\}$.

The associated gauge boson fields are $W_\alpha(x_\mu)$ the weak bosons of $SU(2)$ and B_μ the hyper-charge boson of $U(1)_Y$. The kinetic energy terms which need to be added to the Lagrangian for the W_α and B_μ fields are similar to the fields derived for the electro weak Lagrangian includes terms for the gauge field

$$-\frac{1}{4}W^i_{\mu\nu}W^{\mu\nu}_i - \frac{1}{4}B_{\mu\nu}B^{\mu\nu}. \tag{2.21}$$

For the non-abelian field $W^i_{\mu\nu}$

$$W^i_{\mu\nu} = \partial_\mu W^i(x_\nu) - \partial_\nu W^i(x_\mu) + ge^{ijk}W_{\mu j}W^i_{\nu k}. \tag{2.22}$$

Like $SU(3)$ the group $SU(2)$ is non-abelian group as well. As in Equation 2.14 a self interacting term, this time of the form $ge^{ijk}W_{\mu j}W^i_{\nu k}$ appears. The field strength tensor for the B_μ field takes on exactly the same form as the electromagnetic field strength tensor,

$$B_{\mu\nu} = \partial_\mu B_\nu - \partial_\nu B_\mu. \tag{2.23}$$

The physical gauge bosons are obtained from a mixture of the electro weak interactions eigenstates [5, 7],

$$W^\pm_\mu = \frac{1}{\sqrt{2}}(W^1_\mu \mp iW^2_\mu), \tag{2.24}$$

$$Z_\mu = W^3_\mu \cos\theta_W - B_\mu \sin\theta_W, \tag{2.25}$$

$$A_\mu = W^3_\mu \sin\theta_W + B_\mu \cos\theta_W. \tag{2.26}$$

The parameter θ_W is called the *weak mixing angle* experimentally measured to be $\sin^2\theta_w = 0.2255 \pm 0.0021$ [8]

The preceding description of the electroweak theory is for a system of massless gauge boson fields. The problem however is that the real world $W^\pm$ and Z^0 particles are massive. As with the QED Lagrangian a potential term for the fields of the form $-m_W^2 W^\mu W_\mu$ and $-m_Z^2 Z^\mu Z_\mu$ would violate the gauge symmetry of the $SU(2)_L \times U(1)_Y$ group. For this theory to work the boson fields must remain massless and another gauge invariant method must be found the generate the masses of the $W^\pm$ and Z^0.

2.1.7 Spontaneous Symmetry Breaking

In this section *Spontaneous Symmetry Breaking* is introduced as a means by which massless particle fields can gain their experimentally observed masses without violating the gauge invariance of the underlying theory. Under spontaneous symmetry breaking the particle fields will be expressed in an expansion around a non-zero minimum of the field. While the Lagrangian retains its gauge symmetry, that symmetry is hidden by the way that the Lagrangian is expressed. In this form the Lagrangian now contains a term proportional to the field potential energy. Recall that previously the potential energy terms, the source of which was the assumed form of a field Lagrangian, were not gauge invariant and were required to vanish. This was accomplished by setting the mass equal to zero. Here a mass term arises solely from the manner in which the field is expressed. Gauge invariance is not violated by this term, but is simply hidden, and so the particle field gains an effective mass.

We will be working with Lagrangians that, while invariant under the symme-

try transformation U, possess a vacuum expectation value that is not, $U|0>\neq|0>$. Alternately there should exist field operators with non-vanishing expectation values $<0|\Phi|0>\neq 0$. The simplest Lagrangian which exhibits spontaneous symmetry breaking can be written as

$$\mathcal{L}_{sbc} = (\mathcal{D}_\mu\Phi)^+(\mathcal{D}^\mu\Phi) - V(\Phi), \tag{2.27}$$

where

$$\Phi = \begin{pmatrix} \phi^+ \\ \phi_0 \end{pmatrix} \tag{2.28}$$

is a fundamental complex doublet with hyper-charge $Y(\Phi) = 1$ [5, 7]. The simplest re-normalizable potential is

$$V(\Phi) = -\mu^2\Phi^+\Phi + \lambda(\Phi^+\Phi); \quad \lambda > 0. \tag{2.29}$$

For $(-\mu^2) < 0$, the minimum of the potential is the bottom of a circular trough, of radius $\nu \equiv \sqrt{\mu^2/\lambda}$, Figure 2.2.

Note that here we have chosen a particular gauge or phase of the field in which the state is projected entirely along $\nu/\sqrt{2}$.

$$|\langle 0|\Phi|0\rangle| = \begin{pmatrix} 0 \\ \nu/\sqrt{2} \end{pmatrix} \tag{2.30}$$

Consequently the system assumes one vacuum eigenstate state which no longer reflects the symmetry of the potential.

The physical spectrum is then determined using small oscillations about the

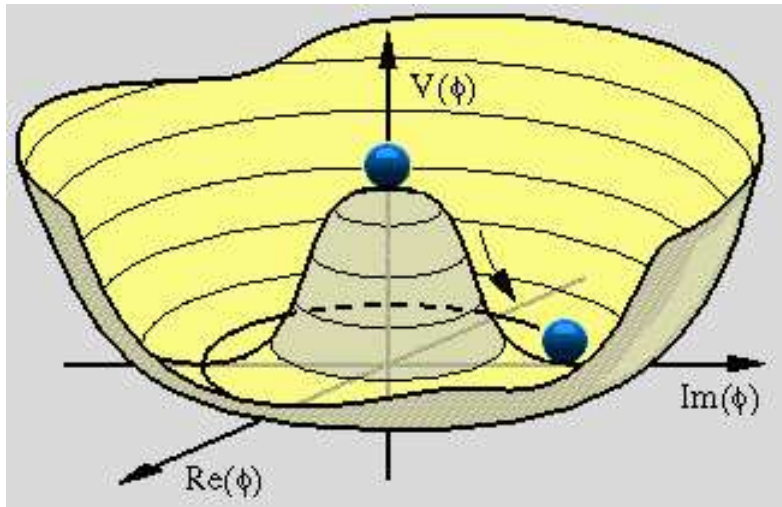

Figure 2.2: The potential has a minim in a circular trough of radius $\nu \equiv \sqrt{\mu^2/\lambda}$

vacuum expectation value,

$$\Phi(x) = exp\left(i\frac{\vec{\xi}\vec{\sigma}}{\nu}\right)\begin{pmatrix} 0 \\ (\nu + H(x))/\sqrt{2} \end{pmatrix}, \tag{2.31}$$

and then eliminating the unphysical field $\vec{\xi}(x)$ through a choice of gauge [7]. The tree level predictions give

$$m_W = \frac{1}{2}g\nu \qquad\qquad m_Z = \frac{1}{2}\sqrt{g^2 + g'^2}\nu, \tag{2.32}$$

while the photon remains massless.

The parameter ν determined experimentally from μ-decay and is equal to 246 GeV. The predicted masses $m_W = 80.4$ GeV and $m_z = 91.2$ GeV anticipated the experimental observation and are considered one of the great successes of the Standard Model.

This procedure which unifies spontaneous symmetry breaking and gauge in-

variance is called the *Higgs mechanism*. It introduces a new scalar boson called the Higgs boson and like other introduced fields it requires its own terms in the Lagrangian. The interactions of the Higgs boson with the fermions introduces a Yukawa term to the Standard Model Lagrangian,

$$\mathcal{L}_{Yukawa} = -M_U^{ij}\bar{U}_L^i U_R^j - M_D^{ij}\bar{D}_L^i D_R^j - M_E^{ij}\bar{E}_L^i E_R^j - h.c., \tag{2.33}$$

where

$$U_{R,L} = \begin{pmatrix} u' \\ c' \\ t' \end{pmatrix}_{R,L}, D_{R,L} = \begin{pmatrix} d' \\ s' \\ b' \end{pmatrix}_{R,L}, E_{R,L} = \begin{pmatrix} e' \\ \mu' \\ \tau' \end{pmatrix}_{R,L}, \tag{2.34}$$

and M_U, M_D and M_E are 3×3 complex matrix generators. By diagonalizing these matrices one obtains the mass eigenstates of the quarks and leptons.

Hence the Higgs Boson imparts masses to the gauge bosons $W^{\pm}$ and Z^0 as well as to the quarks and leptons, but unlike the $W^{\pm}$ and Z^0 masses which are predicted in terms of measured coupling constants, the fermion masses are each set by a separate Yukawa coupling constant,

$$m_f = \lambda_f \frac{\nu}{\sqrt{2}}. \tag{2.35}$$

The collection of λ_f are a set of unknown parameters of the Standard Model and so the mass hierarchy in the fermion sector remains completely undetermined. In addition there is still no prediction for the Higgs self coupling on which the Higgs mass itself depends, $M_{Higgs} = \sqrt{2\nu^2\lambda}$. The Higgs remains the only undiscovered particle of the SM.

2.2 Beyond the Standard Model

Despite the success of electroweak theory in predicting the masses of the weak bosons there exist a large number of unconstrained parameters in the Standard Model, Yukawa couplings between the Higgs and the individual fermions as well as three independent gauge couplings. While in principle these are measurable parameters, other questions remain. Why are there three generations of leptons and quarks? Why do the weak bosons mix in the way that they do? How does gravity fit into the Standard Model? What is this dark matter made from? Why does the universe possess a matter antimatter asymmetry? What is the origin of mass itself? The very fundamental nature of these questions lead us to treat the Standard Model as a work in progress.

The successful unification of the electromagnetic and weak nuclear interactions under the framework of electroweak theory is one of the major triumphs of the Standard Model. We are loath to abandon a successful tool and so there remains the belief that symmetry rules the world and that all of these questions can be understood in terms of some fundamental structure with a simple description however complex the physical expression of that relationship may be.

2.2.1 Unification

Grand Unified Theories (GUTs) seek to repeat the success of electroweak unification by uniting the QCD and electroweak theory. If the separate energy scales of the known forces, QCD, QED and Weak interactions are to be explained by a single symmetry breaking event at an enormous energy scale then evolution of the coupling constants should all converge at that same energy [9]. The evolution of these couplings, strong (α_S), weak (α_W) and electromagnetic (α_e) forces

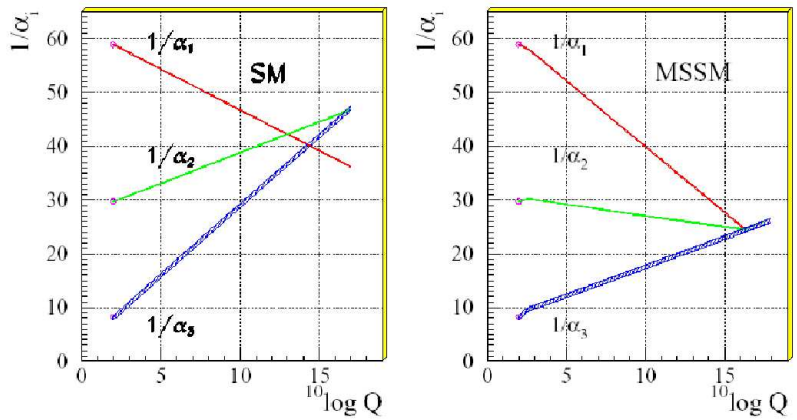

Figure 2.3: The evolution of the inverse coupling constants $1/\alpha_i$ are shown for both the Standard Model on the left and MSSM on the right. The MSSM plot presupposed a SUSY threshold above which super partners of the Standard Model particles provide corrections to the slope of the $1/\alpha_i$ plots. Unification at a single point is only achieved for the MSSM.

is sensitive to the full inventory of particles that can exist. Given the particle content of the Standard Model the couplings (displayed as inverse values $1/\alpha_i$) evolve as the left plot in Figure 2.3. The right plot shows the evolution of same parameters given the theorized existence of super partners to the known particles of the Standard Model under a framework known as the Minimal Super Symmetric Model (MSSM). It is proposed that at this scale unification takes the form of a single symmetry group which encompasses the $SU(3)_c \times SU(2)_L \times U(1)_Y$ symmetry which describes our world.

The *Hierarchy Problem* also hints at the existence of particles and fields beyond the Standard Model. This arises when the measured value of a fundamental parameter, couplings or masses differ from the theoretical values used in the Lagrangian used to describe the phenomena. With respect to the Higgs, the natural scale of the Higgs is expected to be in the range of the plank mass, roughly 10^{19} GeV/c^2 due to quadratically divergent radiative corrections in the Lagrangian

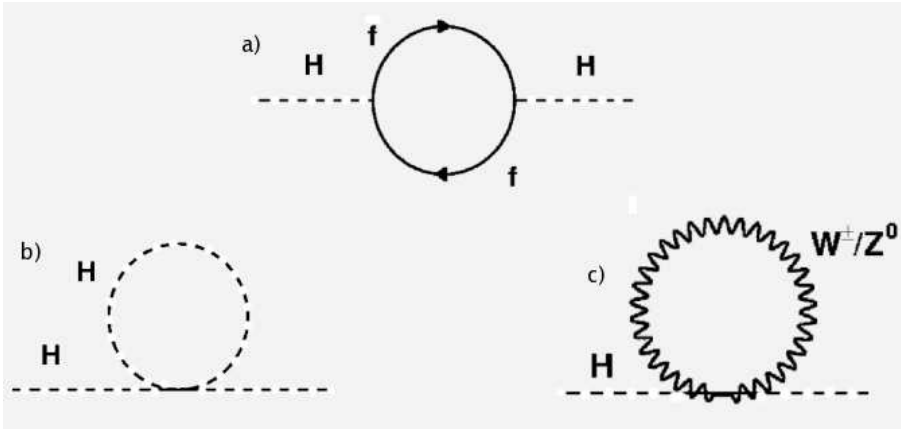

Figure 2.4: Feynman diagrams of a) fermion, b) Scalar and c) vector boson loop corrections to the Higgs mass.

describing the theory. Three diagrams contributing to the self energy of the Higgs are shown in Figure 2.4.

Indirect measures of the Higgs mass from electroweak observables [10] and the top mass [11] place the upper limit on the Higgs mass at 200 GeV/c^2 with a 95% confidence level. These two results can be reconciled with a delicate balancing or *fine tuning* of parameters to bring the effective Higgs mass down in order to agree with observation. The nature of this fine tuning is unknown, but many schemes have been proposed including various sypersymmetric models indicating plenty of physics to be discovered beyond the Standard Model.

2.2.2 Leptoquarks

Unification schemes often involve a field mediating interactions of the quark and lepton fields. The quanta of this field, the leptoquark, makes an appearance in a surprising variety of theoretical frameworks. A very brief list follows, $SU(5)$ GUT [12], Superstrings [13], $SU(4)$ Pati-Salam [14], Compositness [15] and Technicolor [16, 17].

Of necessity the leptoquark field is a color triplet boson carrying both lepton and baryon number. As a color carrying particle it will transform as a fundamental representation of $SU(3)_{color}$ and so appear in both scalar ($spin = 0$) and vector ($spin = 1$) varieties. Experimentally observed constraints on Flavor Changing Neutral Currents (FCNC) suggest a strong generational coupling with leptoquarks decaying to quarks and leptons of a single generation[1]. Proton stability implies a massive leptoquark on the order or or greater than the mass of the top quark [8]. Leptoquarks are also assumed to be chiral to prevent excessive $\pi \rightarrow e\nu$ decays [19]. The remaining properties, weak isospin, electric charge and couplings to leptons and quarks are model dependent. We further assume that the fermion interactions of the leptoquarks are invariant under the Standard Model gauge group and have dimensionless couplings thus providing further restrictions on the leptoquark quantum numbers, see Table 2.5, [20, 21].

At the Tevatron leptoquarks can be produced in pairs either through quark-antiquark annihilation, Figure 2.5, or through gluon-gluon fission, Figure 2.5. Quark-antiquark annihilation is the dominant production mechanism due to the abundance of antiquarks in the antiproton beam. Gluon-gluon fusion is expected to be the dominant process at the Large Hadron Collider. For plots of the pair production cross section for $VLQ3$ proceeding from quark-antiquark annihilation and from gluon-gluon fusion see Figure 3.1.

The model independent Lagrangian we proceed from is contained in the work of J. Blümlein, *et al.* [21]. The effective Lagrangian containing leptoquark inter-

[1]A leptoquark which is blind to quark lepton generation would allow a path to violate the observed FCNC limits. This suggests that if leptoquarks exist at all they come in three generations. The limits $\Gamma(K^+ -> \pi^+\nu\bar{\nu})/\Gamma(K^+ \rightarrow all) = 1.6^{1.8}_{0.8} \times 10^{-10}$[18] means that Flavor Changing Neutral Currents (FCNC) are highly suppressed in the first generation. Observed experimental limits for the other generations, bottom changing neutral currents (BCNC) and charm changing neutral currents (CCNC) are less stringent but still on the order of 10^{-7} for BCNC and 10^{-6} for CCNC.

LQ	Spin	3B+L	SU(3)	SU(2)	U(1)	Q	Channels(s)
S_1	0	-2	3^*	1	$\frac{1}{3}$	$-\frac{1}{3}$	$\tau^-_{L,R}t[g_{1L,R}], \nu_L b[-g_{1L}]$
$\tilde{S}_1$	0	-2	3^*	1	$\frac{4}{3}$	$-\frac{4}{3}$	$\tau^-_R b[\tilde{g}_R]$
S_3	0	-2	3^*	3	$\frac{1}{3}$	$\frac{2}{3}$ $-\frac{1}{3}$ $-\frac{4}{3}$	$\nu_L t[\sqrt{2}g_{3L}]$ $\tau^-_L t[-g_{3L}], \nu_L b[-g_{3L}]$ $\tau^-_L b[-\sqrt{2}g_{3L}]$
V_2	1	-2	3^*	2	$\frac{5}{6}$	$-\frac{1}{3}$ $-\frac{4}{3}$	$\tau^-_R t[-g_{2R}], \nu_L b[-g_{2L}]$ $\tau^-_[L, R]b[-g_{2L,R}]$
$\tilde{V}_2$	1	-2	3^*	2	$-\frac{1}{6}$	$\frac{2}{3}$ $-\frac{1}{3}$	$\nu_L t[\tilde{g}_{2L}]$ $\tau^-_L t[\tilde{g}_{2L}]$
R_2	0	0	3	2	$\frac{7}{6}$	$-\frac{2}{3}$ $-\frac{5}{3}$	$\tau^-_R \bar{b}[= h_{2R}], \nu_L \bar{t}[h_{2L}]$ $\tau^-_{L,R}\bar{t}[h_{2L,R}]$
$\tilde{R}_2$	0	0	3	2	$\frac{1}{6}$	$\frac{1}{3}$ $-\frac{2}{3}$	$\nu_L \bar{b}[\tilde{h}_{2L}]$ $\tau^-_L \bar{b}[\tilde{h}_{2L}]$
U_1	1	0	3	1	$\frac{2}{3}$	$-\frac{2}{3}$	$\tau^-_{L,R}\bar{b}[h_{1L,R}], \nu_L \bar{t}[h_{1L}]$
$\tilde{U}_1$	1	0	3	1	$\frac{5}{3}$	$-\frac{5}{3}$	$\tau^-_R \bar{t}[\tilde{h}_{1R}]$
U_3	1	0	3	3	$\frac{2}{3}$	$\frac{1}{3}$ $-\frac{2}{3}$ $-\frac{5}{3}$	$\nu_L \bar{b}[\sqrt{2}h_3 L]$ $\tau^-_L \bar{b}[-h_{3L}], \nu_L \bar{t}[h_{3L}]$ $\tau^-_L \bar{t}[\sqrt{2}h_{3L}]$

Table 2.5: Leptoquark Species: Quantum numbers and decay channels for various species of leptoquark. The subscript on the leptoquark is the dimensionality of the $SU(2)$ group representation. The fermion number is given by $3B + L$ where B is the fractional Baryon number and L is the lepton number. In the decay channels L and R refer to the chirality of the τs.

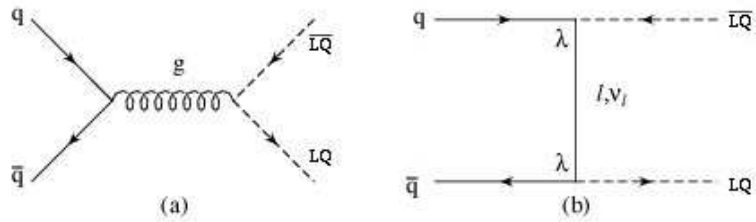

Figure 2.5: Leptoquark production from $q\bar{q}$ fusion. Production can proceed from a) a trilinear coupling to an intermediate gluon or b) via an s-channel e, μ, τ or ν. Diagram a is the dominant contributor to the production amplitude in the $q\bar{q}$ fusion channel.

actions divided into scalar and vector parts,

$$L = L^g_{scalar} + L^g_{vector}. \tag{2.36}$$

The scalar interaction is described by,

$$L^g_{scalar} = \sum_{scalars} [(D^{\mu}_{ij}\Phi^j)(D^{ij}_{\mu}\Phi_k) - M_S^2\Phi^{i\dagger}\Phi_i], \tag{2.37}$$

where M_S is the scalar leptoquark mass. The vector leptoquark portion of the effective Lagrangian is,

$$L^g_{vector} = \sum_{vectors} \left\{ -\frac{1}{2}G^{i\dagger}_{\mu\nu}G^{\mu\nu}_i + M_V^2\Phi^{i\dagger}_{\mu}\Phi^{\mu}_i - ig_sF(\kappa_G, \lambda_G) \right\}$$
$$F(\kappa_G, \lambda_G) = (1-\kappa_G)\Phi^{i\dagger}_{\mu}t^a_{ij}\Phi^j_{\nu}G^{\mu\nu}_a + \frac{\lambda_G}{M_V^2}G^{i\dagger}_{\sigma\mu}t^a_{ij}G^{i\mu}_{\nu}\mathcal{G}^{\nu\sigma}_a. \tag{2.38}$$

Here g_s is strong coupling constant and t^a are the generators of $SU(3)_{color}$. The masses of the scalar and vector leptoquarks are M_S and M_V. The anomalous couplings κ_G and λ_G are assumed to be real and are related to the 'magnetic' moment, μ_v and the 'electric' quadrapole moment, q_v, by the following relation-

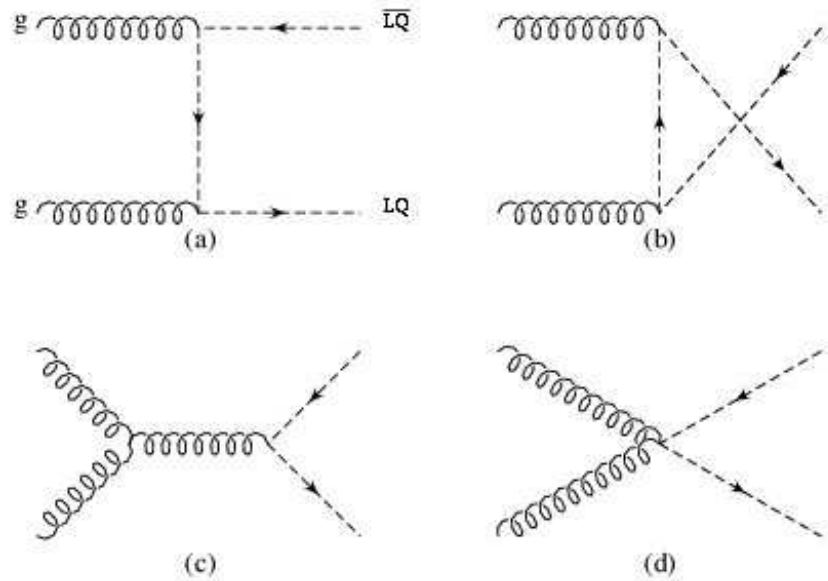

Figure 2.6: Feynman diagrams for leptoquark production from gluon-gluon fusion. Diagrams a), b) and c) are the dominant contributors to the production amplitude in the gluon-gluon fusion channel.

ship

$$\mu_V = \frac{g_s}{2M_V}(2 - \kappa_G + \lambda_G) \tag{2.39}$$

$$q_V = -\frac{g_s}{M_V^2}(2 - \kappa_G - \lambda_G) \tag{2.40}$$

The covariant derivative is the QCD derivative defined in Equation 2.11 with indices explicitly displayed. The notation used in Blümlein exchanges the labels for the generators λ_a for t_a to avoid confusion with the anomalous coupling λ_G.

$$D_\mu^{ij} = \partial_\mu \delta^{ij} - i g_s t_a^{ij} A_\mu^a \tag{2.41}$$

The field strength tensor for the gluon field is given in the familiar form,

$$\mathcal{G}^a_{\mu\nu} = \partial_\mu A^a_\nu - \partial_\nu A^a_\mu - g_s f^{abc} A_{b\mu} A_{c\nu}. \tag{2.42}$$

The field strength tensor for the leptoquark field, utilizing the covariant derivative, Equation 2.41, is given by

$$G^i_{\mu\nu} = D^{ik}_\mu \Phi_{\nu k} - D^{ik}_\nu \Phi_{\mu k}. \tag{2.43}$$

Leptoquarks subsequently decay into either a charged lepton quark pair or into a neutrino quark pair. The factor β is the branching ratio of a leptoquark decaying to a quark and charged lepton of the appropriate generation. With $\beta = 0$ leptoquark decays proceed via a quark and neutrino. The CDF and D0 have searched two scenarios of $\beta = 1$ and $\beta = 0$ for the scalar type leptoquark. The signatures are $l^+l^-q\bar{q}$ ($\beta = 1$), $\nu\bar{\nu}q\bar{q}$ ($\beta = 0$), and $l\nu q\bar{q}$ ($\beta = 0.5$) for the first and second generations of leptoquark [22] as well as the third generation scalar leptoquark [23].

Chapter 3

GRACE/GR@PPA

We have developed a new Monte Carlo event generator for leptoquark events under the GR@PPA framework[24, 25]. GR@PPA stands for "GRACE at pp / anti-p Colliders," and is an extension of the GRACE matrix element generator for lepton interactions to hadron collisions. While PYTHIA was sufficient for the scalar leptoquark study [26], a proposed search for the third generation vector leptoquark [27] exposed some new requirements. Under the existing CDF simulation and production framework used in Run II, a tau from the decay of a leptoquark is handled by a physics package called TAUOLA [28]. In order to correctly simulate the decays of a tau, TAUOLA requires the preservation of the helicity amplitudes. No existing event generation tool met this need, specifically spin sums of the taus were averaged over.

3.1 Extension of GRACE to $pp/p\bar{p}$ collisions

The GRACE system was developed for lepton interactions with their well defined initial and final states. GRACE itself is a FORTRAN program for gen-

erating Feynman Diagrams to any order of perturbation theory at Tree-Level. Progress on Loop Diagrams has been made, but is not fully automatic. The GRACE framework takes advantage of the three additional packages to generate the event. CHANNEL is used to evaluate the amplitudes of the Feynman diagrams. BASES is a multi-dimensional grid optimized random number integration package. SPRING converts the numerical result into the kinematic variables to fully specify the event.

GR@PPA is an extension of the GRACE system to hadron interactions. Hadron collisions involve initial states which are composite particles possessing flavor and initial momenta described by Parton Distribution Functions (PDFs) all of which need to be accounted for in the generation of the matrix element. GR@PPA determines the initial and final state partons, flavors, and momenta of the incoming particles. Final state particles are also specified for subsequent use in decays and jet production. GR@PPA produces a file of events and a production cross section. An event entry contains both parent particles, the $VLQ3$ pair, as well as the b quark and tau daughter for each $VLQ3$. For this analysis all decays were restricted to a single channel, $VLQ3 \rightarrow \tau + \bar{b}$. The parameter $\beta = Br(LQ \rightarrow q + l)$ describes the branching ratio between different decay channels of the $VLQ3$ and is assigned a value from 0 to 1.0. The probability for the other decay channel $LQ \rightarrow q + \nu$ to occur is $1 - \beta$. A search for the process $LQ \rightarrow q + \nu$ would involve a greater emphasis on missing transverse energy and is simply not the signature chosen for this analysis. We use an assigned value of $\beta = 1.0$, not fixed by theory but rather as an efficiency in generating the Monte Carlo for this particular experimental signature. The CTEQ5L PDF library is specified in GR@PPA and renormalization/factorization scale, $Q^2 = m^2_{LQ3}$ was used.

This analysis is the first leptoquark search to use a matrix element event generator. Up to this point experimental signatures including taus were generated in a format in which the tau polarizations were lost, specifically spin sums were averaged over. GR@PPA takes advantage of incoherent but kinematically similar subprocess by summing over them in the calculation of the total cross section, Equation 3.1.

3.2 Total Cross Section

Cross sections with hard interaction in $pp/p\overline{p}$ collisions can be described by

$$\sigma = \sum_{i,j,F} \int dx_1 \int dx_2 \int d\hat{\Phi}_F f_i^1(x_1, Q^2) f_j^2(x_2, Q^2) \frac{d\hat{\sigma}_{ij\to F}(\hat{s})}{d\hat{\Phi}_F}, \tag{3.1}$$

where $f_i^a(x_a, Q^2)$ is the PDF of the hadron a (p or $\bar{p}$) which gives the probability to find the parton i with energy fraction x_a at the probing virtuality of Q^2 [29]. The differential cross section $d\hat{\sigma}_{ij} \to F(\hat{s})/d\hat{\Phi}_F$ describing the parton-level hard interaction gives final state F from a collision of partons, i and j. The square of the total initial four vector momentum is given by $\hat{s}$, while $d\hat{\Phi}_F$ is the differential element of the final state phase space. The sum is over all relevant combinations of i,j and F.

Due to the $1/x$ asymptotic behavior of the structure functions, it is convenient to rewrite previous Equation as

$$\sigma = \sum_{i,j,F} \int \frac{d\tau}{\tau} \int dy \int d\hat{\Phi}_F x_1 f_i^1(x_1, Q^2) x_2 f_j^2(x_2, Q^2) \frac{d\hat{\sigma}_{ij\to F}(\hat{s})}{d\hat{\Phi}_F}, \tag{3.2}$$

where $\tau = x_1 x_2$ and $y = 1/2 \ln(x_1/x_2)$. It is this formula which is implemented

with in GR@PPA. Both variables τ and y are generated as random numbers by the BASES package; τ from a $1/x$ distribution, y assumed to have a uniform probability distribution. The momenta fractions x_1 and x_2 derived from definitions of τ and y for use in consulting the PDF when returning the differential cross section matrix element. Access to the momenta fractions x_1 and x_2 can be obtained by inverting the expressions for τ and y. A sum over all matrix elements returns the total differential cross section.

As previously mentioned a process in GR@PPA may consist of incoherent subprocesses which are kinematically similar but possess different combinations of initial and final state partons. For instance "two-jet" production is computationally treated as a single process which includes all $q\bar{q}$, $qg(\bar{q}g)$ and gg processes with the different couplings and masses implemented as integration/differentiation variables.

The GR@PPA framework leaves it as a responsibility of the user to write the process interface, converting random numbers into kinematic variables for matrix element calculation. In particular care must be taken by process authors to deal with singularities in the integrals. The leptoquark production process including all incoherent subprocesses was implemented by John Rodgers Smith and Soushi Tsuno [30].

The mass dependent cross section for $VLQ3$ pair production can be seen in Figure 3.1. This plot also shows the separate contributions due to quark antiquark annihilation and due to gluon-gluon fusion. Yang-Mills couplings and a $Br(VLQ3 \rightarrow b\tau) = 1$.

m_{VLQ3} (GeV/c^2)	100	120	140	160	180	200	220	240
$\sigma_{VLQ3\overline{VLQ3}}\,(pb)$	898.4	324.5	132.1	58.55	27.59	13.60	6.928	3.614

m_{VLQ3} (GeV/c^2)	260	280	300	320	340	360	380	400
$\sigma_{VLQ3\overline{VLQ3}}\,(pb)$	1.911	1.035	0.562	0.307	0.169	0.093	0.051	0.028

Table 3.1: GRACE/GR@PPA cross section for $VLQ3$ pair production in $p\bar{p}$ collisions at $\sqrt{s} = 1.96$ TeV. The GRACE/GR@PPA matrix element generator is used with the Yang-Mills settings for the anomalous couplings $\lambda = \mu = 0$, and $Q^2 = m^2_{VLQ3}$.

3.3 Anomalous Couplings

The Blümlein model of the vector leptoquark includes two anomalous couplings, λ and μ. When $\lambda = \mu = 0$ the interaction reduces to a Yang-Mills coupling. The minimal $VLQ3$ coupling is achieved for $\lambda = 1$ and $\mu = 0$. The effect of this change over the full range was simply to shift the pair production cross section downwards. Both couplings were set to zero for the generation of event files produced by the GR@PPA vector leptoquark code. Throughout the rest of the analysis when efficiencies and systematics are cited for some given mass point, the sample used in the study was generated with the Yang-Mills settings. The cross sections for the Yang-Mills settings are detailed in Table 3.1.

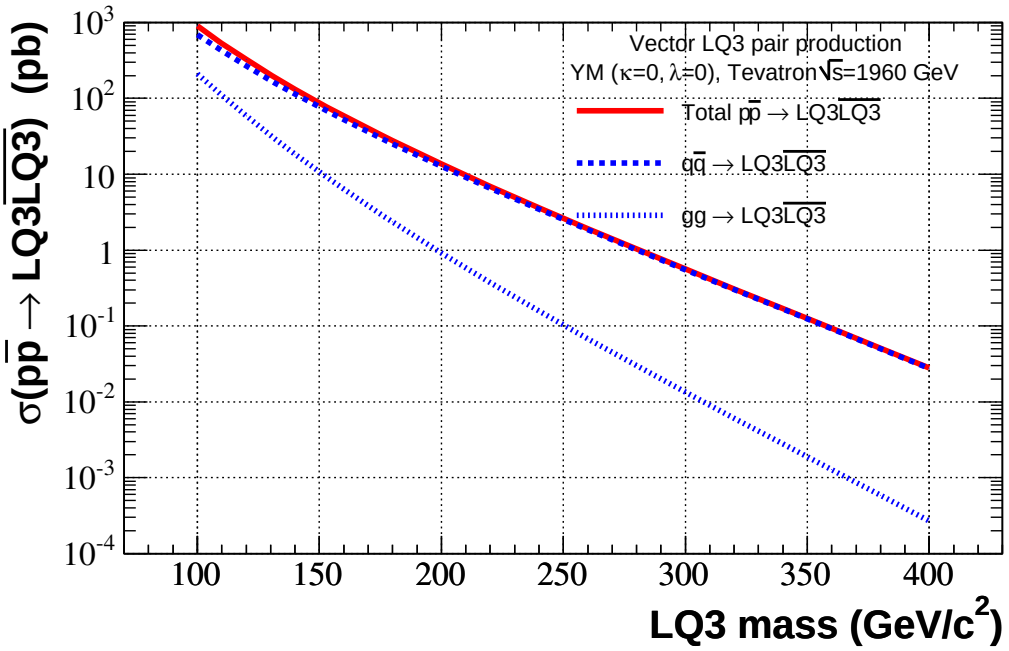

Figure 3.1: Pair production cross section as a function of $VLQ3$ mass (here referred to as LQ3) for the total (solid line), quark-antiquark annihilation contribution (heavy dashed line), and gluon-gluon fusion contribution (light dotted line). In these cases the generator uses Yang-Mills couplings and $\mathrm{Br}(VLQ3 \to b\tau) = 1$.

Chapter 4

Experimental Apparatus

The search for the vector leptoquark takes place at the Collider Detector at Fermilab (CDF) at the Fermi National Accelerator Laboratory in Batavia Illinois. Here we provide an overview of the accelerator complex in which colliding beams of protons and antiprotons are produced, and the instruments used to extract event data used in the search. The complete chain of events from a hydrogen molecule to proton or antiproton bunch colliding in the accelerator is described in the Tevatron Collider, Section 4.1. The CDF general physics detector is described in Section 4.2. We give a high level overview of the detector functions such as tacking, calorimetry, muon systems and the detector trigger systems. The data acquisition system, Section 4.3 covers the hardware and software functions needed to take voltages in thousands of data channels from the various CDF subsystems and turning them into event data stored and ready for use in analyses.

4.1 The Tevatron Collider

The Tevatron Collider is a proton-antiproton collider operating at a center of mass energy of $\sqrt{s} = 1.96$ TeV. Named for the "Tera electron volt" energies of its beams, the Tevatron is located at the Fermi National Accelerator Laboratory (Fermilab) in Batavia, Illinois, 35 miles west of Chicago. Here the term "Tevatron Collider" refers to the Tevatron accelerator itself, a superconducting magnet cyclotron and to the all of the infrastructure: proton source, antiproton source and various auxiliary accelerators, required to support the operation of the Tevatron accelerator.

One of the greatest accomplishments of high energy physics remains the 1995 observation of the top quark [1]. These observations were conducted by two of the experiments, CDF and D0, examining $p\bar{p}$ collisions at Fermilab. Other important if less dramatic work at both experiments deals accurate measurement of masses, cross sections and constraining the remaining free parameters of the SM. The Tevatron is currently the world's highest energy particle accelerator and the only place in the world where the top quark can be produced. In late 2007 the Large Hadron Collider (LHC) at CERN is scheduled for startup at energies and luminosities well beyond those available at the Tevatron. Until then the Tevatron remains the premier facility for the study of particle physics at the high energy frontier.

Below we give an overview of the portions of the accelerator complex required to support $p\bar{p}$ collisions. The progress of hydrogen to proton bunches, Section 4.1.1, and the antiproton source, Section 4.1.2, are covered in enough detail to understand the Tevatron Accelerator itself. That section is covered in greater detail as the specifics of the accelerator impact directly on the analysis and its

interpretation.

4.1.1 Accelerator Complex

A schematic of the various Fermilab accelerator components employed in supporting Tevatron collider operations is shown in Figure 4.1. Protons for the proton beam are obtained directly from H_2 gas [31]. Negatively charged through ionization, H^- is accelerated from the -750 kV storage dome to a grounded wall, where it enters a 150 meter linear accelerator. The LINAC is composed of a series of RF cavities which accelerate discrete bunches of particles to 400 MeV. A thin copper foil serves as a target for this beam and strips the electrons from the hydrogen leaving bare protons. The proton bunches then pass to the Booster. The Booster is a circular synchrotron accelerator 75 m in radius. It is here that the protons are boosted 8 GeV and passed on to the Main Injector.

The Main Injector is the third stage in the accelerating process. With seven times the circumference of the Booster the Main Injector is able to accelerate particles to either 120 GeV for use in the antiproton source or to 150 GeV for injection directly into the Tevatron. The Main Injector also has a role in supplying beam to a variety of other experiments located at Fermilab including the Switchyard for fixed target experiments [32], MiniBooNE [33] and NuMI [34].

4.1.2 The Antiproton Source

To obtain antiprotons, protons at 120 GeV are focused on a nickel target. Subsequent interactions create a shower of daughter particles among which are antiprotons. A lithium lens is first used to separate the beam of secondary particles by charge and then a charge mass spectrometry technique is used to separate

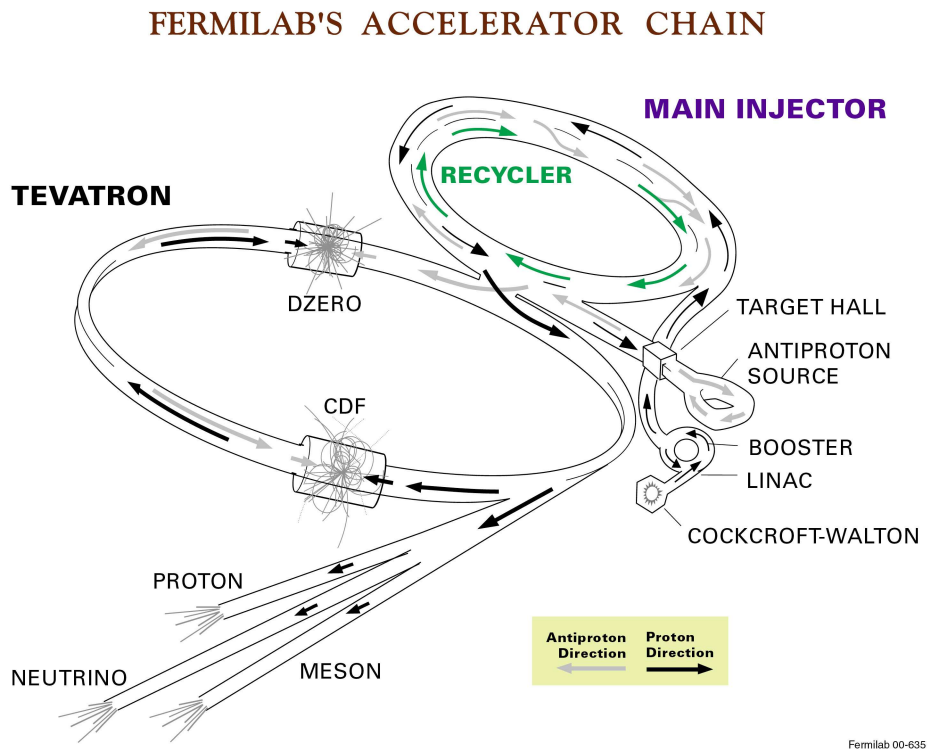

Figure 4.1: Schematic of the various Fermilab accelerator components employed in supporting Tevatron collider operations.

the antiprotons. The next stage is the Debuncher, the first of two synchrotrons which make up the antiproton source. As the synchrotron magnets in the Debuncher bend the particles into their orbits, higher energy particles travel in an orbit with a slightly larger radius. The longer travel time allows the Debuncher to apply varying acceleration via an RF cavity to accelerate the low momentum particles and to slow the high momentum particles. Spatial and time coherence is exchanged for momentum and energy coherence. By this process the Debuncher takes a beam of bunched particles and converts them into a continuous beam of antiprotons at 8 GeV.

The quality of the beam is further improved through a process called "Stochastic Cooling" It was the insight of Simone van der Meer (CERN) [35] that a

"Hot" beam or a beam possessing a large spread in momentum and energy could "cooled" by reading and correcting the deviations from an ideal orbit within the Debuncher. Corrections are made with an RF signal leaving narrower more focused beam.

The second synchrotron in the antiproton source is called the Accumulator. Pulsed RF injects antiproton bunches into the Accumulator which then uses it own RF cavities and Stochastic Cooling to incorporate the new antiproton bunch into the *"stack core"*. As implied by the name the function of the Accumulator is to store a beam of antiprotons in a high quality (low width momentum spectrum) state for hours until required for injection in to the main ring. The process of collecting and storing antiprotons is called *stacking*.

Until recently stacking rates have been limited by the size of the stack already in the Accumulator. Recently stacking rates of 20 mA/s in to an empty Accumulator have been achieved. However, this rate falls off rapidly with increasing stack size. To alleviate this, the recycler ring (yet another synchrotron) collocated in the same tunnel as the Main Injector is used to store antiprotons, clearing the Accumulator for higher stacking rates.

In conjunction with the operation of the recycler a new process called electron cooling takes place within the recycler [36]. An electron beam at energy 4.3 MeV and 0.5 A with a low momentum spread is placed in the presence of an 8.9 MeV antiproton beam already present in the recycler. The two beam are brought into proximity over the space of 20 meters. During that time the antiproton beam can be thought of as being situated in an electron gas with which it under goes Coulomb scattering. Antiprotons with the highest deviation from the average momentum profile under go the largest momentum transfers in these interactions. The electrons which now have a high momentum spread are

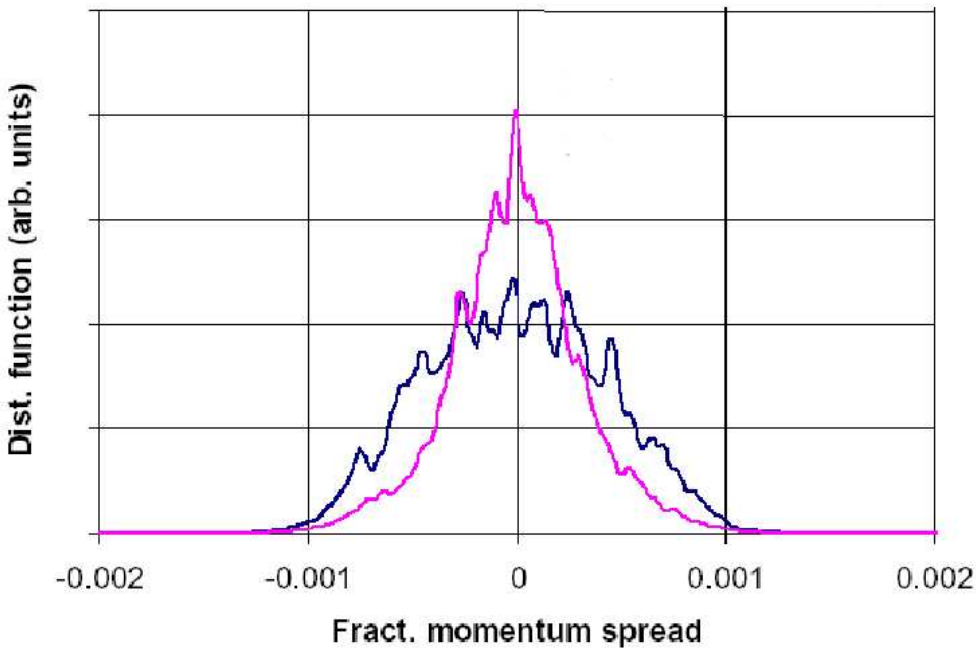

Figure 4.2: Effect of electron cooling within the recycler. The wider or blue plot is the momentum profile for the original beam and the more central or pink plot is the momentum profile for the conditioned beam.

collected and reconditioned in a separate system. As the antiproton beam continuously cycles through the recycler the momentum spread of the beam drops. Figure 4.2 shows the change in effect of electron cooling after a 15 minutes of operation of the electron cooling apparatus for an antiproton beam containing 6.5×10^{10} particles and the electron cooling beam at 200 mA [37].

4.1.3 Tevatron Accelerator

The Tevatron proper is the largest synchrotron on the Fermilab site. The ring is 1 km in radius and is visible from the surface as a large earthen berm with evenly spaced pump houses. The actual installation of the Tevatron accelerator is in a tunnel approximately 2 stories underground. The accelerator itself is a superconducting magnetic synchrotron. The superconducting magnets are made

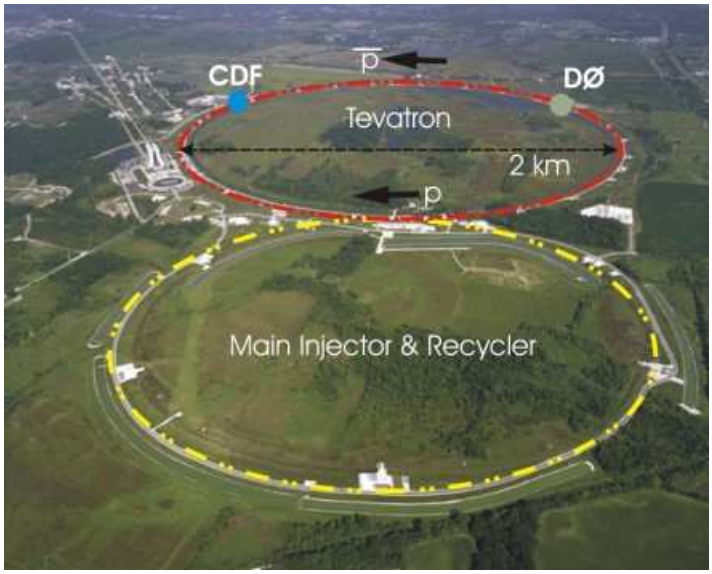

Figure 4.3: An aerial view of the Tevatron, Main Injector and locations of the CDF and D0 experiments.

of niobium/titanium and in operation are kept at a temperature of 4.6 K with liquid helium. Superconducting magnets are used as they eliminate the resistive heating, allowing magnet designs with greater currents and therefore greater magnetic field strengths.

During operation beams of protons and antiprotons ($p\bar{p}$) are accelerated to to 0.98 TeV. Both beams are contained within the same beam pipe and utilizing the same magnets the two oppositely charged beams counter-rotate with the proton beam moving clockwise as viewed from above. During data taking the beams are made to cross at various experimental sites. The resulting collisions take place head on and nearly all the beam energy is available in the laboratory frame for the production of particle species.

Injecting protons and antiprotons into the Tevatron is a process called *shot setup*. During shot setup various transfer lines are configured to inject bunches of protons at 150 GeV. These bunches are injected with a 396 ns separation into

three trains of 12 bunches each. Each bunch contains roughly 2.2×10^{11} protons. A 2.617 μs abort gap is established between the trains. Antiprotons are injected in a similar manner in the opposite direction allowing for the opposite charge. Antiproton bunches are typically a factor of 10 smaller than proton bunches. The beams are kept on separate helical orbits to ensure separation in the beam tube.

With bunches of protons and antiprotons in the Tevatron at 150 GeV a condition called *front porch* has been reached. RF cavities in the Tevatron then ramp up both beam energies to 980 GeV. A stable state of protons and antiprotons at 980 GeV is called a *store*.

The Tevatron ring contains several interaction points where the beams can be made to interact. One of these points, called B0, is the location of CDF. At the interaction points magnets, called low beta quads are used to take the beams off their helical orbits. The beams are allowed to cross and collisions occur.

The collision rate is given by

$$R = \sigma_{int}\mathcal{L}, \tag{4.1}$$

where σ_{int} is the interaction cross section and $\mathcal{L}$ is the instantaneous luminosity. The instantaneous luminosity $\mathcal{L}$, is a function of the revolution frequency f, the number of bunches in the beam n, the number of particles per bunch N_a and N_b and the cross sectional area of the beam A,

$$\mathcal{L} = \frac{fnN_aN_b}{A}. \tag{4.2}$$

Luminosities achieved at the beginning of every store in Run II through 24 November 2006 is displayed in Table 4.4. The value plotted is the average value

as reported by the CDF and DO experiments. Weekly totals for integrated luminosity since the beginning of Run II are displayed in Table 4.5 in green. The accompanying blue plot shows the cumulative or total integrated luminosity. This latter plot represent delivered luminosity which may differ from integrated luminosity as recorded at each of the experiments. Operational status of either of the experiments may preclude data taking for several minutes to several hours in the case of a major hardware failure.

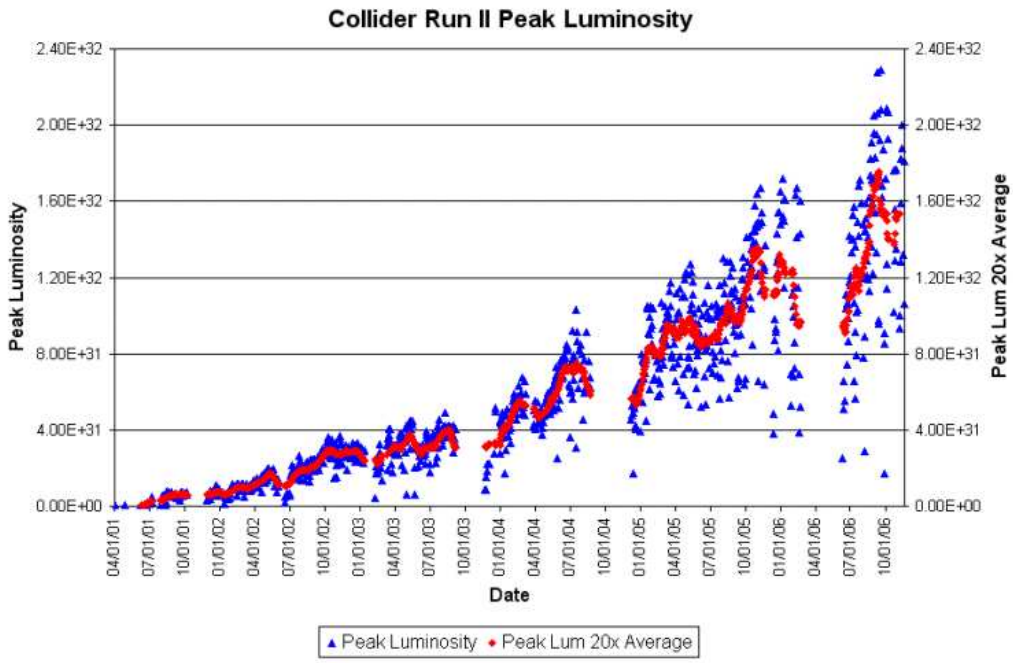

Figure 4.4: Tevatron initial instantaneous luminosities for all stores in Run II of the Tevatron through 24 November 2006 shown in small blue triangles. Data points are an average of those reported by CDF and D0 experiments. Instantaneous Luminosities are measured in units of $cm^{-2}sec^{-1}$.

A store is consumed by both particle interactions and increases in bunch emittance due to intra-beam scattering. Particle interactions is the dominant effect at the beginning of a store. Later in the store when the ratio between p and $\bar{p}$ ratio has increased, intra-beam scattering causes the emittance to increase

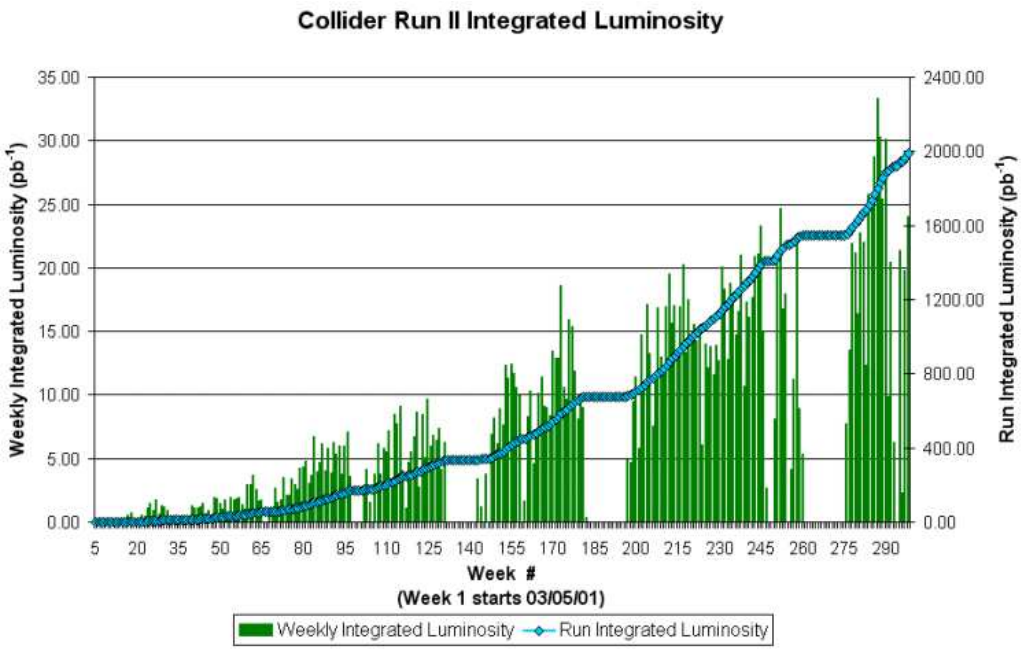

Figure 4.5: Tevatron weekly integrated luminosities for Run II of the Tevatron as reported by Fermilab beams division. This graph represents every week of Run II Tevatron operations through 24 November 2006. The solid curve indicates integrated luminosity.

and antiproton losses becomes near exponential. Typically, by the time a store is ended the accelerator operators have readied a new stack of antiprotons and shot-setup can begin.

4.2 CDF

The Collider Detector at Fermilab (CDF) is a multipurpose detector used to study a wide range of physics processes occurring in high energy $p\bar{p}$ collisions. CDF combines charged particle tracking and timing, projective calorimetry and muon detection systems. The exotic species of particles and interactions of interest decay quickly to more stable objects: electrons, muons, photons and jets that traverse the detector. High quality measurements of the energy, momentum,

origin and trajectory of these objects allow reconstruction of the underlying events and shed light on the processes involved. A multilevel trigger system is used to help recognize these high quality events so they can be written to tape for later analysis.

Proton antiproton collisions are not restricted to the exact geometric center of the CDF detector. The Tevatron beams possess a transverse particle density which is roughly Gaussian, and a cross sectional area on the order of millimeters. Center to center separations between the proton and antiproton bunches are also on the order of millimeters. In order to provide collisions the beams are taken off their helical orbits by magnets called "low beta quads" well outside the detector volume. The bunches of protons and antiprotons must then traverse tens of meters to before reaching the exact center of the detector. The beams are effectively overlapping (and colliding) at significant rates out to $\pm 100cm$ of the nominal interaction point. Typically events with primary vertices, e.g. initial $p\bar{p}$ interactions are accepted out to ± 60 cm along the beam axis from the geometric center of the detector. Figure 4.6 illustrates the z_0 distribution of primary vertices.

The natural symmetry about the beam axis is expressed in the cylindrical design of CDF. The detector is both forward and backward symmetric about the nominal interaction point and is azimuthally symmetry about the beam axis. The CDF coordinate system is a right-handed system with the origin taken at the center of the CDF detector. The z-axis is taken along the proton beam, West to East, the y-axis points vertically upward, and the x-axis points radially outward from the Tevatron ring. The polar angle θ and the azimuthal angle ϕ are defined as follows: θ is measured with respect to the positive z-axis and $\phi = 0$ is along the positive x-axis with ϕ increasing toward the positive y-axis.

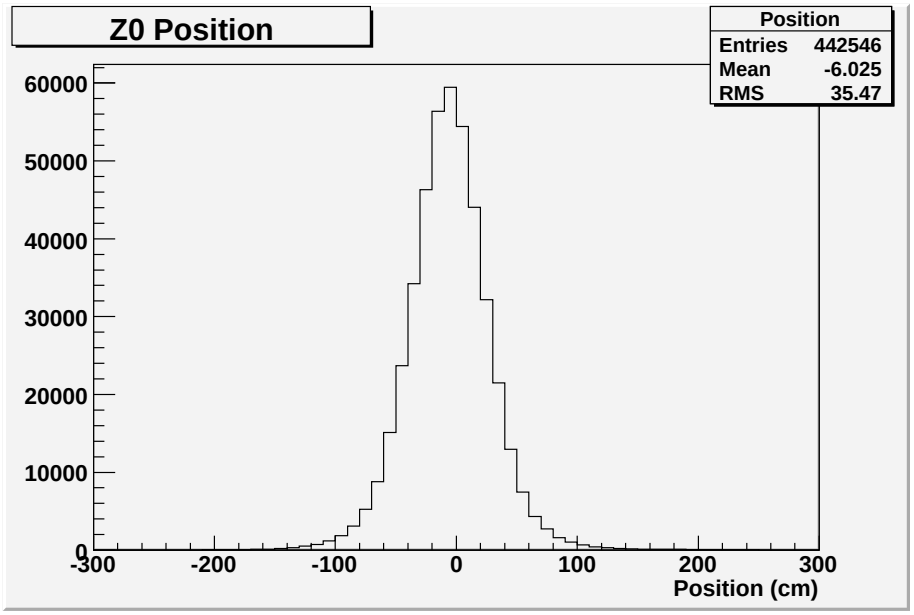

Figure 4.6: Primary vertex z_0 position extends well beyond the nominal interaction point at $z_0 = 0$. Appreciable rates of events out to ± 100 cm are recorded. In practice removal of events with $|z_0| \geq 60$ cm are routinely cut. This plot was taken from the monitoring of live data during run 220604 at 2:14 a.m. 29 July 2006.

The Tevatron accelerates both the proton and antiproton beams to near the speed of light. Due to high momentum along the z direction a convenient system for analysis is one in which the distribution of particles $dN/d\theta$ is a Lorentz invariant. The rapidity is defined for a collision produced particle with energy E and longitudinal momentum p_z,

$$y = \frac{1}{2} \ln \left(\frac{E + p_z}{E - p_z} \right) + \mathcal{O}(\epsilon^2). \tag{4.3}$$

The rapidity transforms under boost $\beta \equiv v/c$ as $y \rightarrow y - tanh^{-1}(\beta)$ and is a Lorentz invariant [38]. For the Tevatron, the particle energy $E >> mc^2$ and the particle momenta $E/c \simeq \sqrt{p_T^2 + p_z^2}$, the rapidity Equation 4.3 is approximately the psuedorapidity, Equation 4.4.

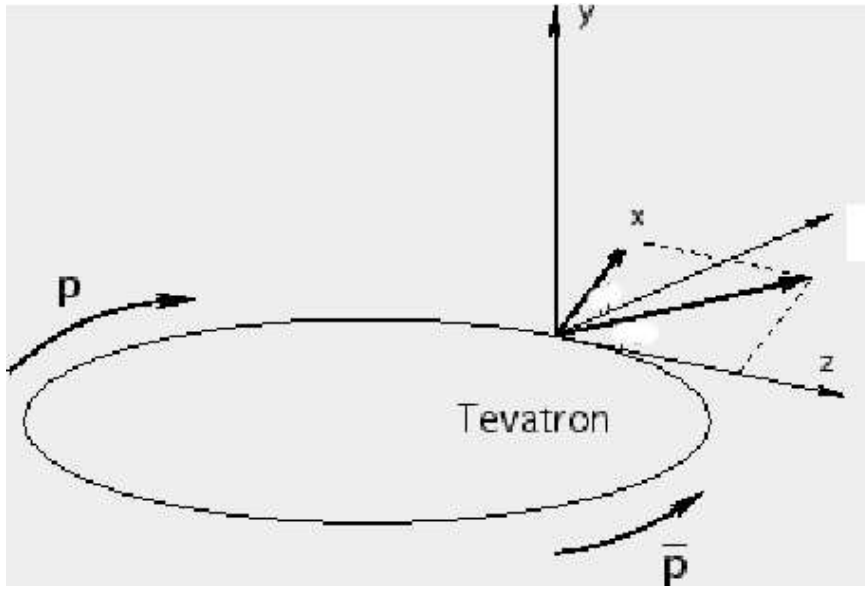

Figure 4.7: The CDF coordinate system with respect to the Tevatron.

$$\eta = -\ln\left(tan\frac{\theta}{2}\right) \tag{4.4}$$

The opening angle between two particles is expressed by

$$\Delta R = \sqrt{\Delta\eta + \Delta\phi}. \tag{4.5}$$

In describing CDF it is helpful to group the detector subsystems into three main assemblies that accomplish related measurements. Moving radially outward from the beam line:

- The tracking system uses semiconductor and gas detectors for time of flight and charged particle detection and momentum measurement within the magnetic field.
- Calorimetry detectors lie just outside the solenoid and provide a measure of energy deposited by charged and neutral particles.

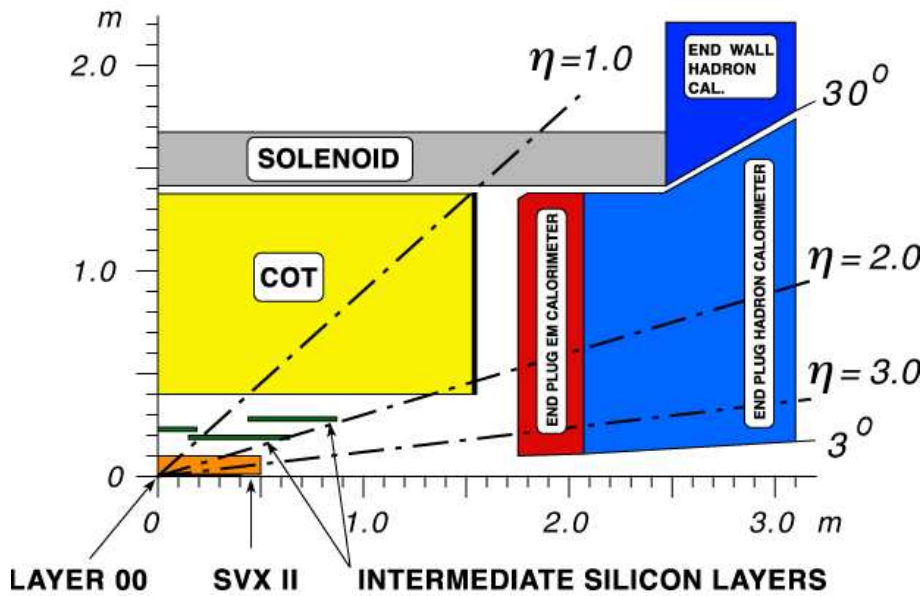

Figure 4.8: An illustration of the η coordinate of various components.

- Muon detectors outside the calorimeters measure the position of charged particle principally muons as other particles are typically absorbed by the material or the calorimeter.

In the following sections these assemblies are discussed in detail.

4.2.1 Tracking

Measuring 4.8 meters longitudinally and 1.5 meters in radius, the tracking volume contains the Silicon Detector, the Central Outer Tracker (COT) and the Time of Flight Detector (TOF). The tracking volume is immersed within a superconducting solenoid providing a 1.4 Tesla magnetic field collinear with the beam line.

The tracking system is discussed in more detail below but a quick overview follows.

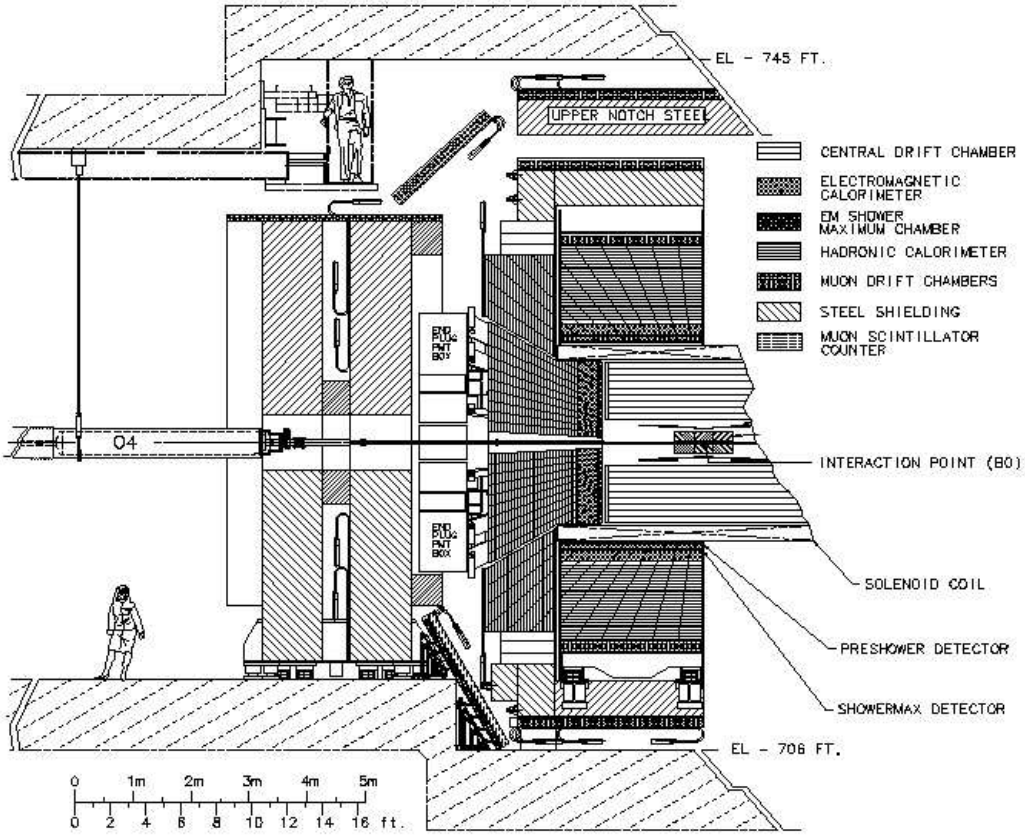

Figure 4.9: CDF detector longitudinal view with components clearly labeled. A figure standing next to the detector is provided for scale.

- The Silicon Detector collects ionization charges as particles pass through multiple layers of biased semi-conductor. This detector provides enough resolution to conduct secondary vertex reconstruction.

- The COT is an open cell drift chamber. Particle tracks are reconstructed from ionized charges collected on sense wires.

- The Time-of-Flight (TOF) detector provides time and pulse height measurements from bars of plastic scintillator mounted axially on the outer edge of the COT volume.

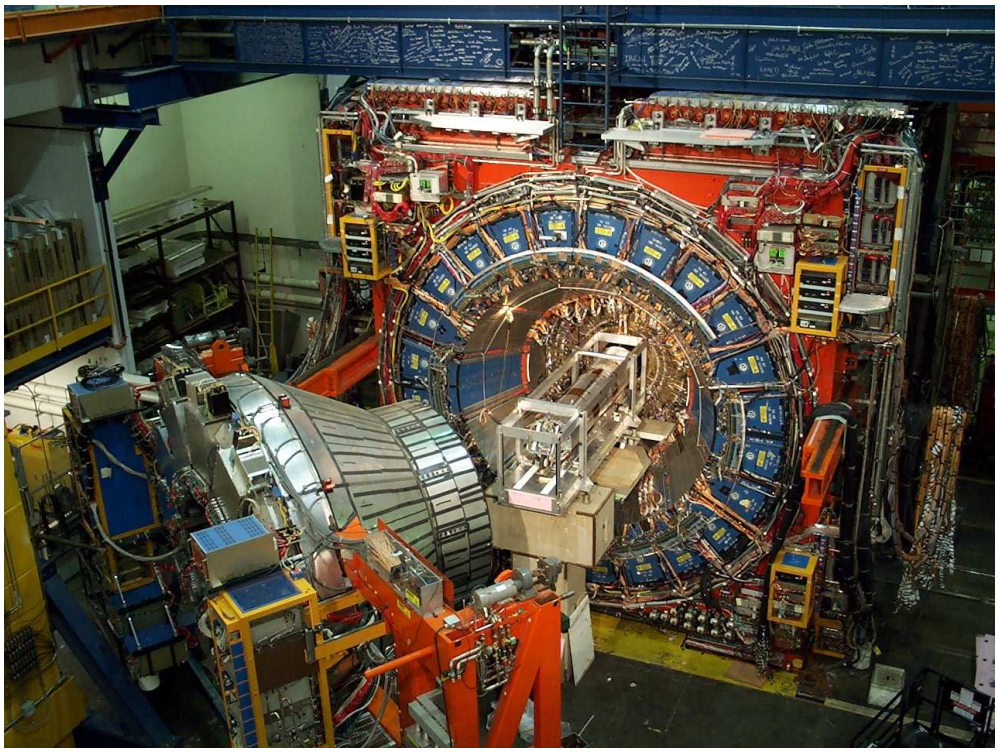

Figure 4.10: Photograph of the CDF detector in the assembly hall during construction. Note the geometry of the central and end plug calorimeters clearly points towards the nominal interaction point. The blue sectors arranged in a ring define the 24 ϕ sectors of the central calorimeter. The COT, masked in gold colored Kapton cables is nested inside the detector bore surrounded by the calorimeters. The Silicon detector is shown during the process of installation.

The Time-of-Flight (TOF) detector while not use in this analysis deserves a brief mention. Particle identification is performed by measuring the time of arrival of a particle at the scintillator with respect to the collision time. Time and pulse height measurements are provided by Photo Multiplier Tubes (PMTs) and bars of plastic scintillator mounted axially on the outer edge of the COT volume. The particle mass m can then be determined based on it momentum p, path length L and time of flight t,

$$m = \frac{p}{c}\sqrt{\left(\frac{ct}{L}\right)^2 - 1}. \tag{4.6}$$

The time of flight is measured with a resolution of $\sim 130\ ps$ providing the capability to distinguish between $K^{\pm}$ and $\pi^{\pm}$ hadrons up to 5 GeV [39]. The $K^{\pm}$ is a massive long lived particle with $c\tau = 3.71$ m which can hope to reach the radius of the TOF, but because of it mass will experience a significant delay with respect to the lighter $\pi^{\pm}$ in reaching that point. The instrument is of limited utility for particles with $p_T > 5$ GeV/c, which arrive at the TOF detector at essentially same time and are thus indistinguishable with in the output from this instrument. The implication is that while the TOF detector has an application in identifying massive long lived particles, this detector is not employed in searches for massive short lived particles characterized by low mass decay products possessing high p_T. In the case of this analysis, the vector leptoquarks are massive and short lived.

4.2.1.1 The Silicon Detector

The Silicon Vertex Detector (SVX) is the largest operating silicon detector in high energy physics. This instrument is a semiconductor tracking device intended for secondary vertex reconstruction. The small dimension of design elements on the surface of a semi-conductor means a silicon based detector can be placed closer to the nominal interaction point without sacrificing detector granularity, e.g. a 25 μm feature at 2.45 cm subtends the same angle in the transverse plane as a 3 mm feature at 3 m. Combined with the higher density of material with which charged particles can interact, this means that a semiconductor design can be substantially smaller than a drift chamber based tracking system.

Charged particles from $p\overline{p}$ collisions interact with the materials they penetrate leaving a trail of ionized charges in their wake. Within a doped semiconductor material this takes the form of liberated electron-hole pairs which are free to move about the semiconductor lattice. The silicon sensors are designed such that when a bias voltage is applied these charges are collected in narrow channels (strips) of n and p-type materials. Associated electronics read out the collected charge. A *hit* on the sensor is registered if the collected charge exceeds threshold, also called the pedestal value. A pattern of multiple hits in different radial layers indicates the passage of a charged particle and is referred to as a track. With a pitch or spacing between channels of as little as 25 μm, silicon sensors provide excellent spatial resolution in a small instrument. If radiation hardness issues are controlled the instrument can be placed close to the interaction point. The extension of the expected service life of the silicon detector to the end of CDF Run II has raised this issue from to a top priority for those maintaining the instrument, see Section 5.

The silicon sensors are composed of 300 μm thick (275 μm in ISL) wafers of n-type high resistivity bulk silicon. Parallel strips of p-type semiconductor form the sensor channels. The geometry of the silicon strips is axial to collect $r - \phi$ tracking information. The reverse side of the sensor is either either "90 degree stereo" or small angle stereo, $\pm 1.2^o$ to collect $r - z$ tracking information.

The basic operational component of the silicon detectors is a ladder. A ladder contains six silicon sensors, electrically bonded and glued to a carbon fiber backing. Integrated circuits, SVX3D chips are mounted at the end of each ladder to provide for read out.

The SVX3D is a custom designed radiation hard CMOS integrated circuit. The design contains 128 parallel analogue inputs and an 8 bit digital output bus. Channels contains a preamplifier, analogue delay pipeline, ADC (8 bits) and data sparsification logic. Deadtimeless mode -simultaneous acquisition, digitalization and readout operation. Figure 4.16 shows a magnified photograph of the SVX3D with the functional areas labeled.

Silicon strip sensors are used in three detector subsystems located near the center of the tracking volume, see Figure 4.11. Layer 00 (L00) contains a set of single sided silicon sensors mounted directly on to the beam pipe. The Silicon Vertex Detector (SVXII) contains 5 double sided ladders arranged in 12 azimuthal *wedges*. All ladders at a given radius are referred to as a *layer*. The Intermediate Silicon Layer (ISL) lies outside of the SVXII and extends coverage out to $|\eta| = 2$. The ISL support frame work also supports the SVXII and the Port Cards, a portion of the silicon data acquisition system. Figure 4.12 shows the radial placement of the silicon detector subsystems.

The nomenclature for naming individual ladders is of the form **SB0W9L3**. This translates into S for SVXII, B0 means barrel 0, W9 stands for wedge 9 and L3

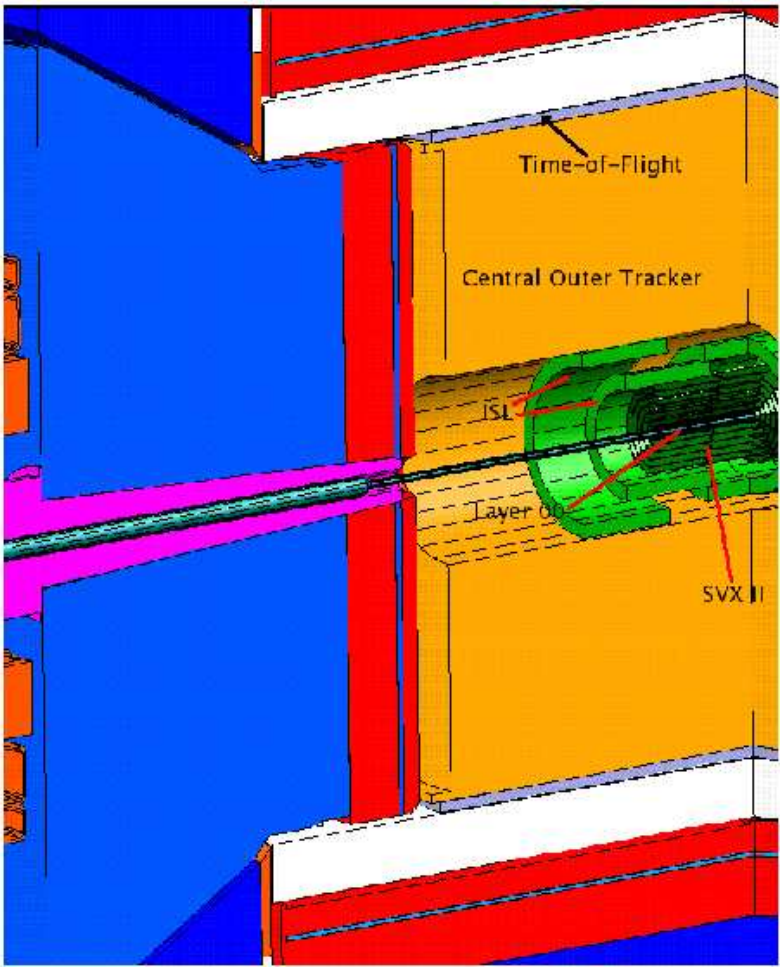

Figure 4.11: Placement of CDF tracking system components. Silicon components are in green, COT is in orange and the TOF is in blue.

means layer 3. Wedges 10 and 11 are labeled "WA" and "WB" respectively. For L00 and ISL ladders the leading "S" is replaced by an "L" or an "I" respectively

Layer 00: is a single sided silicon strip detector mounted on the beam pipe at radius of 1.35 cm and 1.6 cm and is 80 cm in length Figure 4.13. Mounting the instrument directly on the beam pipe improves impact parameter resolution and provides redundancy in the event that the innermost layer of SVXII becomes unusable from radiation damage. Due to the radiation tolerant design, L00 is expected to remain serviceable through 7.4 fb of integrated luminosity. The

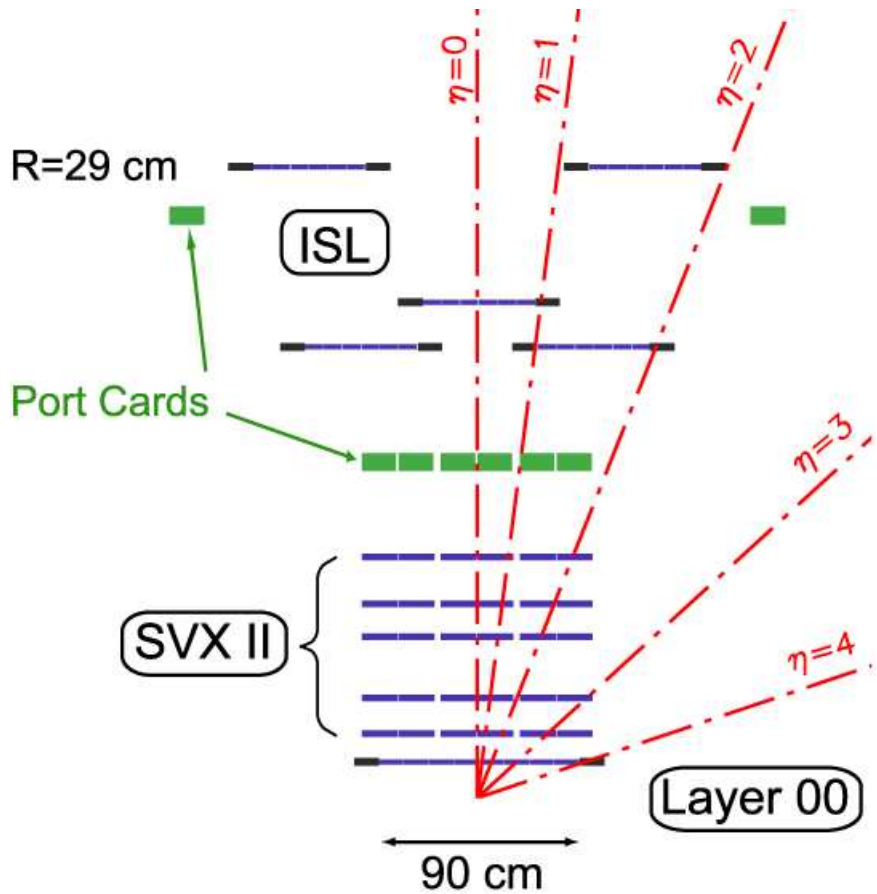

Figure 4.12: Radial placement of L00, SVXII and ISL detector components. Please note that the longitudinal and radial scales do not match.

radiation hardening is accomplished in part with an axial strip design using guard structures to minimize the effects of leakage currents which will increase with the received dose. L00 silicon sensors have an implant pitch of 25 μm and a readout pitch of 50 μm achieved by reading out every other strip.

Silicon Vertex Detector II: In SVXII the silicon sensors are arranged into *half-ladders*. Five half-ladders of increasing width make a 12 degree *wedge*. Twelve azimuthal wedges make a *barrel* and six barrels complete the SVXII detector.

As the width of each layer increases so do the number of channels to be read

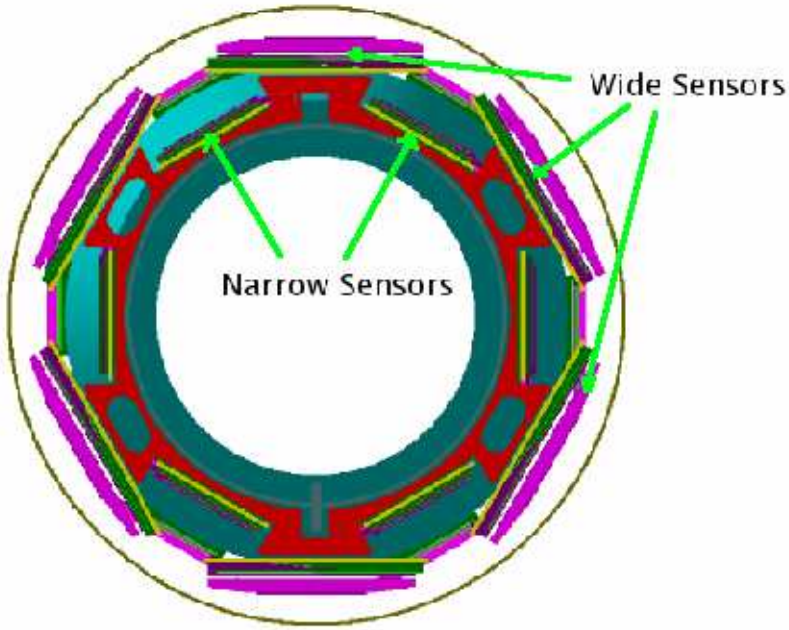

Figure 4.13: Layer 00 end view showing the alternating wide and narrow sensors.

out. Moving outwards from layer-0 there are 4, 6, 10, 10 and 14 SVX3D chips on each ladder. The Port Cards located at the periphery of the bulkheads, interface the hybrids and front end chips with the rest of the readout data acquisition system.

The SVXII layers are is located at radii of 2.45 cm to 10.6 cm. The length is 96 cm in the z coordinate centered on the nominal interaction point. Figure 4.14 shows the SVXII detector during construction with the wedge and layer structure explicitly displayed. Support for all of these components is provided by beryllium bulkheads.

The SVXII sensors were fabricated by two manufacturers. Hamamatsu Photonics (Hamamatsu City, Japan) manufactured the layers 0, 1 and 3. These are "90 degree stereo" layers, meaning the sensor strips on the $r - \phi$ and $r - z$ sides of the sensors are perpendicular to each other. the 90 degree layers have an ad-

ditional layer of insulator and readout strips in the double-metal configuration. These strips carry the z signals to be readout by the SVX3D chips. Micron Semiconductor (Lansing, Michigan) manufactured layers 2 and 4 with a small angle stereo configuration. In this configuration the $r-z$ side sensor strips are offset by -1.2 degrees and +1.2 degrees. The Micron sensors utilized a 6 inch wafer technology which had, at the time of manufacture recently become available. The Hamamatsu "90 degree stereo" ladders were created with an older 4 inch wafer technology to preclude the manufactured from having to deal with two innovations at once [40]. A summary of SVXII design details by layer are listed in Table 4.1 [41].

Figure 4.14: SVX II during assembly. End view explicitly illustrates the wedge and layer structure of the instrument.

	Layer 0	Layer 1	Layer 2	Layer 3	Layer 4
# ϕ strips	256	384	640	768	896
# z strips	512	576	640	512	896
stereo angle	90°	90°	$+1.2^o$	90°	-1.2^o
ϕ pitch (μm)	60	62	60	60	65
z pitch (μm)	141	125.5	60	141	65
Active Width (mm)	15.40	23.80	38.34	46.1	58.18
Active Length (mm)	72.43	72.43	72.38	72.43	72.38
detectors	141	141	141	141	141

Table 4.1: Silicon sensor properties by SVX II layer.

Intermediate Silicon Layer: ISL consists of five additional layers of silicon detector extending silicon tracking out to $|\eta| = 2.0$. In the central region there is a single layer with coverage $|z| \leq 20$ cm at radius 22 cm. There are two additional layers at radii 20 cm and 28 cm covering at either end of the ISL detector. Placement of these layers is such that the outer edge is at $|\eta| = 2.0$.

ISL ladders are composed of six sensors arranged as half ladders of three sensors each. The three sensors are bonded to form a single electrical unit and mounted on a carbon fiber support. The greater radial position of ISL results in both a lower occupancy and lower radiation dose rate. This enables a longer strip length and a fixed strip pitch of 112 μm on both the axial and small angle stereo (1.2 degrees) sides. This reduces the number of read out channels to about half that of SVXII.

Silicon Readout System: The Silicon Data Acquisition (Si-DAQ) system is represented in Figure 4.15. A brief description of the Si-DAQ read out sequence follows.

Charge collected on the silicon sensor strips is sampled by the "Front end" or analog input section of the SVX3D chip and stored in the analog pipeline. The pipeline contains 47 cells. Of these 42 cells form the event buffer. There are also 4 cells which can be reserved pending a signal called Level-1 Accept. The remaining cell stores the pedestal value set at chip initialization and which is used to determine threshold for this channel. When Level-1 accept is received the corresponding position in the pipeline is flagged as reserved so that cell will not be overwritten by a subsequent event. The magnitude of the stored signal is converted to a digital signal with an 8 bit Wilkinson ADC. There is a separate ADC for each of the 128 channels on the chip. Additional control signals cause the chip to digitize and read out the signal. Data from all chips on a single ladder are combined by reading the output from each chip sequentially. This data stream is sparsified, meaning in that only channels above a threshold are read out a practice also referred to as zero suppression. The SVX3D chip Figure 4.16 shows the various functional areas of the chip.

The notable features of the SVX3D chip are that it is *Deadtimeless*, meaning that data continues to be taken even as earlier events are digitalized. Data acquisition and digitalization occur simultaneously and the design can be implemented in a radiation hard process.

Illustrated is the same figure in the top row are a single wedge with 5 layers and 44 SVX3D readout chips. A Port Card (top right) serves five ladders or a single wedge. It acts as a gate keeper between the initialization and control signals sent to the set of chips on a particular ladder and the data stream coming from the ladder. A Port Card is pictured in Figure 4.17.

The Port Card also converts the electrical signal carrying the data to an optical signal via the use of DOIMs or *Dense Optical Interface Modules* [42].

The DOIMs are used in order to replace copper conductor readout cables with fiber optic ribbon. The advantage of using fiber optic is that the material is low mass and features a high bandwidth for data transmission in a harsh radiation environment. Each DOIM on the Port Card serves a single ladder with a byte-wide fiber optic readout. A schematic of the DOIM optical system is shown in Figure 4.18. Transmitter and receiver DOIMs are pictured in Figures 4.19 and 4.20 during testing.

Fiber Interface Boards or FIBs (bottom row far left) are contained in crates mounted in the collision hall. Each FIB serves two wedges/Port Cards or up to ten ladders. Not all channels will be used in FIBs serving the ISL and L00 systems. Each FIB is connected to a VRB via the back plane of the equipment crate. VRB stands for VME Readout Buffer, while VME simply refers to a manufacturer's equipment standard. The FIB retransmits the data stream on high speed (1.5 GHz) serial fiber cables. This signal is received by a VME boards outside the collision hall. There the data enters the CDF DAQ system along with data from the other detector instruments.

Silicon Power Supplies: Power is delivered to the silicon detector ladders and Port Cards by 114 CAEN SYS527 power supplies. Each ladder has a common 5 and 10 volt current supplied to all of the SVX3D chips on a ladder. Ladder bias voltages used to deplete the silicon are individually set with a voltage divider. The eight CAEN power supply crates, containing between 5-12 modules each are mounted peripherally around the collision hall itself. Several of the CAEN crates have been moved out of the plane of the Tevatron beam to minimize beam interference with the sensitive electronics.

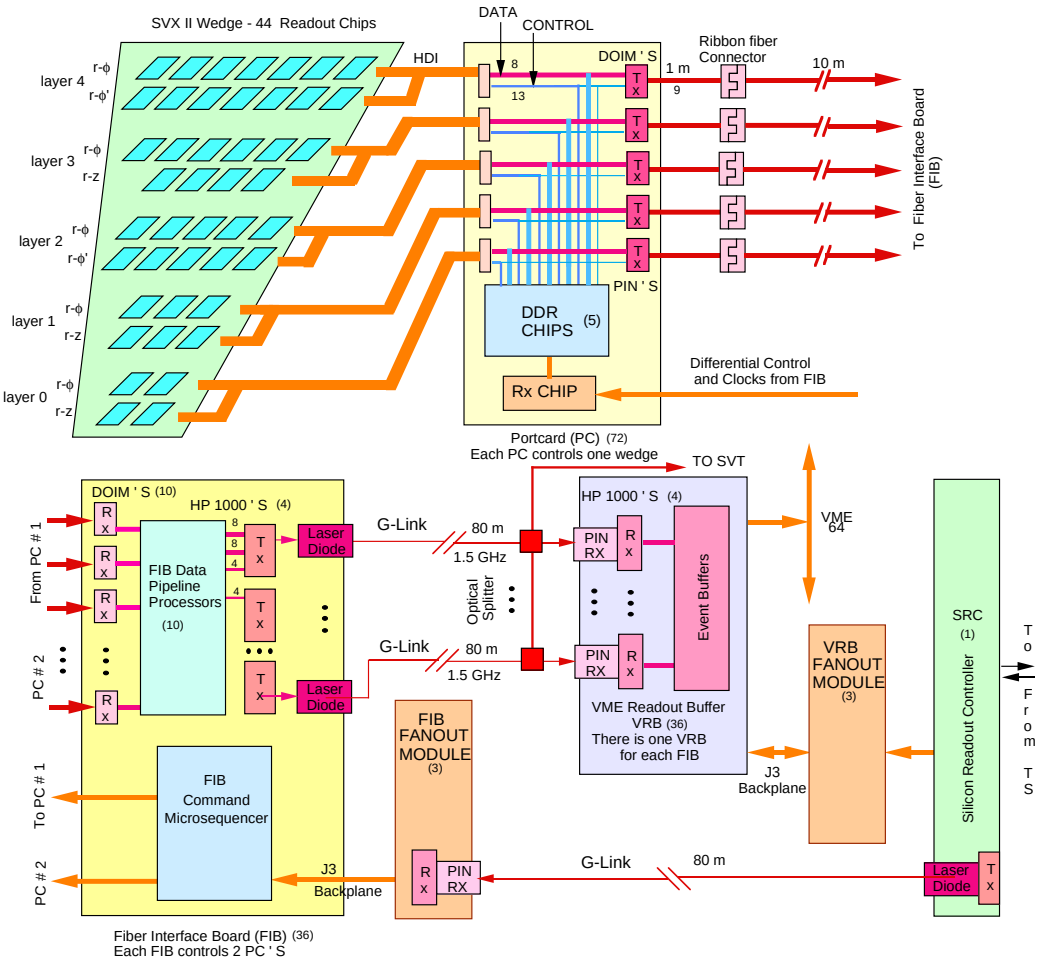

Figure 4.15: The top row of the silicon readout electronics are generally inaccessible within the detector volume. The bottom row shows the accessible portions of the Si-DAQ.

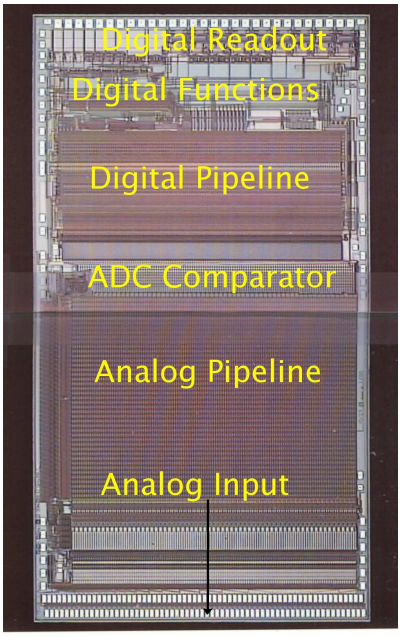

Figure 4.16: Photograph of the SVX3d chip with functional areas from analog input near the bottom to digital readout near the top labeled.

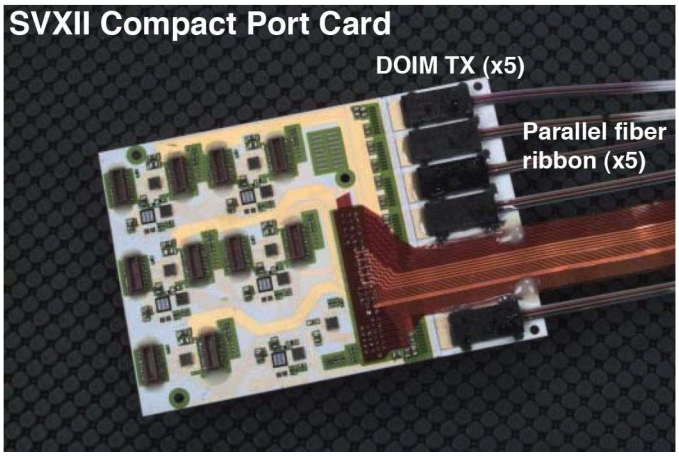

Figure 4.17: Port Card shown with five mounted DOIMs, one per ladder. The optical fibers from each carry 8 parallel bits to a similar receiver DOIM (RX) on the FIB card.

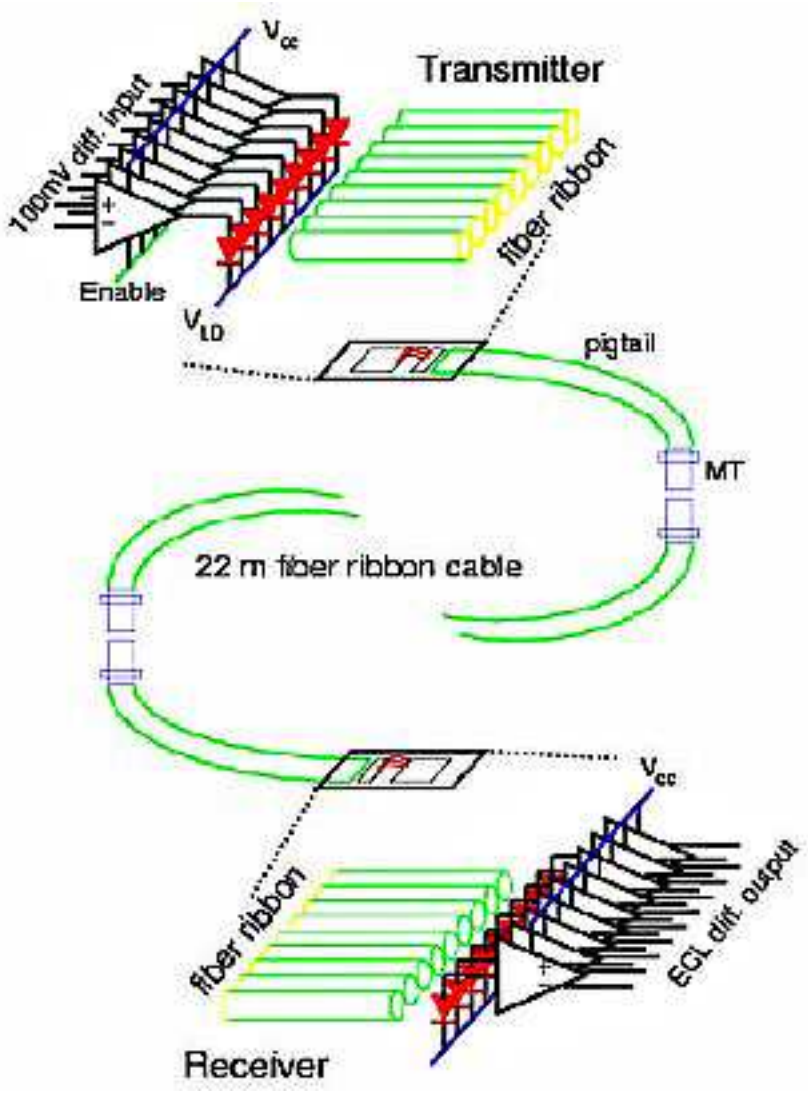

Figure 4.18: Schematic of the DOIM system

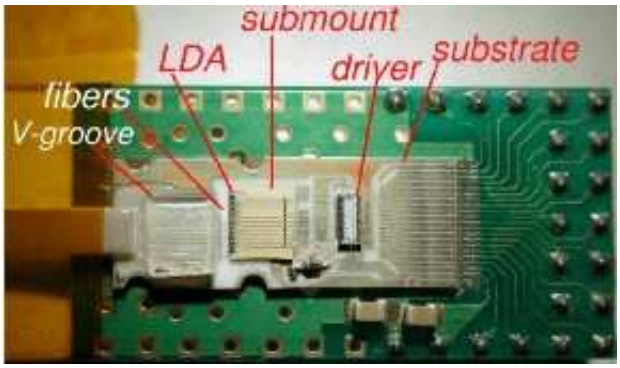

Figure 4.19: Disassembled transmitter or TX DOIM which converts an eight bit readout signal from a ladder and converts it to an optical signal for transmission out of the detector volume.

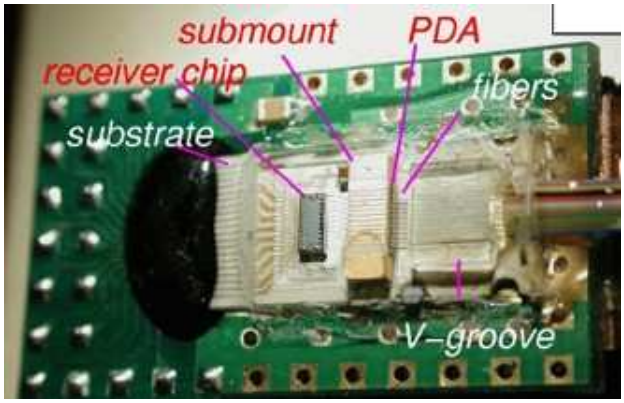

Figure 4.20: Disassembled receiver or RX DOIM which converts an eight bit optical signal transmitted from the Port Cards inside the detector volume back to an electrical signal.

4.2.1.2 The Central Outer Tracker

The Central Outer Tracker (COT) [43] is an open cell drift chamber covering the full ϕ range and $|\eta| \leq 1.0$ (ref tech design report) and p_T as low as 400 MeV/c. The active volume spans 310 cm parallel to the beam axis and from radius 44 cm to 132 cm. Charged particles transversing this volume ionize the gas mixture contained within leaving a trail of electrons and positive ions. By measuring the time needed for charges to collect on a sense wire the position of the charged particle track can be determined.

The COT is filled with an active gas mixture which ionize with the passage of a charged particle and then quickly return to its ground state in time for the next bunch crossing. By design the COT has a 100 ns drift time, from ionization to measurement, well below the 396 ns bunch spacing. The COT was originally designed to operate with a gas mixture of 50% Argon, 35% Ethane and 15% CF_4. This mixture has been since modified with the addition of a small amount of oxygen to correct hydrocarbon degradation encountered beginning in 2004 [44]. By function, argon is the ionization gas, ethane acts as a quench gas allowing the Argon to return to its ground state, while presence of CF_4 increases the electron drift velocity.

The COT contains 30,240 sense wires mounted on two precision machined aluminum end plates. Eight superlayers (SL1-8) are arranged radially with superlayer 1 the inner most and superlayer 8 the outermost, Figure 4.21. The superlayers alternate axial and stereo configurations. Axial superlayers have sense wires strung parallel to the beam axis providing tracking information in the $r - \phi$ plane. Stereo information is provided by sense wires mounted on $\pm 2^o$ angle and provide a limited amount of information in $r - z$ plane.

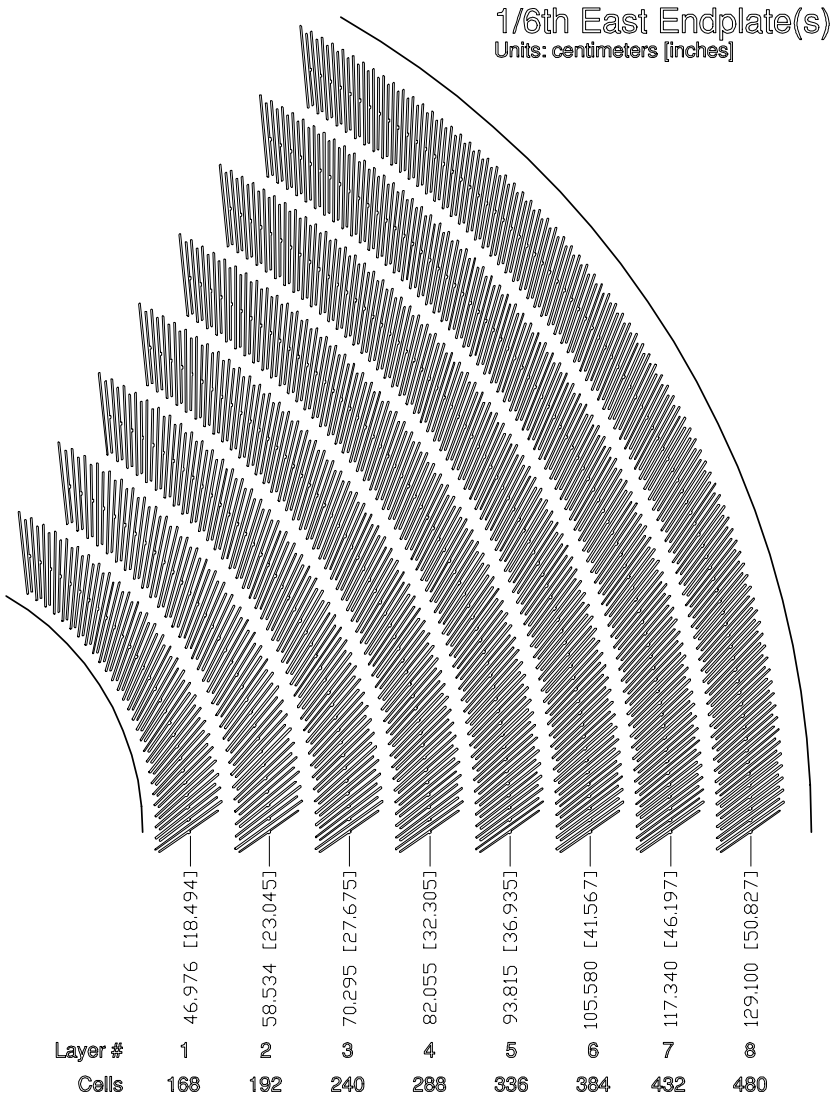

Figure 4.21: Diagram of 60° of the East Central Outer Tracker (COT) endplate showing all 8 superlayers.

Superlayers are further divided into supercells. Three supercells are shown in Figure 4.22. Each supercell has 13 alternating potential wires with 12 sense wires placed at their midpoints. Four shaper wires electrostatically close the cell. Supercells are bounded by two gold coated mylar cathode planes parallel to the sense wire plane. Cathode sheets are kept at ground. Sense wires are kept at 3 kV and potential wires are kept at 2 kV with small variations to keep a uniform drift field. The entire supercell is mounted at 35 degrees with respect to the radial direction to compensate for the Lorentz drift of charged particles in a magnetic field. The Lorentz drift is the deflection of the charged particle due to the presence of the magnetic field generated by the solenoid. In order to maintain a roughly constant drift velocity the number of supercells in each superlayer varies from 168 cells in Super Layer 1 (SL1) to 480 cells in Super Layer 8 (SL8).

Wire readout is accomplished with custom built ASD (Amplifier, shaper, discriminator) radiation hard 8 channel chips. ASD boards are mounted directly on the COT end plates. Pattern recognition allows the recognition of multiple hits on a single sense wire.

A particle of charge q moving in a field $\vec{B}$, inside the CDF tracker, has a helical trajectory with a radius of curvature of

$$r = \left| \frac{p_T}{qB} \right| . \tag{4.7}$$

The transverse momentum p_T is obtained by reconstructing the particle trajectory from hits in the COT and extracting the curvature r. The system provides excellent momentum resolution [45]. In a recent study of the momentum resolution using J/Psi [46] a momentum resolution of $\delta p/p = 1.5 \times 10^{-3}$ was found.

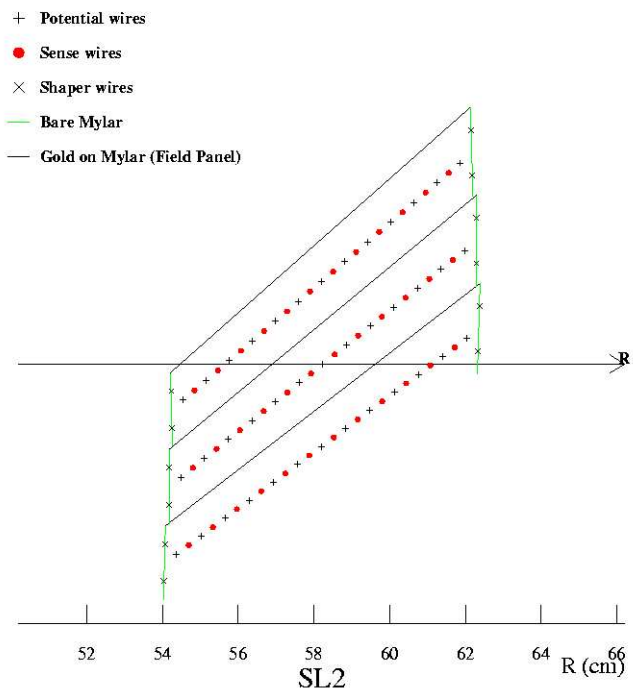

Figure 4.22: Layout of a single COT supercell showing the arrangement of potential and sense wires. Cathode sheets and field shaper wires are also shown.

4.2.2 Calorimetry

Particles with a transverse momentum greater than 350 MeV/c escape the tracking volume, and are detected by the calorimeters outside the solenoid. The Central calorimeter provides coverage to $|\eta| \leq 1.1$ and plug calorimeters in the range $1.1 < |\eta| < 3.4$. In each region, "Plug West," "Central" and "Plug East" calorimeters are provided for measuring Electromagnetic and Hadronic showers.

The operating principle of a calorimeter is to provide an instrument in which the energy from particles produced in collisions can deposited and measured. Each calorimeter is composed of alternating layers of absorber material (high Z material such as lead or steel) and an active read out material. As high energy charged particles traverse an absorber they interact with the material causing

ionization's and creating showers of secondary particles. An active material, in this case polystyrene mixed with organic scintillator, interacts with the shower producing scintillation photons. Wavelength shifters are provided as light guides to collect photons and lead then out to PMTs mounted on the outer radii of the wedges. The amount of light measured is proportional to the shower energy.

Spatial resolution in the $\eta-\phi$ plane is provided by segmenting the calorimeters into towers projected back to the nominal interaction point. In the central region individual towers cover 15 degrees in ϕ and 0.11 in $|\eta|$. Each azimuthal 15 degree section is referred to as a *wedge*. Plug Calorimeter ϕ coverage is 30 degrees between $1.1 < |\eta| < 2.11$, but returns to a 15 degree segmentation in the $2.11 < |\eta| < 3.4$ region. Radially the Electromagnetic Calorimeter (ECAL) is closer to the solenoid, followed by the Hadronic Calorimeter (HCAL). Segmentation of the HCAL sections and the ECAL sections are matched allowing a summation of the total energy deposited in an $\eta - \phi$ region.

Separate Electromagnetic and Hadronic Calorimeters are employed at CDF. Small mass e^+, e^- and γ develop electromagnetic showers at a relatively shallow depth. To take advantage of this electromagnetic calorimeters are designed with a more frequent alternation (thinner layers) of absorber and scintillator with which to sample the shower profile. Hadronic particles with their larger masses punch through the relatively shallow electromagnetic calorimeters and deposit their energy in the larger Hadronic Calorimeters. Absorber and scintillator layers in the hadronic calorimeters are thicker to account for the greater penetrating power of hadronic radiation. The strong interactions by which hadronic particles primarily deposit their energy may involve the production of muons μ and neutrinos ν which themselves escape the calorimeter and lower the energy resolution, Equation 4.8 of the hadronic calorimeters.

Detector	Sampling and PMT	Response Term
CEM	13.5%	2%
CHA	50.0%	3%
PEM	14.4%	7%
PHA	80.0%	5%

Table 4.2: Calorimeter resolution parameters for selected calorimeters.

The absorber used in the Central Electromagnetic Calorimeter (CEM) is lead while the Central Hadron Calorimeter (CHA) and Plug Hadron Calorimeter (PHA) use steel. The Plug Electromagnetic Calorimeter (PEM) uses a Ca-Sn-Pb alloy between steel plates as an absorber. Hadronic coverage is extended in η to cover the gap between the CHA and the PHA through the use of the Wall Hadron Calorimeter (WHA). The WHA is similar in construction to the CHA except that it uses 5.1 cm thick absorber. The WHA energy resolution is effected primarily by the η position of the instrument, where it receives a factor of $\sim \sqrt{2}$ higher jet energies.

The design energy resolution of the Calorimeters is given by

$$\frac{\sigma_E}{E} = \frac{A}{\sqrt{E_T}} \oplus B, \tag{4.8}$$

where the $\oplus$ means that the terms are added in quadrature. the first term comes from sampling fluctuations and PMT performance. The response term is a constant and comes from the non-uniform response of the calorimeter. The values of these parameters are listed in Table 4.2. The actual energy resolution at 50 GeV for the CEM, CHA and WHA are given as 2%, 11% and 14% [47].

The functional dimension describing the evolution of electromagnetic showers is the *radiation length* X_0. The CEM and PEM thickness corresponds to 18 and

Detector	absorber	scintillator
CEM	3 mm Pb	5 mm
CHA	2.5 cm Fe	10 mm
PEM	4.5 mm Ca-Sn-Pb	4 mm
PHA	5 cm Fe	6 mm
WHA	5.1 cm Fe	10 mm

Table 4.3: Calorimeter materials. The initial scintillator layer of the PEM is 10 mm thick and used in the place of the pre-shower detector present in the central region.

21 X_0 respectively. The *attenuation length* λ_I is more descriptive of the energy deposition process taking place in hadronic calorimeters. Where λ_I is defined as the depth of absorber material transversed by a hadronic particle which will reduce its energy by a factor of $1/e$. The CHA, WHA and PHA are respectively 4.7, 4.5 and 7 λ_I thick. Calorimeter materials and the thicknesses of individual layers are given in Table 4.3.

Identifying the transverse character of the showers is aided by two counters embedded within the calorimeter region. The Central Preradiator Detector (CPR) is mounted between the solenoid and the CEM. It consists of proportional counters and samples the early development of electromagnetic showers in the material of the solenoid coil. The Central Electromagnetic Shower Counter (CES) is a proportional strip and wire chamber embedded with in the CEM at 5.9 X_o where the average EM shower maximum occurs. The CES provides a measurement of the electromagnetic shower profile in both the $r-\theta$ and the $r-z$ planes. The CES has cathode strips arranged azimuthally giving z coordinate information. Wires running parallel to the beam line give $r-\phi$ information.

In the plug the preshower detector consists of a thicker initial scintillator

layer (10 mm). This layer is readout separately from the remaining scintillator layers. The Plug Shower Maximum (PES) detector is embedded at roughly 6 X_0, radiation lengths and is constructed of 2 layers of scintillator with 45° segments in ϕ and into 2 η regions. The two 5mm layers of scintillator are arranged with a $\pm$ 22.5^o offset with respect to the radial direction.

4.2.3 Muon Systems

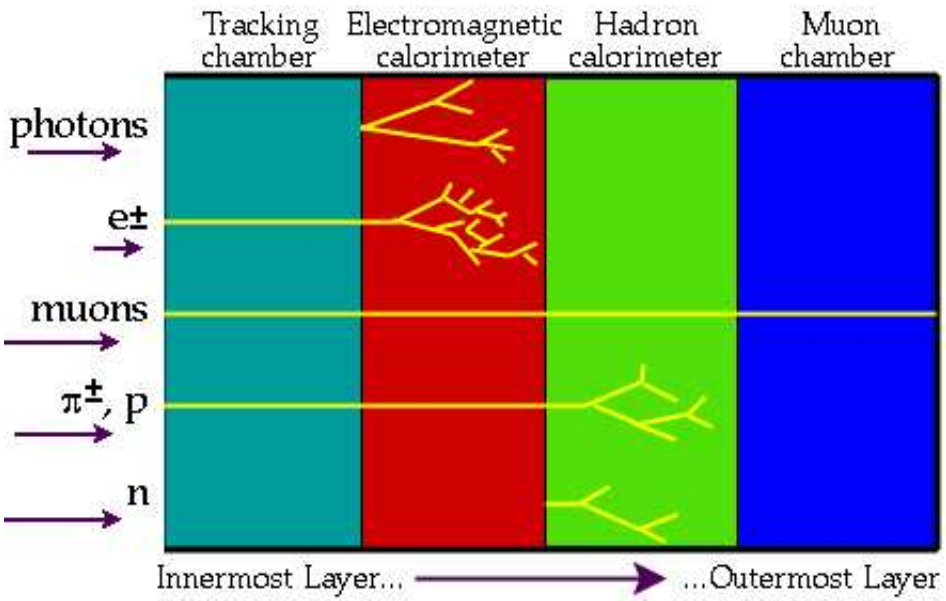

Figure 4.23: With nearly all of the other particle species absorbed in the inner portions of the detector the remaining particle flux is primarily composed of muons.

Muon detection is accomplished by placing charged particle detectors behind enough absorber material to ensure that most arriving particles are indeed muons. While muons leave tacks in the ionizable gas of the COT they deposit little or no energy in the calorimeters. As discussed in the ECAL section the energy loss in matter of a charged particle is inversely proportional to the mass of the particle. In the same manner that higher mass hadrons, muon with a mass roughly 200

times that of the electron, muons leave nearly no signal in the ECAL. Nor are muons subject to the strong interactions and do not interact with the HCAL. Figure 4.23 shows the portions of the detector in which the various long lived particle species deposit their energy.

Muons are identified at CDF by matching the tracks with hits or *stubs* in the muon chambers. Drift tubes with ionizable gas, combined with scintillator layers to provide timing information comprise the various muon detector systems. The CDF muon system is comprised of the Central Muon Chambers (CMU), Central Muon Upgrade (CMP), Central Muon Extension (CMX), and Intermediate Muon Detector (IMU).

The CMU and CMP provide coverage in the $|\eta| < 0.6$ range. Typically the two detector are used together by requiring a coincidence between the two detectors. The CMU contains 3 towers of four rectangular drift cell per calorimeter wedge. At the center of each drift cell is a sense wire running the length of the cell. Pairs of sense wires are offset by 2° to provide a ϕ indication by determining which sense wire was hit first. The z-position of the track is determined by comparing the pulse heights at each end of the wire. The CMU resolution is 250 μm in $r-\phi$ and 1.2 mm in $r-z$ A minimum 3 out of 4 coincidence defines a *muon stub*.

The CMP resides behind the CMU and an additional 60 cm of structural steel which support the CDF detector. Similar in construction to the CMU the CMP contains only a single sense wire. The additional absorber further reduces the non-muon flux.

The CMX provides coverage in the $0.6 < |\eta| < 1.0$ range. Four conical arches, 2 on either side of the detector comprise the The IMU provides coverage in the forward region ($|\eta| \simeq 2.0$). The Muon detector system covers a large solid angle but is not complete. A map of the $\phi - \eta$ coverage is provided as Figure 4.24.

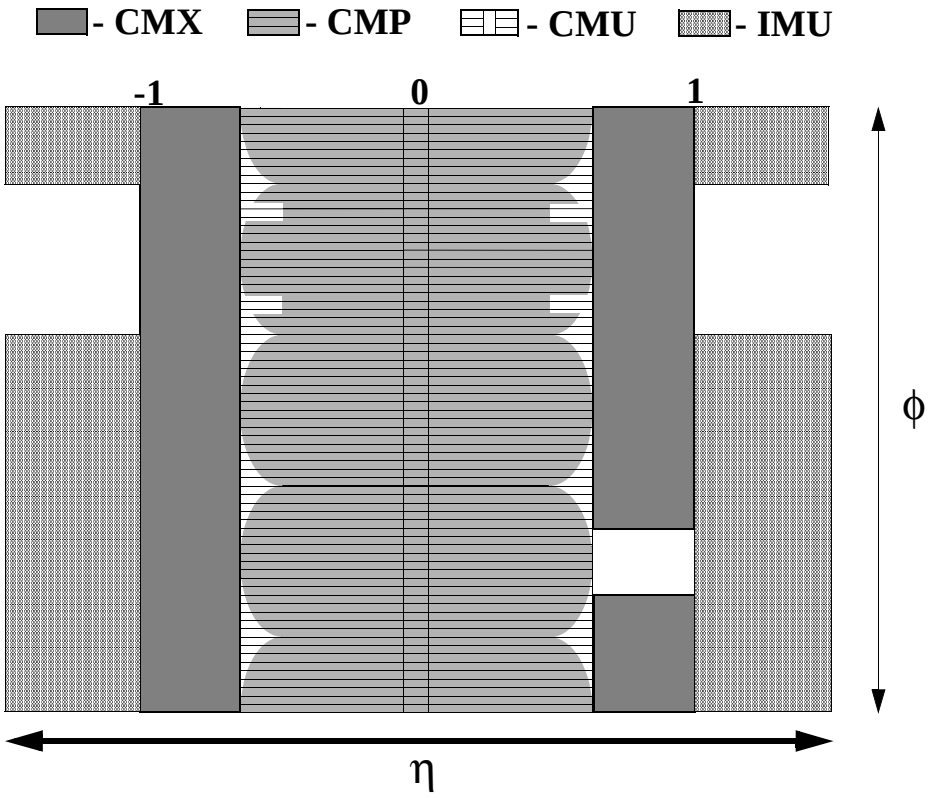

Figure 4.24: The CMU and CMUP detectors are use in conjunction, CMUP muons requiring a stub in both instruments. The CMX detector extends muon detector coverage out to $|\eta| < 1$.

4.2.4 Luminosity Counters

Inelastic proton antiproton interactions, called *minimum bias events* scatter at small angle from from the beam pipe. These are primary particles and measuring the flux of these minbias particles can give a precise knowledge of beam luminosity (see Equation 4.2). Cherenkov Luminosity Counters are placed at small angle $\theta \leq 3$ degrees relative to the beam axis have a high probability of intercepting these particles.

Cherenkov Luminosity Counters consist of 48 gas filled volumes placed on either side of the detector. Arranged in 3 concentric rings of 16 truncated cones with the small end closest to the interaction region they cover the range $3.7 < |\eta| < 4.7$ The active gas in the counters is iso-butane with an index of refraction of $n = 1.00143$ and good transparency in the UV range [48, 49]. Reflectors are placed at the large end of each cone and PMTs closest to the interaction region.

Cherenkov light from incident particles is emitted at an angle θ_C determined by the index of refraction of the gas and the dimensionless particle velocity $\beta = v/c$

$$\theta_C = \cos^{-1}\left(\frac{1}{n\beta}\right). \tag{4.9}$$

The number of photoelectrons produced by a charged particle $N_{p.e.}$ in a Cherenkov Counter is proportional to the path length L to $sin^2\theta_C$

$$N_{p.e.} = N_o L sin^2\theta_C \tag{4.10}$$

Where $N_o \sim 200cm^{-1}$ is a design parameter specific to the counter [38].

The prompt particles from $p\bar{p}$ interactions travel the full length of the counter

and generate a large amplitude PMT signal, $\sim$ 100 photoelectrons. Beam-halo interactions or sources of charged particles originating is secondary interactions with the detector structure have lower momenta, transverse the counter at larger angles and have shorter path lengths. Photoelectrons produced by these sources experience large losses due to reflection.

The high precision of the luminosity monitoring is ensured by the fact that the counters measure the actual number of primary particles. The counters are robust at high luminosity since two particles incident on the same detector result in a signal twice the size of a single particle signal.

4.3 Data Acquisition

The discovery of the top quark by CDF and her sister experiment D0 required the detection of a signal with a cross section 9 orders of magnitude smaller than the total inelastic $p\bar{p}$ cross section. Top quark events are literally "one-in-a-billion" events. Figure 4.25 shows the relative magnitude of inelastic $p\bar{p}$ events to the production cross section for pair produced $t\bar{t}$. For a 3rd generation vector leptoquark above 300 GeV, the production cross section is an order of magnitude smaller than even $\sigma_{t\bar{t}}$. To preserve the detector information for every collision is clearly impractical, while providing full reconstruction of events to to determine which are worth preserving is impossible given a beam crossing rate of $\sim$ 2.5 MHz.

CDF designers solved this problem with a multi-level trigger system. There are three trigger levels of increasingly sophisticated reconstruction. At each level, triggers comparison event information with a list of thresholds to determines whether or not an event will be accepted and passed on to the next level.

The design limit for fully reconstructed events to be written to tape for permanent storage is 75 Hz. The triggering system is designed to reduce the large event rate in several stages with event buffers at each level deep enough to minimize the deadtime.

4.3.1 Level-1 Trigger System

At Level-1 the triggering system consists of several individual instrument triggers each with its own selection criteria. In level 1 the information from all detectors is buffered in a 42 event deep synchronous data pipeline and stored for 5.5 μs. Without event buffering Level-1 decision time or latency could either be no greater than the time between bunch crossings or some fraction of bunch crossing would never be examined by the CDF detector at all. In operation a Level-1 trigger deadtime of $> 5\%$ is required.

During the Level-1 latency the event data is analyzed by three parallel synchronous streams. One stream finds calorimeter based objects (electrons, photons and jets). A second find stubs in the muon chambers. Last, the eXtremely Fast Tracker (XFT) reconstructs tracks on the transverse plane of the COT, and an extrapolation unit (XTRP) matches tracks to calorimeter towers and muon chambers.

At Level-1 Calorimeter towers are paired to form trigger towers. A simple threshold model is applied to the trigger towers, EM energy and Had + EM energy to form trigger primitives for clusters. These are examples of object triggers, triggers using information from only a limited portion of the detector. Global triggers, for instance the sum of all calorimeter energies, are also available. Electrons and muons objects are identified when the XTRP links reconstructed

XFT tracks with clusters in the EM calorimeter and muon stubs. P_T and E_T thresholds are programmable for various regions

The Level-1 trigger decision module using simple AND and OR gates can form up the 64 different triggers by setting requirements on the number and certain features of the objects from the level 1 trigger streams. Trigger rates can be prescaled to prevent any single trigger from overwhelming the available DAQ system bandwidth. The rejection factor is about 150 thus decreasing the event rate to around 15 kHz.

4.3.2 Level-2 Trigger System

Events passed on to Level-2 by the Level-1 trigger decision module are loaded into one of four asynchronous event buffers. While level 2 is processing an event the buffer that event occupies can not be over written by Level-1. When all four buffers are full the system begins to experience *deadtime*.

Level-2 is allowed a 20 μs decision time or *latency* to perform a limited level of event reconstruction. The latency of Level-2 is assigned with the goal of keeping the deadtime to 10%.

The first phase of Level-2 is an event building stage taking approximately 10 μs. Calorimeter towers are combined to form clusters of deposited energy. These are jet primitives possessing both E_T as well as average η and ϕ. Shower maximum detectors (XCES) reduce the rate of electron and photon fakes by eliminating the background from single phototube discharge and improving matching between XFT tracks and EM clusters.

In the second phase of Level-2 object data is examined to see if any of the Level-2 triggers have been satisfied. About 100 different Level-2 triggers can be

formed. The Level-2 accept rate is about 300 Hz with a rejection factor of about 150.

4.3.3 Level-3 Trigger System

Level-3 is fully implemented as software running on a processor or event builder farm. The triggering architecture is shown in Figure 4.26

4.3.4 Data Acquisition

After a Level-2 accept has been sent event fragments are collected in the Data Acquisition System (DAQ) buffers and then transfered to the event builder farm. The data from one event is assigned to a single node in the event builder farm where the event will be fully reconstructed. Triggering also takes place in Level-3. Events accepted by Level-3 are delivered to the consumer-server logger system (CSL) which will then transfer the data to mass storage. The event rate transfered to tape is around 75 Hz. With event sizes of $\sim$ 250 kB this corresponds to $\sim$ 20 MB/s of bandwidth.

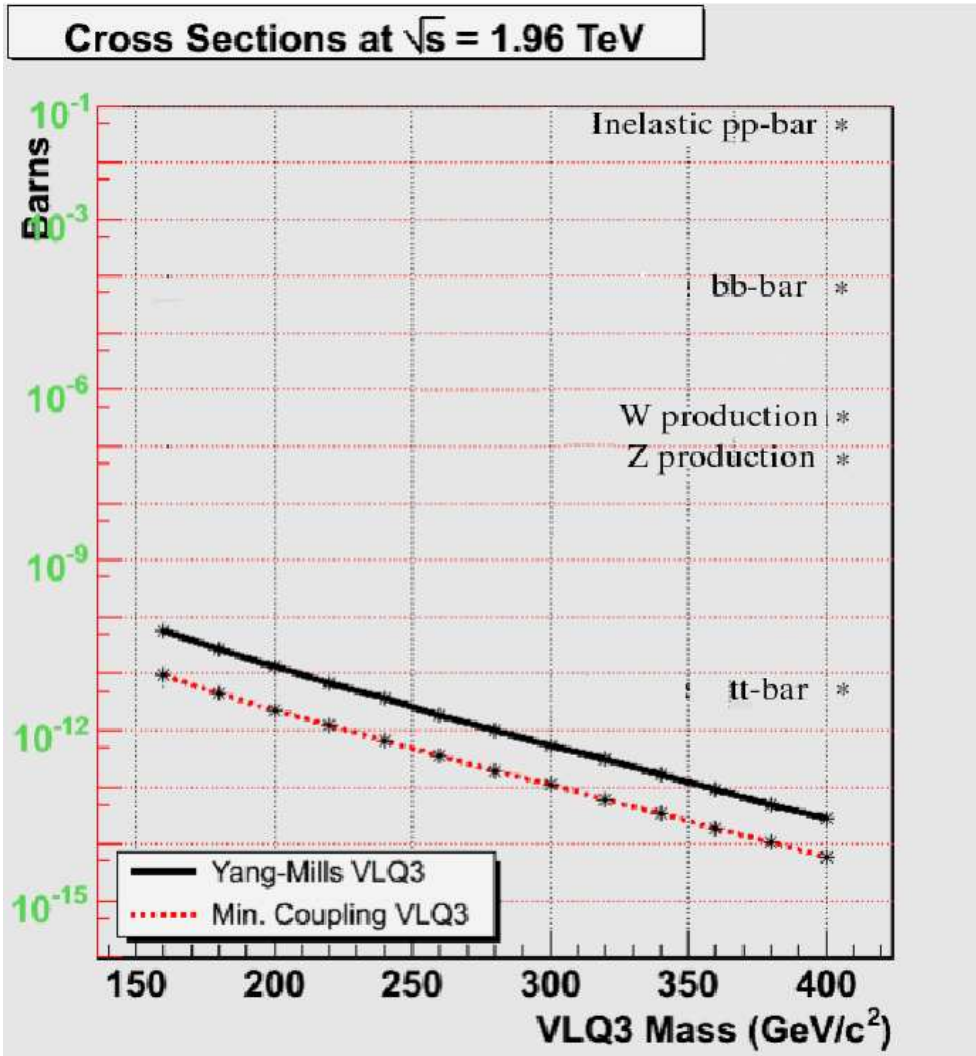

Figure 4.25: A semilog plot comparing the cross sections of inelastic $p\bar{p}$ events (in green) to the theoretical production cross section of 3rd generation vector leptoquarks. The blue and red curves are the production cross sections for the Yang-Mills and minimal coupling models of vector leptoquark production respectively. Various other physics backgrounds are included as well to show the orders of magnitude ratio between those processes and vector leptoquark production.

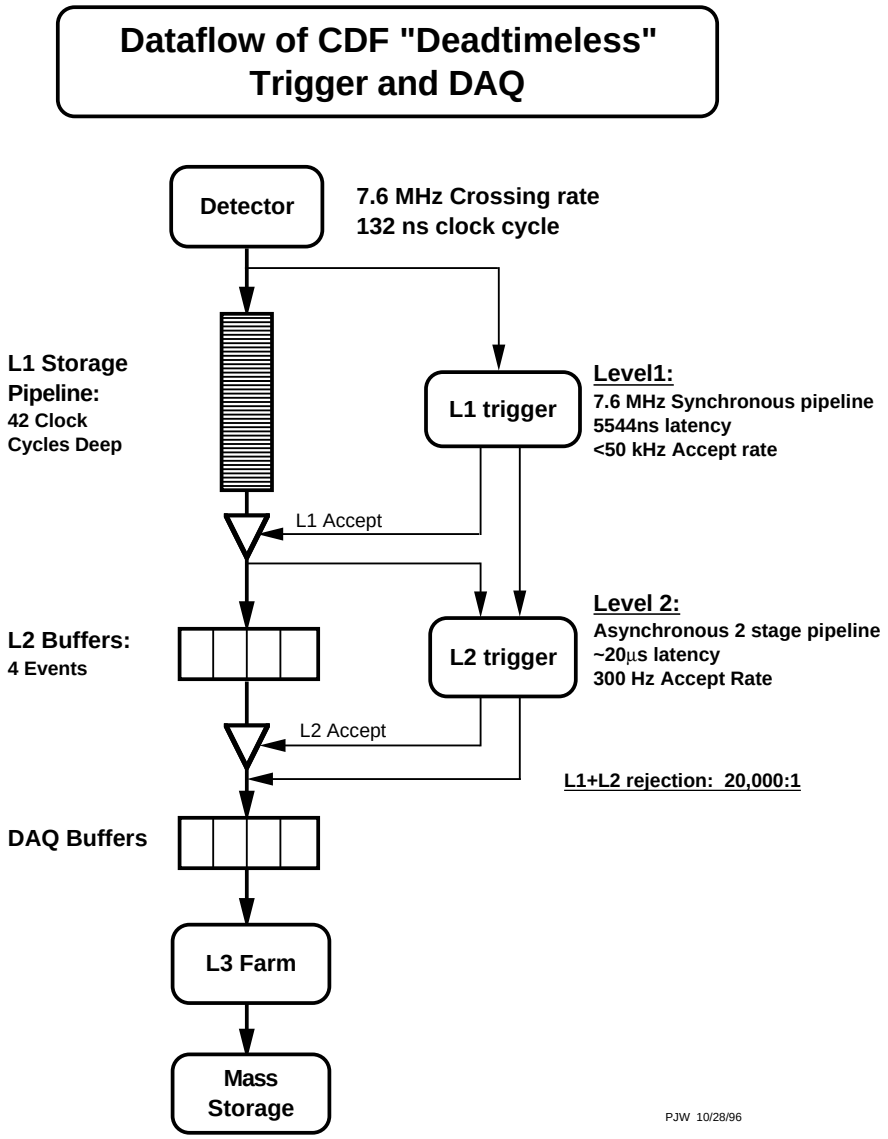

Figure 4.26: Level 1 and Level 2 are dedicated hardware processors. Level 3 consists of a farm of processors

Chapter 5

Silicon Operations

The topics covered in this chapter are presented in conjunction with the personnel organization of the Silicon Group as a whole and the specific tasks of the smaller working groups. We describe the place of the Silicon Group within the CDF collaboration and of the smaller working groups established within the silicon effort to accomplish specific and on-going tasks. Special task forces are also formed to deal with specific issues. The wire-bond failure task force and the longevity committee are two specific examples of such groups.

This chapter covers the maintenance and operational measures required to ensure high quality data from the various silicon detector components. While the silicon detector is not utilized in this analysis, a description of the effort required to keep this particular instrument running and taking good data is an effective way to illustrate the efforts by the hundreds of physicists required to keep the CDF experiment up and running.

The SVXII detector was installed in 2001 with a commissioning phase lasting 1.5 years. This was due in large part to the complexity of the system [50]. There were several unexpected milestones in the commissioning, including the

clearing of several ISL cooling channels with a laser. Epoxy blocked several of the ISL cooling channels, rendering 15 ISL ladders inoperable. All but one of these ladders were recovered when the blockages were cleared with a laser. Two additional design changes were implemented on the Fiber Interface Boards requiring the replacement of several on board component which resulted in a number of ladders transitioning to taking good data.

Figure 5.1 illustrates the current operational reliability of the silicon detector. We are currently operating with 92.5% of all ladders powered and are recieving good data from 85%. Good data is defined as less than a 1% error rate from the ladder.

5.1 Silicon Organization

Organizationally, the Silicon Detector is a sub-project of the CDF experiment lead by two Sub-Project Leaders or SPLs. Administratively, the SPLs answer to the two spokespersons, the elected leaders of the CDF collaboration while operationally the SPLs report to the CDF head of operations. As is typical of CDF, many of the leadership positions are occupied by two persons who collaborate in accomplishing the tasks of the group.

The various working groups and a short description of each are listed below. While the definition of a working group is somewhat fluid, each of the groups on the list has an established personnel roster and maintains a schedule of experts on 24-hour availability. The workload of the Silicon Detector Group is estimated to be 15 to 20 FTE or Full Time Equivalents [50]. In practice, roughly 80 persons provide the required man-hours on an “as available” basis. Operational needs sometimes bring in All Hands to address a particular issue. It is estimated that

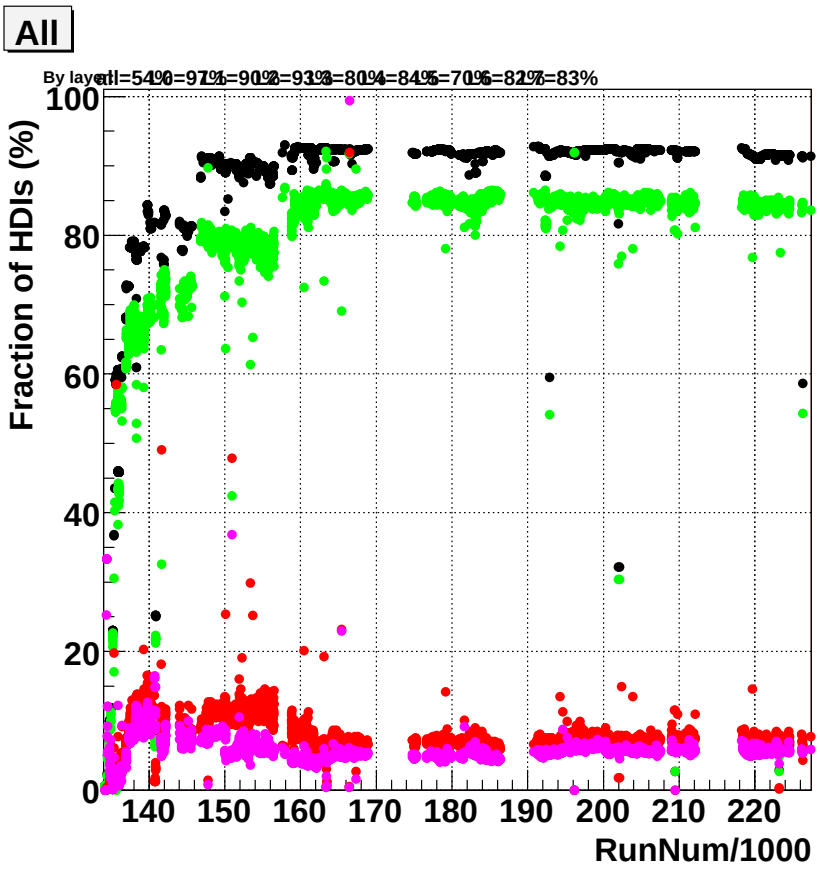

Figure 5.1: The experiment is currently in a stable running configuration of the silicon detector with 92.5% of ladders powered (black) and getting good getting good data (green) from 86% of the ladders. Bad ladders, ladders with an error rate $< 1\%$ are shown in red. The overall error rate is shown in pink. The commissioning phase of silicon operations ended around Run 145,000.

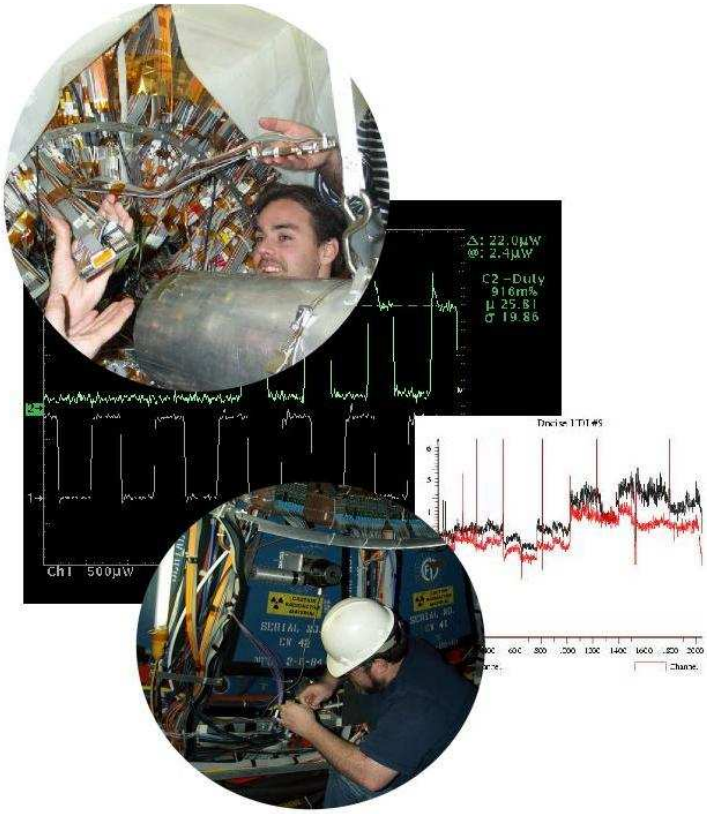

Figure 5.2: Silicon Detector Working Group Logo showing (from the top) David Clark at the east face of the bore during a rerouting of silicon cooling lines, oscilloscope screen shot used during light level measurements, channel occupancy showing an increase in occupancy at the transition to chips on the z side of the ladder, Stanley Forrester inserting a ribbon cable tap on a Port Card command cable.

1/3 of the work hours go into steady state maintenance, while the remaining 2/3 go into incident response. The SPLs have also identified a need for R&D personnel to deal with issues that will appear with increased luminosity.

The working groups of the Silicon Detector effort are:

- **Detector Maintenance:** Responsible for quiet time studies and maintenance requiring collision hall access. Quiet time studies are those maintenance operations, usually at the single ladder or even single chip level, which must be performed with no beam in the Tevatron.

- **Calibrations:** This group consists of one person and an alternate who updates the Silicon calibrations often enough to supply offline processing with the required Silicon performance data. Actual calibrations are preformed by shift crews once per shift when allowed by operating conditions, e.g., quite time.

- **Power Supplies and Interlocks:** This group is responsible for the CAEN SYS527 power supplies which service each wedge. Efforts of this groups are focused on swaps of power supply modules, calibrations and the occasional bias voltage change. The latter requires the removal of a CAEN module and soldering in a new voltage divider. Accesses to replace L00 crowbars are made in conjunction with the Maintenance group.

- **DAQ:** Responsible for the VME hardware and software maintenance, as well as mitigation of errors which prevent real time data taking. The Ghost Buster resonance frequency protection board was introduced by this group.

- **Monitoring:** Examines data from each silicon channel for indications of problems. Some problem they might encounter are high occupancy in a

single channel or dropped readout from all chips on the z side of a ladder. Problems detected by this group are passed on to the DAQ or maintenance groups.

5.2 Silicon Maintenance Group

When quiet time studies and changing parameter settings are not sufficient to correct single ladder faults, a collision hall access may be necessary to isolate the problem. The usual first step is an optical fiber swap. Readout of data from a single ladder, between Port Card and the Fiber Interface Board, is accomplished through optical fiber, see Figure 4.15. A ladder which shows a bit problem can have its optical fiber switched to a different readout channel. A swap will usually indicate if the problem is inside the detector and therefore likely unfixable, or exterior to the CDF detector requiring only a component swap. If the problem follows the cable, we conclude that the problem is in some inaccessible portion of the detector, and is therefore only addressable via chip initialization settings. If, however the problem stays with the channel despite having input from a different ladder we can conclude that an accessible component is responsible.

The optical receivers are located on the Fiber Interface Boards, FIB (see Figure 4.15, first component on the left, second row). The data readout from each ladder is converted to a light signal for transmission by a component on the Port Card, called a DOIM Transmitter, TX. The light signal is carried out of the detector volume on fiber optic cable. The optical receivers, DOIM RXs, convert the light signal back to an electrical voltage. RX performance is variable enough that for a channel with bit problems, it is often worth the effort to try several different RXs to find one well-matched to the TX on the Port Card.

The next level of maintenance is to swap out an entire FIB card, servicing two entire wedges. Each FIB is connected with a VRB through the backplane of each crate. The VRB front end handles communications with the portions of the CDF Data Acquisition System which lie outside of the collision hall. If a VRB swap does not fix the symptom, then the fault lies out side the collision hall and the problem is reassigned to the DAQ group.

Rarely, a problem can be traced to a Port Card. Most of these problems are unfixable because of equipment access issues. There is, however, one problem that can be fixed for a limited number of Port Cards. The Port Card comes in two halves that can become unseated due to thermal expansion and contraction. If the Port Card is near enough to the bore face, a thin probe can be inserted into the detector to reseat the card.

The Silicon Working Group Logo illustrating several of these maintenance activities is shown in Figure 5.2.

5.3 Power Supplies and Interlocks

Past problems with the power supplies have included spontaneous transitions, and loss of communications. A spontaneous transition happens when a transient signal occurs within a module, faking a command which tells the module to transition to off. The problem is mitigated by simply leaving that circuit unpowered until required. A shift crew member will physically plug in the system before issuing a manual reset. Loss of communication is an occasional problem in which the module begins sending it status, voltages, and read back to somewhere other than where the CDF monitoring software is configured to look for it.

Mitigation is accomplished through "Hockerization" a procedure named after

the its creator. This procedure is a hard reset of the entire crate containing the offending module. During this process, the CAEN software seeks to reestablish communication with the CDF monitoring software. The problem is believed to track with increased luminosity and is expected to become a major issue in the near future.

The proton beam enters the collision hall from the West side an has an intensity 5-10 times higher than the antiproton beam. This leads to an asymmetry in the power supply crate malfunctions. To mitigate this problem one set of CAEN crates has actually been moved out of the plane of the Tevatron beam.

5.4 Monitoring

The monitoring group looks at chip and ladder performance to diagnose faults in the instrument. If a fault is detected, such as high occupancy in all of the channels assigned to one chip or the total loss of data from the $z-$side chips, the maintenance group will be notified. Also, when either the maintenance or the power supplies group does any maintenance on any component the data channel associated with that component item is placed on a two week watch list. During this time data quality in the effected channels, is monitored with the monitoring group having final sign-off on whether or not a problem has been fixed.

5.5 Wire Bond Failure

Wire Bond Failure The Silicon ladders are connected $r - \phi$ and $r - z$ sides with wire bonds perpendicular to the magnetic field. At high level L2 Accept rates, Lorentz forces from the control signal take on the form of an oscillating

current and can set up a resonance in the wire bond. Readout commands near the natural frequency of the wire bond can rip the wire from its bond pad, see Figure 5.3. A distribution of the natural frequencies of the wire bonds have been found in the 15 kHz range which is a frequency range the L1 Accept frequently occupies.

Hardware protection has been implemented in the form of the Ghost Buster board [51]. Ghost Buster reads the time between subsequent readouts and bins the result. If synchronized readout commands are detected, e.g.,the occupancy in any one bin rises above 10, a BRAKE signal is sent to the Silicon Readout Controller (SRC) and data taking is stopped.

5.6 Radiation and Longevity

SVXII was designed to survive an integrated luminosity of 2 to 3 fb^{-1}. As of January 2006, the integrated luminosity to which the silicon detector has been exposed stands at 1.4 fb^{-1}. A new silicon detector, for RunIIb, intended as a replacement for L00, SVXII and ISL, was canceled [52]. So the current detector will have to serve until 2009 and into an expected integrated luminosity of between 4 and 8 fb^{-1}. As a consequence the longevity of the silicon detector has become a major focus of the Silicon group's efforts.

Operational constraints on the Silicon detector operations have been implemented to ensure the safest feasible operation. The main focus, however, has been on mitigating the effects of radiation damage to the bulk silicon which makes up the sensor elements in the ladders.

Radiation damage occurs when incident particles "knock" atoms loose in the crystal of the bulk silicon. This leaves points which attract and reduce the free

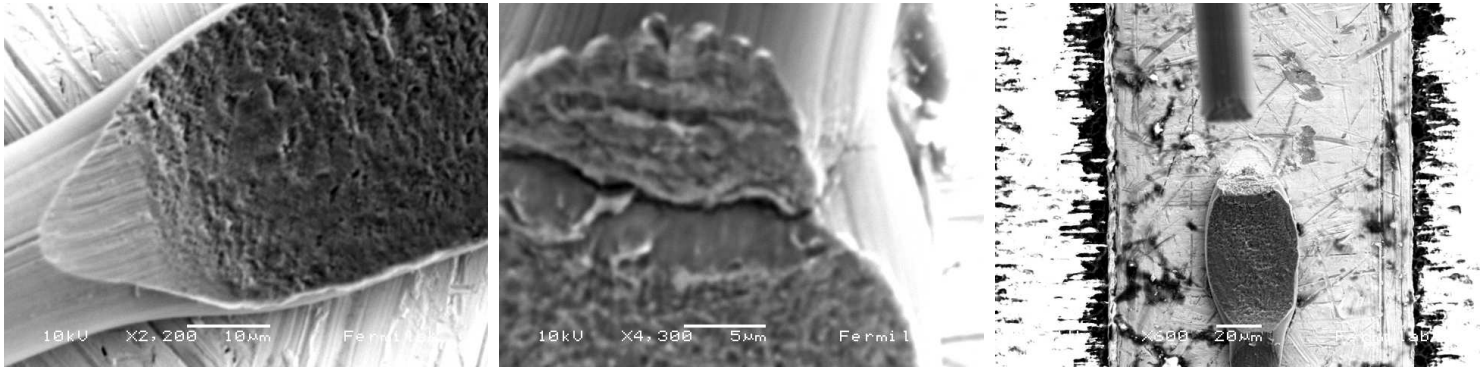

Figure 5.3: The first photograph is of a micro wire-bond in good repair. The second wire-bond has been deeply stressed but has not yet separated from the footing. The third shows a complete separation of the wire from the footing.

movement of charges through the bulk material. Single defects do reduce charge mobility within the lattice but the larger effect comes when thermal effects cause these defects to migrate and collect. The cumulative effect of these defects is called type inversion as the bulk n-type material is turned into a p-type material [53]. The result of this is that a greater bias voltage must be applied to fully deplete the silicon detector. An operational limit of 100 V bias is imposed by the capacitively coupled design of the readout traces. Beyond 100 V the oxide layer that insulates the capacitive pickup experience pinhole leaks characterized by large leakage currents through the sensor. The concern is that given enough radiation damage it may become impossible to deplete the silicon sensors. The required depletion voltages are projected for two scenarios in Figure 5.4. An optimistic -1σ model predicts that deletion of the sensors out to 8 fb^{-1} will be possible. The solid line show the actual depletion voltages to date. This indicates that radiation mitigation measures taken have been even more effective than the optimistic model predicted.

One source of radiation exposure to the silicon detector comes from normal operations. This is a consequence of being located at the smallest radius with respect to the beam line of any of the detector subsystems. These operational doses of radiation are, however, greatest at beam startup. From operational experience, high beam losses indicate a higher probability of uncontrolled beam loss. Thus, operational limits on beam losses have been set for shift crews before they can bias the silicon sensors.

A second and more worrisome source of radiation exposure is the kicker pre-fire. The Tevatron beam has three trains of particle bunches in each beam with an abort gap separating the trains. The purpose of these abort gaps is to allow a sufficient interval for the beam dump steering magnets, the kickers magnets to

ramp up their field and to divert the beam safely. If the kicker prefire occurs in some place other than the abort gap the Tevatron beam is diverted through the running detector. There have been 18 incidents in which the kicker magnets spontaneously ramped up sending the Tevatron beams through the detector. Several of these incidents have lead to the unrecoverable loss of ladders.

In order to minimize the thermal effects and to increase the lifetime of the silicon detector, the SVXII volume has been thermally isolated and cooling temperature has been reduced from -6 degrees to -10 degrees[1]. CDF operations has also, at the urging of the Silicon group, tried to minimized the number of thermal cycles or major changes in the detector temperature to help mitigate radiation damage.

Radiation monitoring is accomplished through the use of Thermo Luminescent Dosimeters (TLDs) and Beam Loss Monitors (BLMs). The two types of TLDs are physically mounted on and within the CDF detector in 144 locations. These TLDs must be harvested in order to be read out. The four BLMs are sealed glass argon chambers. They are located in the horizontal plane of the Tevatron beam at $\pm$ 4.3 meters from the interaction region and on either of the beam. Figure 5.5 illustrates the integrated radiation dose received by components in the tracking volume including the various Silicon detector components.

Silicon Cooling: The cooling system removes the heat load from the Silicon Port Cards, sensor leakage currents and power consumed by the SVX3D chips. Two coolant loops are provided one for ISL and the SVXII Port Cards and one

[1]Incidentally the SVX Port Card DOIMs did not respond well to the change in temperature. There were significant increases in bit error rates in 12 ladders in excess of the 1% error rate definition of a "good ladder." After a study of leakage currents as a function of coolant temperature indicated that the Port Cards were in fact thermally isolated from the SVXII ladders, the Port Cards were placed on the ISL cooling loop which remains at -6 degrees. The 12 errant ladders recovered within a month of operations of the change.

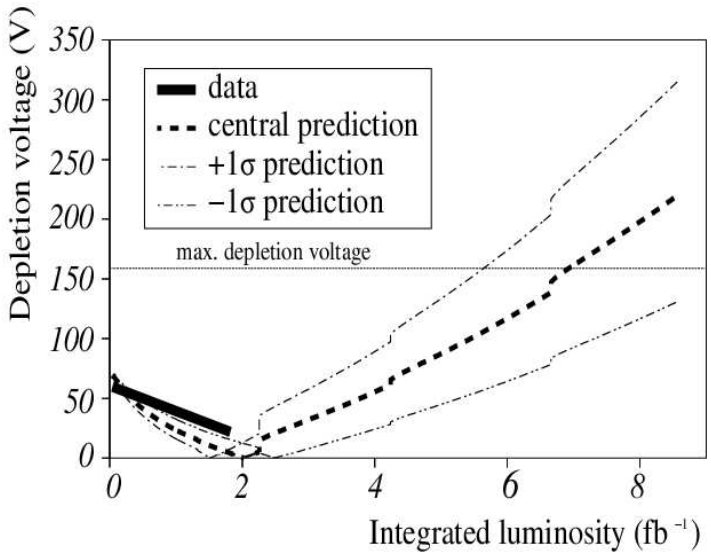

Figure 5.4: Projected bias voltages required to deplete Layer 0 or the inner most layer of SVXII. Three projections are presented. The central projection and an optimistic (-1σ) and a pessimistic (+1 σ) projection. The data in solid black available out to 1.7 fb^{-1} seems to be following the -1 σ curve. The indication is that we will be able to deplete the inner most layer of SVXII until well beyond 8 fb^{-1}.

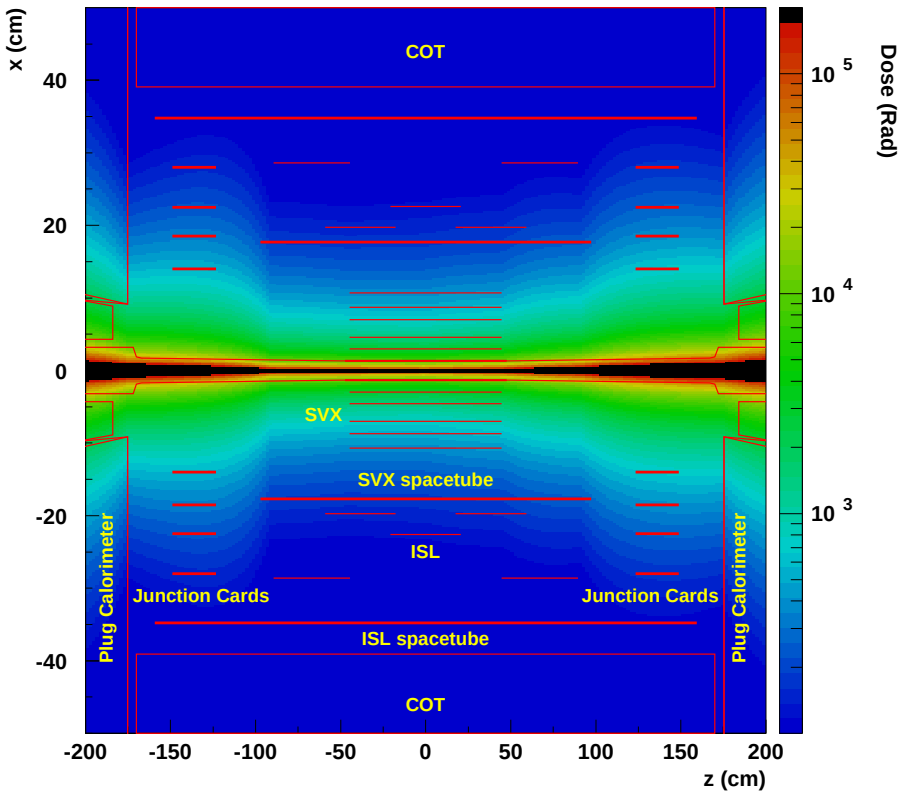

Figure 5.5: Integrated radiation dose over the original expected lifetime of the Silicon detector delivered to all components in the tracking volume. Due to the placement of the silicon detector at small radius that instrument receives a high radiation dose.

for the SVXII and Layer 00 ladders. The coolant is water ethylene glycol at 6 C for ISL and -10 C for SVXII and L00. Initially the SVXII cooling loop was taken from 6 C to -6 C as a radiation mitigation measure. Upon a rise in error rates from the SVXII ladders the SVXII Port Cards were placed on the ISL cooling loop. The SVXII cooling loop has since been reduced to -10 C.

Chapter 6

Trigger and Dataset

The theoretical models for a number of Standard Model investigations and beyond the Standard Model physics searches include signatures with two taus. In many cases they include signatures with low momentum decay products from the short lived taus. Some of these processes include Drell-Yan, SUSY, Higgs, b and top physics. At the high luminosity CDF Run II environment dedicated triggers are required to collect these low momentum events at a rate that will not overwhelm the data handling system.

The *Lepton + Track* triggers [54], requiring the coincidence of two separate charged lepton candidates, brings the trigger rate down and allows the collection of events with low E_T and p_T leptons. Taus produced in these events decay almost immediately. The leptonic decay channels to electron and muon take place with a total branching ratio of 0.35. The CDF detector has high efficiency for identifying electrons and muons, although the leptonic decay products are at lower p_T due to production of neutrinos in the decay. However, the coincidence of two taus decaying to leptons $\tau_{lep}\tau_{lep}$ is only $0.35^2 = 0.1225$. On the other hand allowing one of the taus to decay hadronically $\tau_h\tau_{lep}$ or $\tau_{lep}\tau_h$ give a coincidence of

$2 \times (0.35 \times 0.65) = 0.455$. This is the best compromise of detector efficiency and branching ratio for di-tau analyses, and this is the principle behind the design of the *Lepton + Track* triggers.

The search for vector leptoquarks pair produced at the CDF experiment is one of the investigations using this trigger data. The $VLQ3$ search is conducted with 322 pb^{-1} of data taken with the *Lepton+Track* triggers between March, 29, 2002 and August 22, 2004. In this chapter, we cover the details of the specific trigger paths and the resulting analysis dataset. Details of how the signal Monte Carlo datasets are created are given at the end of the chapter.

6.1 Overview

The primary crude selection of events in the data sample is performed online by the CDF trigger system. Events passing certain criteria at each of the three trigger levels are passed on through trigger paths and enter into the *TAU_LEPTON* dataset. The first of the triggers feeding this dataset is a low E_T electron plus isolated track trigger, *TAU_ELECTRON8_TRACK5_ISO*. The muons have two paths both, of which are low p_T muon plus isolated track triggers. The first requires a hit in both the CMU and CMP muon chambers and is called *TAU_CMUP8_TRACK5_ISO*. The second muon trigger path requires a hit in the CMX and that trigger path is called *TAU_CMX8_TRACK5_ISO*. The two muon trigger paths cover different η for the different muon detectors as detailed in Section 4.2.3. It is possible for a single event to pass more than one trigger and so enter the dataset by two independent trigger paths.

The specific trigger selection criteria[1] are discussed in detail below. Briefly,

[1]The trigger selection criteria are taken directly from the trigger table data summaries.

Level 1 attempts to match particle tracks with either deposits of energy in the CEM (electrons) or with hits in the muon chambers (muons). Level 2 repeats this matching with a finer granularity while beginning event reconstruction. Here cuts can be applied based on partial event information, the profile of energy deposits in neighboring calorimeter towers or a second track in the COT. Cuts based on full event information can be applied at Level 3, which performs a simplified version of the full offline event reconstruction.

One of the Level 3 requirements present in all three trigger paths is the *tau-like isolation* requirement. This is applied to the track which is intended to become the tau seed track. The requirement is that within an annulus of $0.175 < \Delta R < 0.524$ around the seed track there are no tracks with $p_T \geq 1.5$ GeV/c and $|\Delta z_0| < 15$ cm. The inner annulus allows for multiple tracks originating from the decay of the same tau.

When discussing the electrons, muons and the various trigger level requirements for each, it is important to make the distinction between the actual particle produced and the software object by which it may or may not be represented. For instance an electron object is built up from an energy deposition in the calorimeters above a certain threshold and a track object with sufficient p_T pointed at the corresponding calorimeter tower. However, other processes occurring in the event or secondary interactions with the detector material could produce a particle which "fakes" an electron from the primary collision. Likewise an actual particle with a trajectory along say the beam pipe or some other gap in detector coverage can escape without registering in any instrument.

These are available online via the CDF Run Summary Database.

6.2 Electron + Track Trigger

The single electron trigger path TAU_ELECTRON8_TRACK5_ISO consists of requirements at all three trigger levels. Requirements at one trigger level are frequently repeated at another. For instance an electron candidate is required to have deposited a minimum of 8 GeV in the CEM calorimeter at both level 1 and Level 2. At Level 1 calorimeter tower energies are read out in pairs so the requirement is that any two paired CEM towers have greater than 8 GeV. Level 2 examines each calorimeter tower independently during the clustering process and so the 8 GeV requirement here applies to a single tower. In the listing below, only substantively new trigger requirements are listed for each subsequent trigger level.

The second track requirement (10 degree ¡ ϕ separation) listed for Level 2 is added to the trigger tables for latter runs. This change brought down the effective trigger rate encountered as the Tevatron delivered higher instantaneous luminosities.

For TAU_ELECTRON8_TRACK5_ISO the requirements are:

- Level 1

  L1_CEM8_PT8 requires a CEM trigger tower with $E_T > 8$ GeV and a matching XFT track with $p_T \geq 8.34$ GeV/c. In addition the ratio of energy deposited in the hadronic and electromagnetic calorimeters E_{had}/E_{em} is required to be less than 0.125.

- Level 2

  L2_CEM8_PT8_CES3_&_TRK5_DPHI10. Clustering takes place at Level 2 and the cluster seed tower is required to have ≥ 8 GeV. The cluster shoulder formed from neighboring towers is required to have ≥ 7.5 GeV.

Level 2 also requires a second track separated from the first XFT track by at least 10 degrees in ϕ. This track must satisfy $E_T \geq 3$ GeV and $p_T > 5.18$ GeV/c.

- Level 3

  L3_ELECTRON8_TRACK5_ISO requires a central electron with $E_T > 8$ GeV, central track $p_T \geq 8$ GeV/c, $|\eta| \leq 1.5$. and the calorimeter cluster must have a minimum of 3 towers. The second track must possess tau-like isolation.

6.3 Muon + Track Trigger

Where electron candidates were triggered on E_T, muons are selected on transverse momentum p_T measured from the XFT track curvature. There are two trigger paths for muons. In the central region a coincidence between the CMU and the CMP muon chambers is required.

This trigger is called TAU_CMUP8_TRACK5_ISO.

- Level 1

  L1_CMUP6_PT4 requires a CMU stub with $p_T \geq 6$ GeV/c, a matching XFT track with $p_T \geq 4.09$ GeV/c and a matching hit in the CMP.

- Level 2

  L2_CMUP6_PT8 requires matching hits in both CMU and CMP and an XFT with $p_T \geq 8.34$ GeV/c and hits in at least 4 COT superlayers.

- Level 3

  L3_CMUP8_TRACK5_ISO requires $p_T \geq 8$ GeV/c, and $|\eta| \leq 1.5$. Corresponding hits in both CMU and CMP muon chambers are required. The

projected muon trajectory must match stubs in the plane transverse to the beam line within 20 cm for CMP and 15 cm for CMU. Level 3 also requires a second track with tau-like isolation.

A second muon trigger path is also available to increase the η range for muons: TAU_CMX8_TRACK5_ISO.

- Level 1

  L1_CMX6_PT8_CSX required a CMX stub with $p_T \geq 6$ GeV/c, a matching XFT track with $p_T \geq 8.34$ GeV/c. The XFT track is required to have hits in at least 4 superlayers.

- Level 2

  L2_AUTO_L1_CMX6_PT8_CSX references a package called L2_AUTO and automatically passes the event through to Level 3.

- Level 3

  L3_CMX8_TRACK5_ISO requires a CMX muon stub with a minimum $p_T \geq 8$ GeV/c and $|\eta| \leq 1.5$. The projected muon trajectory must match the CMX muon stubs in the plane transverse to the beam line within 30 cm. A second track with tau-like isolation is required.

6.4 Signal Monte Carlo

Signal Monte Carlo (MC) datasets used in this analysis are generated using a modified version of the run dependent MC framework common to all CDF electroweak analyses. This process consists of several discrete steps. First, the vector leptoquark events are generated using the GRACE/GR@PPA and written to file

using the Les Houches common interface [55]. A standard CDF package containing PYTHIA [56], which has been modified to accept events in the Les Houches format, is employed to simulate the decays of any partons remaining in the event. The output of PYTHIA is passed to the CDF detector simulation package. CDF-Sim which is a GEANT application generates the various detector responses that would be produced by the presence of a particle in the detector with the energy, momentum and charge specified by PYTHIA. TrigSim simulates in software the trigger level decisions that would happen in the Level 1 and 2 hardware and in the Level 3 software farm. During Production the simulated data stream from the detector is formatted into data banks accessible by the AC++ data analysis framework. The vector leptoquark analysis uses data sets reduced in size and optimized for speed of access by StntupleMaker.

The internal details of the GRACE/GR@PPA framework is detailed in section 3. For a single event, the event file generated at this stage contains information on only eight particles. These are the parent partons, the $VLQ3$ pair and the immediate decay daughters of each. The particle type and the components of their four vector momentum are the only pieces of information preserved. A summary of the entire data set contains the production cross section.

Run dependent PYTHIA Monte Carlo data files are produced with offline version 5.3.3. of the CDF software packages. Run dependent means that the conditions present in the detector: calibrations, detector configurations and recorded luminosity are used in the simulation of the response of the various detector subsystems. We used the 848 runs listed in runlist_v7goodrunlist_1001. These are the runs listed in the offline database as good, i.e. all of the relevant detector subsystems were functioning during this run.

At the stage of simulation handled by PYTHIA only the run luminosity is

referenced. PYTHIA adds the initial and final state parton showers and simulates the hadronization and decays the τ and b from the leptoquark. A final overall p_T of the hard interaction is determined and a generator level requirement is imposed through the application of *TauFinderModule*. We require that each event contain a hadronically decaying tau τ_h and a leptonically decaying tau of the appropriate flavor τ_e or τ_μ. No requirement that the tau be descended from a $VLQ3$ is imposed at this point. CDFSim, TrigSim, Production and StntupleMaker are all used without modification.

In the analysis an event topological check on generator level information is imposed at run time. A hadronically decaying tau τ_h descended from a $VLQ3$ and a leptonically decaying tau τ_e or τ_μ descended from a $VLQ3$ are both required. We also imposed an additional detector requirement that the Silicon detector be marked good in the offline database.

Vector leptoquark Monte Carlo samples were generated for masses from 160 GeV to 400 GeV in steps of 20 GeV. Samples of 500,000 events were generated at each of these mass points. The number of events simulated per run is proportional to the recorded luminosity. The total number of events to be simulated is chosen such that the analysis is not limited by statistics. We were left with working sample sizes of around 45,000 events at each of the mass points in each of the decay channels.

Chapter 7

Offline Selection

The online trigger selections are based primarily on balancing the collection of high interest events, in our case *lepton + track* events, with the rate at which the DAQ system can write events to tape. Consequently the online selection is quite permissive with regard to event quality. This approach allows datasets to be defined that are suitable for a wide variety of analyses. Datasets must also support studies of both detector response and various efficiencies. Event quality is addressed offline in three stages of the analysis itself. In this chapter details the various stages of offline selection.

The first stage is the geometric acceptance selection. These selections are intended to ensure that reconstruction of physics objects has occurred in portions of the detector where triggering and efficiency are well understood. The cylindrical geometry of the CDF detector limits the solid angle coverage to low values of η. We also require fairly central values of z for both the position at the at the beam line z_0 and at radii specific to various detector subsystems such as Z_{RCES} at the radius of the shower max detector.

Separation requirements are imposed between the acceptance stage and the

identification stage which immediately follows. We do this to keep from convoluting physics objects. While the detector response for electron and jet candidates have both undergone extensive study, the detector response to an electron and jet in close proximity are less well understood.

Identification (ID) requirements are in place to ensure the quality (purity) of the specific particle candidate. All identification requirements include a track quality check for a sufficient numbers of hits in COT axial and stereo superlayers and that within the superlayers themselves a sufficient number of segments have been triggered. An additional E_{had}/E_{EM} as a function of E_T requirement is put in place for electron candidates. Limits on the energy deposition in the calorimeters are imposed on the muon candidates. Tau candidates are required to possess an odd number of tracks. Additional fiducial requirements are imposed on all three particle candidate types.

7.1 Offline Efficiency

Candidate events used to evaluate the acceptance, ID and separation efficiencies are from signal Monte Carlo. The process used to generate the events imposes a requirement that the event possess a tau decaying hadronically and a tau decaying to the appropriate flavor of lepton. This filtering at the generation stage does not guarantee that the taus are from the vector leptoquark event. In order to properly evaluate the efficiencies all events are subjected to HEPG (Monte Carlo generator level) matching to verify that each event has to proper particle topology with one $VLQ3 \rightarrow \tau_h b$ and the other $VLQ3 \rightarrow \tau_l b$. A HEPG leptonically decaying tau and a hadronically decaying tau daughter are identified. Both are traced back to a parent $VLQ3$ particle or the event is vetoed. Once identified as an actual

$VLQ3$ event a $\Delta R = \sqrt{\Delta\eta^2 + \Delta\phi^2}$ requirement of $\Delta R < 0.2$ between the HEPG object and the reconstructed object is imposed.

The effect of this HEPG matching on the final efficiency is estimated by removing the ΔR requirement, which allows an additional 4,157 events into the sample. The number of events being considered by the analysis is identical after the acceptance and particle ID selections. This is a testimony to the effectiveness of the selections even prior to event level cuts in ensuring event quality. The effect on the final efficiency is estimated by considering one additional hypothetical event which passes all selection cuts. The magnitude of the effect is smaller than the uncertainty of the efficiency, 0.2%. The effect of the HEPG matching requirement on our analysis is negligible.

The total efficiency for offline selection is factored as follows:

$$\epsilon_{total} = \epsilon_{acc}\epsilon_{lepton}\epsilon_{tau}\epsilon_{event} \tag{7.1}$$

where

$$\epsilon_{acc} = \epsilon_{acc(lep)}\epsilon_{acc(tau)}\epsilon_{sep(lep,tau)} \tag{7.2}$$

$$\epsilon_{lepton} = \epsilon_{sep(lep,jet)}\epsilon_{ID(lep)}\epsilon_{iso(lep)}\epsilon_{trig(lep)} \tag{7.3}$$

$$\epsilon_{tau} = \epsilon_{sep(tau,jet)}\epsilon_{ID(tau)}\epsilon_{iso(tau)}\epsilon_{trig(tau)} \tag{7.4}$$

All efficiency terms are sequential. The electron and muon acceptance terms $\epsilon_{acc(lep)}$ are detailed in sections 7.2.1 and 7.2.2 respectively. Tau acceptance $\epsilon_{acc(tau)}$, Section 7.2.3 are evaluated next. The separation term $\epsilon_{sep(lep,tau)}$ is included within the acceptance section in order to keep the detector response to both lepton and tau in a well-understood regime and is calculated with respect

to all events passing $\epsilon_{acc(tau)}$.

The lepton efficiency ϵ_{lepton} is calculated for events passing acceptance and consists, of in order: a lepton-jet separation $\epsilon_{sep(lep,jet)}$, followed by the actual lepton ID $\epsilon_{ID(lep)}$ and lepton isolation $\epsilon_{iso(lep)}$. A lepton trigger efficiency $\epsilon_{trig(lep)}$ is applied to signal MC. All efficiencies are evaluated with respect to events which have passed the previous stages.

The hadronic tau efficiency ϵ_{tau} is calculated with respect to events which have passed the lepton ID requirements. Again the factors are evaluated in terms of events passing the previous stage. In order these efficiencies are a tau jet separation $\epsilon_{sep(tau,jet)}$, the hadronic tau ID $\epsilon_{ID(tau)}$ and tau isolation efficiency $\epsilon_{iso(tau)}$. Finally a tau trigger efficiency $\epsilon_{trig(tau)}$ is applied to signal MC.

The event efficiency ϵ_{event} is calculated with events which have passed all acceptance, lepton and tau requirements.

7.2 Geometric Acceptance

Acceptance level cuts are imposed first on the candidate lepton (electron or muon). The hadronic tau acceptance cuts are applied next. Any candidate leptons and taus are then checked for a ΔR separation. The acceptance efficiencies are mass dependent (see Figure 9.6) and so all acceptance efficiencies are given for $m_{VLQ3} = 320$ GeV/c^2. Acceptance requirements and efficiencies are listed in in Tables 7.2 and 7.2.

7.2.1 Electron Acceptance

All reconstructed objects of type CdfEMObject that pass the following requirements are considered electron candidates.

Electron:	$e\tau_h$ Efficiency (%)
CdfElectrons	79.6 ± 0.1
CEM	85.2 ± 0.1
$E_T^{\rm corr} > 10$ GeV	88.4 ± 0.1
$p_T > 8$ GeV/c	96.2 ± 0.1
$\|z_0\| < 60$ cm	97.0 ± 0.1
Fiducial	82.9 ± 0.2
Subtotal	46.3 ± 0.2
Tau:	
CdfTau	72.7 ± 0.2
$\|\eta_{\rm det}\| < 1.0$	87.5 ± 0.2
$E_T^{\rm corr} > 15$ GeV	98.4 ± 0.1
$p_T^{\rm seedtrk} > 6$ GeV/c	98.9 ± 0.1
Fiducial	90.4 ± 0.2
Subtotal	56.0 ± 0.2
$\Delta R(\tau_h, \ell) > 0.7$	96.7 ± 0.1
Subtotal	25.1 ± 0.1
Scale Factor	1.000 ± 0.015
Total Acceptance	$25.1 \pm 0.1 \pm 0.4$

Table 7.1: Summary of acceptances for the $e\tau_h$ channel, shown for $m_{VLQ3} = 320$ GeV/c^2. The details of the acceptance requirements are given in the text.

Muon:	$\mu_{CMUP}\tau_h$ Efficiency (%)	$\mu_{CMX}\tau_h$ Efficiency (%)
CdfMuon	71.7 ± 0.1	71.7 ± 0.1
CMUP/CMX	45.2 ± 0.2	21.5 ± 0.2
$p_T > 10$ GeV/c	92.5 ± 0.2	89.1 ± 0.3
$\|z_0\| < 60$ cm	96.9 ± 0.1	96.7 ± 0.2
Fiducial	98.0 ± 0.1	68.3 ± 0.4
Subtotal	28.4 ± 0.1	9.1 ± 0.1
Tau:		
CdfTau	73.3 ± 0.3	72.6 ± 0.5
$\|\eta_{\rm det}\| < 1.0$	87.8 ± 0.2	87.5 ± 0.4
$E_T^{\rm corr} > 15$ GeV	98.6 ± 0.1	98.3 ± 0.2
$p_T^{\rm seedtrk} > 6$ GeV/c	99.1 ± 0.1	99.1 ± 0.1
Fiducial	90.3 ± 0.2	90.0 ± 0.4
Subtotal	56.7 ± 0.3	55.6 ± 0.5
$\Delta R(\tau_h, \ell) > 0.7$	96.3 ± 0.2	97.4 ± 0.2
Subtotal	15.5 ± 0.1	4.9 ± 0.1
Scale Factor	0.941 ± 0.017	0.987 ± 0.015
Total Acceptance	$14.6 \pm 0.1 \pm 0.2$	$4.8 \pm 0.1 \pm 0.1$

Table 7.2: Summary of acceptances for the $\tau_\mu \tau_h$ channel, shown for $m_{VLQ3} = 320$ GeV/c^2. The details of the acceptance requirements are given in the text.

- Central (CEM bit set)
- $E_T^{corr} \geq 10$ GeV (corrected energy)
- $p_T \geq 8$ GeV/c
- $|z_0| < 60$ cm
- Fiducial in Shower Max: $|x_{CES}| < 21.5$ cm and 9 cm $< z_{CES} < 230$ cm
- Fiducial in COT: $|z_{COT}| < 150$ cm at outer radius $R_{COT} = 137$ cm

7.2.2 Muon Acceptance

All reconstructed objects of type CdfMuon that pass the following requirements are considered muon candidates.

- Muon Stub (CMUP or CMX bit set)
- $p_T \geq 10$ GeV/c
- $|z_0| < 60$ cm
- Fiducial in CMUP or CMX
- Fiducial in COT: $|z_{COT}| < 150$ cm at outer radius $R_{COT} = 137$ cm

7.2.3 Hadronic Tau Acceptance

All reconstructed objects of type CdfTau that pass the following requirements are considered hadronic tau candidates.

- $|\eta_{det}| < 1.0$

Requirement	$e\tau_h$ Efficiency (%)
Veto $0.3 < \Delta R(\ell, \text{jet}) < 0.8$	90.3 ± 0.2
Lepton $I_{\text{trk}}^{\Delta R<0.4} < 2$ GeV/c	88.4 ± 0.2
Veto $0.3 < \Delta R(\tau, \text{jet}) < 0.8$	90.3 ± 0.2
$N_{\text{trk}}^{\tau\ \Delta\Theta} = 0$ and $N_{\text{trk}}^{\tau\ \Delta R} = 0$	82.3 ± 0.4
Tau $I_{\pi^0}^{\Delta\Theta} \leq 0.6$ GeV/c	96.1 ± 0.2
Scale Factor	1.00 ± 0.03

Table 7.3: Separation and isolation efficiencies for the τ_e_h channel, evaluated for the case of $m_{VLQ3} = 320$ GeV/c^2.

- $E_T^{corr} \geq 15$ GeV (corrected energy)
- $p_T^{seed} \geq 6$ GeV/c (corrected energy)
- Seed track fiducial in Shower Max: 9 cm $< z_{CES} <$ 230 cm
- Seed track fiducial in COT: $|z_{COT}| < 150$ cm at radius $R_{COT} = 137$ cm

7.2.4 Lepton-Tau Separation

The lepton-tau separation requirement is imposed only after the event has passed the acceptance requirements. For this requirement the tau visible momentum (the sum of the tracks and π^0 E_T within the tau cone) are compared to the track momentum of the lepton candidate. We require that the ΔR separation be greater than 0.7.

7.2.5 Scale Factors

Signal MC events passing the lepton acceptance, hadronic tau acceptance and the separation requirement constitutes the total acceptance. Efficiencies for various lepton candidates are corrected by scale factors to ensure that any differences in

Requirement	$\mu_{\mathrm{CMUP}}\tau_h$ Efficiency (%)	$\mu_{\mathrm{CMX}}\tau_h$ Efficiency (%)
Veto $0.3 < \Delta R(\ell, \mathrm{jet}) < 0.8$	88.5 ± 0.3	90.8 ± 0.4
Lepton $I_{\mathrm{trk}}^{\Delta R<0.4} < 2$ GeV/c	94.9 ± 0.2	95.4 ± 0.3
Veto $0.3 < \Delta R(\tau, \mathrm{jet}) < 0.8$	88.5 ± 0.3	90.8 ± 0.4
${N_{\mathrm{trk}}}^{\tau\,\Delta\Theta} = 0$ and ${N_{\mathrm{trk}}}^{\tau\,\Delta R} = 0$	82.3 ± 0.5	83.0 ± 0.8
Tau $I_{\pi^0}^{\Delta\Theta} \leq 0.6$ GeV/c	96.2 ± 0.3	96.2 ± 0.4
Scale Factor	1.00 ± 0.03	1.00 ± 0.03

Table 7.4: Separation and isolation efficiencies in the $\tau_\mu\tau_h$ channel, evaluated for the case of $m_{VLQ3} = 320$ GeV/c^2.

the efficiencies with data are reflected in our signal MC studies. Details are listed in Tables 7.2 and 7.2.

Differences between the stub (muon chamber hit) finding efficiency between MC and data is compensated for with a correction factor. The CMUP scale factor is 0.941 ± 0.008. For CMX the scale factor is 0.987 ± 0.003.

These scale factors are derived for high p_T muons, $p_T \geq 20$ GeV/c [57]. While the p_T range for this analysis goes down to 10 GeV/c these lower p_T muons represent only 10-15% of the leptons from vector leptoquarks. Additionally, muon reconstruction efficiency is not momentum dependent. A 2.5% effect enters a contribution of 0.3% on the final scale factor. This represents a small effect compared to other systematics. The systematics applied to each decay channel are detailed in Tables 10.5 and 10.6

For the $e\tau_h$ channel, track reconstruction contributes 1.4% and interaction with detector materials another 0.4%. The track reconstruction component includes 0.4% for the electron. Taus contribute 0.4% for the 1-prong taus, and 3% for the 3-prong taus weighted in such a way as to account for the ratio of 1-prong to 3-prong taus.

7.3 Lepton-Jet Separation

The leptons which have already passed all of the acceptance criteria may still be rejected if they are too close to a jet candidate. A lepton will is vetoed if it falls within an annulus of $0.3 < \Delta R(lep, jet) < 0.8$ with respect to any jet object. Note that the inner edge of the annulus prevents a lepton from being vetoed by the jet candidate associated with the calorimeter cluster from which both jets and CdfEmObjects are reconstructed.

7.4 Identification Requirements

Particle identification cuts are implemented to ensure that particle candidates in the fiducial regions of the detector are of sufficient quality to ensure accurate reconstruction. Misidentification of particles or "fake rates" are to be minimized at this point.

7.4.1 Jets

The signal event signature $\tau_h \tau_{lep} bb$ gives rise to two jets from the hadronization of the b quarks. Two of the event level selection criteria are based on jets. These are the H_T cut, see Section 9.7 and the jet multiplicity cut, see Section 9.8. The accurate reconstruction of jets and their energies optimizes the jet separation requirements and the $\not\!\!E_T$ corrections.

Jets are reconstructed using the JETCLU module with a cone size of $\Delta R = 0.4$. The jet energy is corrected through the CDF jet energy corrections level 5. Which means that corrections for energy losses in uninstrumented and non-linear regions of the calorimeter are applied. Jet energy is also adjusted for the sum p_T

of tracks within the jet cone [58].

The jet objects passing the following criteria are written to a jet collection. Any further reference to jets in this analysis refers to jets meeting these requirements.

- $|\eta_{det}| < 2.4$
- $E_T^{raw} \geq 10$ GeV
- $E_T^{corr} \geq 15$ GeV
- $\Delta R(lep, jet)$ and $\Delta R(\tau_h, jet) > 0.8$

7.4.2 Electron Identification

The electron ID requirements and efficiencies are given in Table 7.5. The track quality criteria is 3x5,3x5, meaning that there must be at least 5 hits in 3 axial superlayers and at least 5 hits in 3 stereo superlayers.

A scale factor $f_{\mathrm{CEM}}^{\mathrm{ID}} = 1.00 \pm 0.01$ is applied to the ID efficiency to ensure a match in the efficiency of MC and data. The scale factor is determined from studies of electron efficiencies in $Z \rightarrow e^+e^-$ and $\Upsilon \rightarrow e^+e^-$ datasets. This approach allows the selection of a narrow mass window to suppress backgrounds [59, 60]. The ratio of $\epsilon_{data}/\epsilon_{\mathrm{MC}}$ is measured. The scale factor from both studies is 1.00. This is a standard scale factor applied this and to other analyses [23].

The uncertainty takes a weighted combination of the uncertainties from both of the cited studies. The high p_T study $p_T > 20$ GeV/c result is 1.000$\pm$0.005 and the medium range p_T study result is 1.000$\pm$0.025. More than 80% of the electrons resulting from $VLQ3$ decay fall into the high p_T range and so a conservative weight of 0.8 is assigned to the high p_T uncertainty. A 0.2 weight is assigned to

Requirement	Efficiency (%)
Track Quality	99.9 ± 0.0
$E_{\rm had}/E_{\rm em} < 0.055 + 0.00045 * E$	98.4 ± 0.1
$E_T^{\rm corr}/p_T < 2.0$ for $E_T^{\rm corr} < 50$ GeV	90.2 ± 0.2
$-3.0 < Q * \Delta x_{\rm CES} < 1.5$ cm	98.9 ± 0.1
$\lvert\Delta z_{\rm CES}\rvert < 3$ cm	99.6 ± 0.1
$\chi^2_{z\ \rm CES} < 10$	96.4 ± 0.1
$\rm L_{shr} < 0.2$	98.4 ± 0.1
$d_0 < 0.2$ cm	99.5 ± 0.1
Subtotal	82.4 ± 0.3
Scale Factor	1.00 ± 0.01
Total ID Efficiency	$82.4 \pm 0.3 \pm 0.8$

Table 7.5: Electron identification requirements and efficiencies, for the case of $m_{VLQ3} = 320$ GeV/c^2. The details of the track quality requirement are given in the text.

the medium range p_T uncertainty. The weighted value is $(0.8)0.005+(0.2)0.025 = 0.009$. Again being conservative we assign an uncertainty of 1.0 % to our scale factor.

7.4.3 Muon Identification

The muon ID requirements and efficiencies are given in Table 7.6. The track quality requirements are the same as used for the electron ID given in Section 7.4.2.

A scale factor is assigned to the muon identification to make the efficiency of $VLQ3$ signal MC match the efficiency of muons from data. The scale factors are derived in [26] from efficiency studies done in [57] and [61].

Requirement	CMUP muons Efficiency (%)	CMX muons Efficiency (%)
Track Quality	100.0 ± 0.0	100.0 ± 0.0
$E_{\rm EM} < 2$ and $E_{\rm had} < 6$	91.6 ± 0.2	0.0 ± 0.0
$d_0 < 0.2$ cm	99.9 ± 0.0	99.9 ± 0.1
($\Delta x_{\rm CMU} < 4$ and $\Delta x_{\rm CMP} < 7$)	99.1 ± 0.1	
or $\Delta x_{\rm CMX} < 6$ cm		99.2 ± 0.1
Subtotal	90.7 ± 0.3	90.6 ± 0.4
Scale Factor	0.939 ± 0.030	0.990 ± 0.003
Total ID Efficiency	$85.2 \pm 0.3 \pm 2.7$	$89.7 \pm 0.4 \pm 0.3$

Table 7.6: Muon identification requirements and efficiencies, for the case of $m_{VLQ3} = 320$ GeV/c^2. The details of the track quality requirement are given in the text.

7.4.4 Lepton Isolation

Lepton isolation, $I_{\rm trk}^{\Delta R=0.4}$, is a cut based on the sum of p_T of all tracks within the isolation cone. The isolation cone is centered on the track of the lepton candidate and has $\Delta R = \sqrt{\Delta\eta^2 + \Delta\phi^2} = 0.4$. The lepton isolation requirement is $I_{\rm trk}^{\Delta R=0.4} < 2$ GeV/c.

Separation and isolation requirements and the associated efficiencies are listed in Tables 7.3 and 7.4. The efficiencies are measured with respect to MC. Good agreement between MC and and data is found in studies of $Z^0 \to \tau\tau$ for these requirements. A conservative estimate puts the uncertainty at 3%, intended to account for the differences between $Z^0 \to \tau\tau$ MC and data as well as between our $VLQ3$ signal MC and that study.

7.4.5 Lepton Trigger Efficiency

The triggers used to obtain the analysis dataset are discussed in Chapter 6. By design the *Lepton+Track* triggers are constructed of trigger primitives which allows

Trigger Path	$VLQ3\overline{VLQ3} \rightarrow \tau\tau b\bar{b}$ Efficiency (%)	$Z^0 \rightarrow \tau\tau$ Efficiency (%)	$\tilde{t}_1\bar{\tilde{t}}_1 \rightarrow \tau\tau b\bar{b}$ Efficiency (%)
CEM electron	$97.0 \pm 0.1 \pm 1.0$	$96.0 \pm 0.1 \pm 1.0$	$97.6 \pm 0.2 \pm 1.0$
CMUP muon	$95.9 \pm 0.2 \pm 1.0$	$95.8 \pm 0.1 \pm 1.0$	$95.8 \pm 0.3 \pm 1.0$
CMX muon	$95.8 \pm 0.3 \pm 1.0$	$94.7 \pm 0.3 \pm 1.0$	$94.6 \pm 0.5 \pm 1.0$
TAU tau	$97.0 \pm 0.1 \pm 1.0$	$95.3 \pm 0.2 \pm 1.0$	$96.4 \pm 0.3 \pm 1.0$

Table 7.7: Trigger efficiencies (%) for electron (CEM), muon (CMUP and CMX), and tau (TAU) trigger paths. The effective efficiencies are shown for $VLQ3\overline{VLQ3} \rightarrow \tau\tau b\bar{b}$ using $m_{VLQ3} = 320$ GeV/c^2 MC. For comparison, efficiencies are also shown for $Z^0 \rightarrow \tau\tau$ and $\tilde{t}_1\bar{\tilde{t}}_1 \rightarrow \tau\tau b\bar{b}$ using $m_{\tilde{t}_1} = 150$ GeV/c^2 MC. In each case, the total efficiency is the product of $\epsilon_{\mathrm{L1}} \times \epsilon_{\mathrm{L2}} \times \epsilon_{\mathrm{L3}}$.

for an understanding of the trigger efficiencies as the product of the efficiencies of the trigger primitives [62]. The problem then factorizes into understanding the efficiencies of the lepton and hadronic tau legs of the triggered event separately. Because of the two instruments used to detect muons we effectively have four types of physics objects which need to be understood, CEM electrons, CMUP muons, CMX muons and hadronic taus.

The trigger efficiency for CEM electrons is measured using a sample of conversion candidates from jets [63] and muon data [64]. The trigger efficiencies for the CMUP and CMX muons are measured using samples of $Z^0 \rightarrow \mu^+\mu^-$ and $\Upsilon \rightarrow \mu^+\mu^-$ events [65]. Hadronic tau trigger efficiency is based on the track efficiency of the tau seed track. This efficiency is measured as a function of several tau identification requirements [66, 67].

Trigger efficiencies are applies to signal MC in the analysis. For electrons and taus, there is a p_T dependence to the trigger efficiency and so the efficiency is evaluated event by event as parameterized trigger function. For muons, the trigger efficiency is a constant over the relevant p_T range and so a constant suffices. The results are summarized in Table 7.7.

7.4.6 Tau-Jet Separation

Taus which are too close to a jet candidate are removed from the list of particle candidates. This comparison excludes a separation check with the jet primitive from which the CdfTau object is derived. This check vetoes any tau with a jet within the annulus $0.3 < \Delta R < 0.8$. All separation and isolation efficiencies are contained in Tables 7.3 and 7.4.

7.4.7 Tau Identification

The tau ID requirements and efficiencies are given in Tables 7.8 and 7.9, for both $e\tau_h$ and $\mu\tau_h$ channels. Here the track quality requirement is applied to the tau seed track. The requirement is (3x5,2x5) or 3 hits in the axial superlayers and at least 2 hits in the stereo superlayers. Each superlayer is required to have 5 segments. The tau identification efficiency is scaled by 1.00 ± 0.03, a result obtained from $Z^0 \rightarrow \tau\tau$ studies [68].

At 1.777 GeV/c^2, the tau is a low mass particle and its hadronic decay products will form a low invariant mass. One of the standard tau identification cuts is to reconstruct the invariant mass from the charged tracks and require it to be no larger than 1.8 GeV/c^2. A second cut examines the invariant mass including the neutral pions. We also classify tau candidates by the number of charged track or "prongs." For tau, identification we require 1 or 3 charged tracks within a small solid angle about the tau seed track, also referred to as the signal cone.

Requirement	$e\tau_h$ Efficiency (%)
Seed Track Quality	99.3 ± 0.1
$\lvert z_0^{\tau\ \mathrm{seed}} - z_0^{l\ \mathrm{trk}} \rvert \leq 5$ cm	98.0 ± 0.1
$\lvert d_0^{\tau\ \mathrm{seed}} \rvert < 0.2$ cm	97.3 ± 0.1
$\xi = E_{T\mathrm{had}} / \sum p_T > 0.1$	95.9 ± 0.2
$m_{\mathrm{trk}} \leq 1.8$ and $m_{\mathrm{trk}+\pi 0} \leq 2.5$ GeV/c^2	98.8 ± 0.0
$N_{\mathrm{trk}}^{\tau\mathrm{cone}} = 1, 3$	87.7 ± 0.3
Subtotal	66.1 ± 0.4
Scale Factor	1.00 ± 0.03
Total ID Efficiency	$66.1 \pm 0.4 \pm 0.2$

Table 7.8: Hadronic tau identification requirements and efficiencies in the $\tau_e\tau_h$ channel, for the case of $m_{\mathrm{LQ3}} = 320\,\mathrm{GeV}/c^2$. The details of the track quality requirement are given in the text.

Requirement	$\mu_{\mathrm{CMUP}}\tau_h$ Efficiency (%)	$\mu_{\mathrm{CMX}}\tau_h$ Efficiency (%)
Seed Track Quality	99.1 ± 0.1	99.2 ± 0.2
$\lvert z_0^{\tau\ \mathrm{seed}} - z_0^{l\ \mathrm{trk}} \rvert \leq 5$ cm	97.9 ± 0.1	98.1 ± 0.2
$\lvert d_0^{\tau\ \mathrm{seed}} \rvert < 0.2$ cm	97.0 ± 0.2	97.3 ± 0.3
$\xi = E_{T\mathrm{had}} / \sum p_T > 0.1$	95.5 ± 0.2	95.9 ± 0.4
$m_{\mathrm{trk}} \leq 1.8$ and $m_{\mathrm{trk}+\pi 0} \leq 2.5$ GeV/c^2	98.6 ± 0.0	98.6 ± 0.0
$N_{\mathrm{trk}}^{\tau\mathrm{cone}} = 1, 3$	87.6 ± 0.4	88.3 ± 0.6
Subtotal	66.1 ± 0.5	67.5 ± 0.8
Scale Factor	1.00 ± 0.03	1.00 ± 0.03
Total ID Efficiency	$66.1 \pm 0.5 \pm 0.2$	$67.5 \pm 0.8 \pm 0.2$

Table 7.9: Hadronic tau identification requirements and efficiencies in the $\tau_\mu\tau_h$ channel, for the case of $m_{\mathrm{LQ3}} = 320\,\mathrm{GeV}/c^2$. The details of the track quality requirement are given in the text.

7.4.8 Tau Isolation

Tau isolation is defined with respect to a cone centered on the tau seed track. Tau candidates not meeting the following requirements are vetoed. There may be no candidate tracks within an annulus of defined by a 10° inner or signal cone and a 30° outer or isolation cone. For highly boosted taus the signal cone can be shrunk to as small as 0.05°. Since many times tau hadronic decays produce neutral particles, we also require π^0 isolation, $\Sigma p_T \leq 0.6\,\mathrm{GeV}/c$. The tau isolation criteria are summarized below, and the corresponding efficiencies are reported in Table 7.3 and 7.4.

- ${N_{\mathrm{trk}}^{\tau}}^{\Delta\Theta} = 0$
- ${N_{\mathrm{trk}}^{\tau}}^{\Delta R} = 0$
- $I_{\pi^0}^{\Delta\Theta} < 0.6\,\mathrm{GeV}/c$

A schematic of the tau cone configuration is given in Figure 7.1.

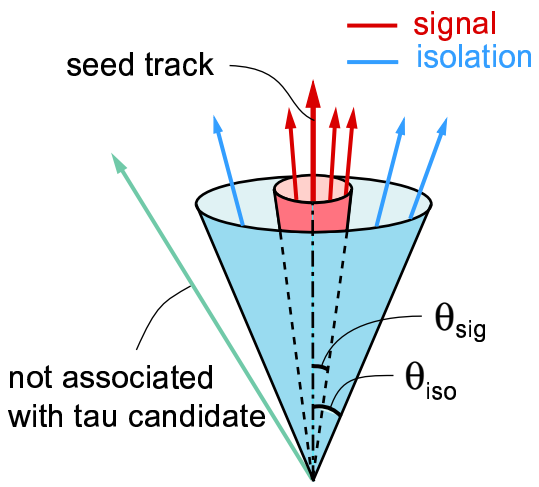

Figure 7.1: Tau tracking isolation uses a small signal cone about the tau seed track to allow for multiple charged tracks associated with the parent tau. A larger isolation cone is used to define the outer extent of an annulus within which no other tracks are allowed. In the pictured case the candidate tau fails because of the number of charged tracks in the signal cone. In the example given, the tau candidate is most likely a hadronic jet.

Chapter 8

Backgrounds

A background is a non-signal process that enters the data sample. In dealing with a small cross section signal the issue of discriminating between these backgrounds and our analysis signal becomes a major focus of the analysis. In order to mask or mimic our $VLQ3$ signature each of the processes must be able to produce or through some confluence of factors to fake a τ_h, a τ_{lep} and two jets. Nearly all of the backgrounds to be discussed involve some level of jet misidentification or jets faking some part of our event signature. Table 8.1 gives rate at which jets fake different kinds of particle candidates [69, 70].

Particle Type	Fake Rate
CEM Electron	$1.3 \times 10^{-4} + exp(-7.94 - 0.194 \times E_T)$
CMUP Muon	$8.6 \times 10^{-4} + 1.7 \times 10^{-4} \times p_T)$
CMX Muon	$8.2 \times 10^{-4} + 2.0 \times 10^{-4} \times p_T)$
Hadronic Tau	0.07 to 0.01 decreasing exponentially with jet E_T

Table 8.1: Lepton fake rate for jets for electrons, muons and hadronic taus. The fake rate satisfying tight lepton identification requirements. Quark jets generate a lot of tracking activity, hence the higher fake rate for hadronic taus.

8.1 Top Quark Pairs

The pair production of top quarks is one of the major backgrounds for this analysis. Despite its small cross section at the Tevatron (assumed to be 6.7 pb) this process $t\bar{t} \rightarrow (W \rightarrow \tau_l + \nu)b(W \rightarrow \tau_h + \nu)b$ can mimic our signal. The top quark, with its 5×10^{-24} s lifetime, does not have time to form quark bound states and so decays with a nearly 100% branching ratio to $t \rightarrow W + b$. The hadronization of the b quarks form the jet portion of our signature. The Ws can subsequently decay to an appropriate $\tau_{lep}\tau_h$ combination or with one W decaying directly to an $e\nu$ or $\mu\nu$. In the case where the actual τ_h or lepton is not produced from the $t\bar{t}$ pair an extra jet present in the event can still fake the missing particle. In this case an additional jet in the event is required to meet the $N_{jets} \geq 2$ requirement. This background was studied with 0.2 million events from PYTHIA MC dataset ttop0z. It is also interesting to note that the most significant discovery of the CDF Run I experiment, the top quark, has for this analysis, become for many exotic particle searches, simply another background for many exotic particle searches.

8.2 $Z^0/\gamma \rightarrow \tau^+\tau^-$

With the presence of two jets, in the event $Z^0/\gamma \rightarrow \tau^+\tau^-$ can mimic the $VLQ3$ signal when one tau passes acceptance and ID as a τ_h and the other as τ_{lep} potentially contributing to either the $e\tau_h$ or $\mu\tau_h$ channel. The contributions from these backgrounds were estimated with a PYTHIA MC dataset zewk8t containing 7.6 million events.

8.3 $Z^0/\gamma \rightarrow e^+e^-$ and $Z^0/\gamma \rightarrow \mu^+\mu^-$

There are two scenarios by which the $Z^0/\gamma \rightarrow l^+l^-$ can contaminate either the $e\tau_h$ or $\mu\tau_h$ channel. First, in an event with two suitable jets the lepton fakes a hadronic tau. The second scenario: an event with three suitable jets in which one of the lepton is missing, not reconstructed or did not pass acceptance and ID requirements, with one jet faking a hadronic tau. $Z^0/\gamma \rightarrow e^+e^-$ studies were conducted with 2.9 million events from dataset zewk6d. $Z^0/\gamma \rightarrow \mu^+\mu^-$ studies were conducted with 3.1 million events from dataset zewk6m.

8.4 $W + jets$

Contamination from this source requires that the W decay to a suitable electron or muon plus three jets one of which fakes a hadronic tau. The W also could decay to a τ which subsequently decays to $e\nu$ or $\mu\nu$.

A mismatch between MC and data for the jet multiplicity bins ($N_{jets} = 0, 1$ and 2) requires that scaling factors be established to get PYTHIA MC to match data for each N_{jet} bin. The transverse mass (M_T), defined for electrons in equations 8.1 and for muons in Equation 8.2, isolates the $W + jets$ background.

$$M_T = \sqrt{2E_T^e \not{E}_T \ \ (1 - \cos\Delta\phi)} \tag{8.1}$$

$$M_T = \sqrt{2p_T^\mu \not{E}_T \ \ (1 - \cos\Delta\phi)} \tag{8.2}$$

where $\Delta\phi$ is the angle between the lepton and the $\not{E}_T$ direction. This can be seen in Figures 9.16 and 9.17 where the jet multiplicities are for the fairly stiff jet criteria defined in Section 7.4.1. For $M_T > 40$ GeV the $W + jets$ contribution

N_{jets}	Scale Factor
0	$0.58 \pm 0.06 \pm 0.09$
1	$0.74 \pm 0.13 \pm 0.11$
≥ 2	$0.84 \pm 0.38 \pm 0.13$

Table 8.2: Scale factors to normalize the $W+$jets background from Monte Carlo simulation to data. The first uncertainty is statistical, the second is a systematic.

dominates for $N_{jets} = 0$ and 1, while in $N_{jets} \geq 2$ this background in comparable with other backgrounds.

The scale factor for each jet multiplicity bin was determined by minimizing a χ^2 between data and the sum of all backgrounds. Increased statistics were achieved by combining events from the $e\tau_h$ and $\mu\tau_h$ samples and loosening ID requirements on the hadronic tau candidates. Tau isolation was dropped from $p_T > 1$ GeV to $p_T > 2$ GeV. The N_{tracks} requirement in the 10 to 30 degree cone was dropped and the track + π^0 mass cut was increased to 4 GeV/c^2. The opposite sign requirement was also dropped.

A look at the difference between M_T from PYTHIA MC and data between $40 \leq M_T \leq 60$ GeV in Figures 9.16 and 9.17 for $N_{jets} = 2$ shows what is possibly a statistical variation between the two points. The difference between the scale factors determined for $M_T < 40$ GeV and determined again for $M_T < 60$ GeV is attributed to a systematic uncertainty. The resulting scale factors are listed in Table 8.2.

This background was modeled using PYTHIA MC datasets, $W \rightarrow e\nu$ from wewkfe (5.4 million events), $W \rightarrow \mu\nu$ from wewk6m (3.1 million events) and $W \rightarrow \tau\nu$ from wewk9t (8.7 million events).

8.5 Diboson

The production of WW, WZ and ZZ could conceivably contaminate our signal through the subsequent decay one or both bosons to $e\nu$ or $\mu\nu$ supply the lepton component of the $VLQ3$ signal. Some combination of the decay of a remaining boson and/or jets faking a hadronic tau are required to produce candidate a hadronic tau and at lest two jets. Background studies were conducted from PYTHIA MC datasets, WW from wtop1w (0.4 million events), WZ from wtop1z (0.4 million events) and ZZ from ztopcz (0.4 million events). The contributions from Diboson processes were found to be negligible primarily due to the small cross section.

8.6 QCD

Light quark backgrounds can contaminate the $VLQ3$ signal when one of the associated jets fakes a lepton of the appropriate flavor and another fakes a hadronic tau. Additional jets must be present in the event to pass the $N_{jets} \geq 2$ requirement.

Heavy flavor quark backgrounds can give real leptons from semileptonic decays of heavy mesons, "real" leptons from the semileptonic decays of heavy flavor mesons and heavy flavor jets faking hadronic taus. For instance a jet containing a $D^{\pm}$ with mass 1.9 GeV/c^2 and decaying to three pions can easily mimic the 1.8 GeV/c^2 tau.

QCD backgrounds are estimated using a sideband method as described in [68, 71]. A plot of lepton isolation from that study, shown inn Figure 8.1 shows that in the non-signal region the QCD background is both dominant and flat.

The sideband region used in those studies extends from 2 to 8 GeV in isolation, while we extended the sideband out to 10 GeV. To insure the applicability of the method over the additional range, QCD tracking isolation was plotted for all of our significant backgrounds. The result for the $\mu\tau_h$ channel is shown in Figure 8.2. A similar result was obtained for the $e\tau_h$ channel.

Tracking isolation I_{track} is defined as

$$I_{track} = \sum_{\Delta R<0.4} p_T \tag{8.3}$$

or the sum of p_T over all tracks in a cone of less than $\Delta R < 0.4$.

The plot shows the distribution of the electron track isolation in data for events with 1-prong and 3-prong tau candidates. The data points are for events with an OS (opposite electromagnetic charge) lepton and hadronic tau pair while the histogram (yellow for color displays) indicates events with a LS (like electromagnetic charge) lepton and hadronic tau pair. The LS events in Figure 8.1a are primarily QCD background with some $\gamma + jets$ contribution especially for lower values of tracking isolation. We then try to enhance the LS QCD contribution in the plot by requiring $M_t < 10$ GeV and $10 < E_T^{(ele)} < 20$ GeV, to remove $\gamma + jets$. The distribution is indeed uniform.

The ratio of QCD in the range $0 < I_{track} < 2$ to $2 < I_{track} < 10$ or R_{2to10} is calculated. QCD from data outside the signal region is multiplied by R_{2to10} to get an indication of the magnitude of QCD in the signal region.

The data sample used to perform QCD studies was the same one as used for the $VLQ3$ analysis. Events underwent the same selection criteria as signal events with the following exceptions. The OS event level requirement was not applied and the cut on $N_{prongs} = 1$ or 3 for taus was changed to $N_{prongs} > 4$.

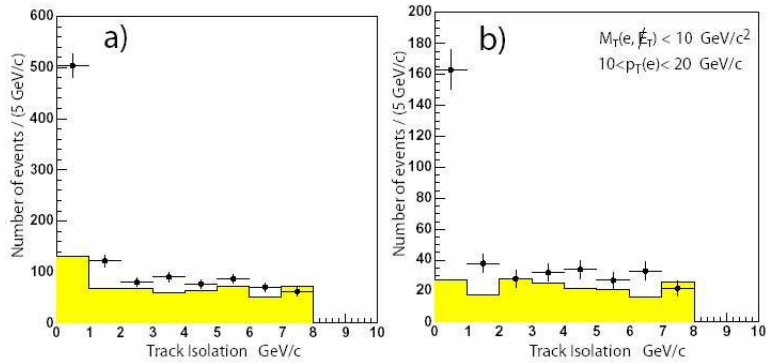

Figure 8.1: a) Electron track isolation in data for 1-prong and 3-prong candidates. The data points are for OS $e\tau_h$ pairs. The yellow shaded histogram is for LS. The LS events are dominated by QCD backgrounds with a $\gamma + jets$ contribution. b) further singles out the QCD background by adding two requirements $M_T < 10$ GeV and $10 < E_T(ele) < 20$ GeV to remove the $\gamma + jets$ leaving only the QCD in the LS histogram. The distribution is truncated at $I_{track} = 8$.

These steps were taken to enhance the QCD component and thus reducing the statistical uncertainty.

8.7 $\gamma + jets$

Photons with three or more suitable jets can fake the $VLQ3$ signal through photon conversions faking an electron. One of the remaining jets fakes a hadronic tau and the remaining two satisfy the $N_{jets} \geq 2$ requirement.

We take the LS events (signal events are OS) with $0 < I_{track} < 2$ not attributed to QCD as $N_{\gamma+jets}$ or conversions from $\gamma + jets$. The number of LS and OS conversions, N_{conv}, or events which pass a check for the presence of a conversion is then counted in each of the control regions. The ratio $N_{\gamma+jets}/N_{conv}$ is used as a scale the number of tagged conversions in each region to determine the contribution from this background. The $N_{\gamma+jets}$ study was conducted using the $VLQ3$ dataset. A detailed summary of background samples is given in Table 8.3.

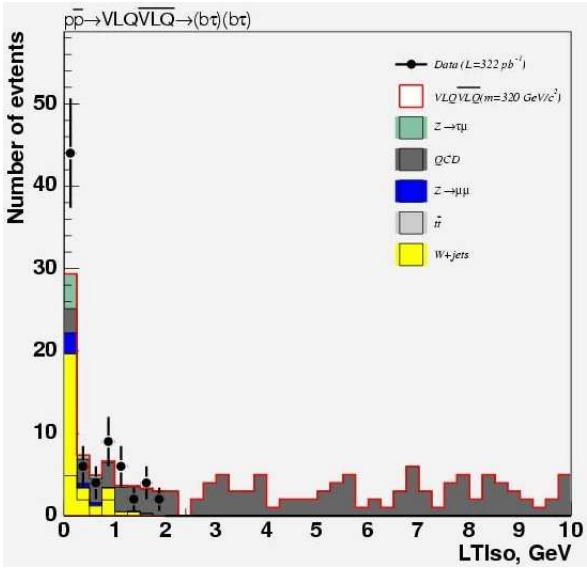

Figure 8.2: I_{track} distributions shown for backgrounds shown for the $\mu\tau_h$ channel. Our sideband method of scaling QCD backgrounds for tracking isolation less than 2 GeV, uses a range larger than in the study for which the method was created. It is necessary to show that QCD remains the dominant background for I_{track} greater than 2 GeV and that the distribution is still uniform over the whole range out to 10 GeV.

Process	Dataset ID	release	# events	cross section	normalization
$Z^0/\gamma^* \to \tau\tau$	zewk8t	5.3.3_EWK	7,598,445	$1.95 \times 255pb$	0.0192
$Z^0/\gamma^* \to \epsilon^+e^-$	zewk6d	5.3.3_EWK	2,879,005	$1.95 \times 255pb$	0.0556
$Z^0/\gamma^* \to \mu\mu$	zewk6m	5.3.3_EWK	3,050,971	$1.96 \times 255pb$	0.0362
$W + \text{jets}\,(W \to e\nu)$	wewkfe	5.3.2_EWK	5,366,615	$2687pb$	0.161
$W + \text{jets}\,(W \to \mu\nu)$	wewk6m	5.3.3_EWK	3,114,127	$2687pb$	0.237
$W + \text{jets}\,(W \to \tau\nu)$	wewk9t	5.3.3_EWK	8,709,395	$2687pb$	0.485
WW	wtop1w	5.3.3	373,511	$11pb$	0.00950
$t\bar{t}$	ttop0z	5.3.3	208,335	$6.7pb$	0.0104
QCD	etlp0d	5.3.1			0.25
$\gamma + \text{jets}$	etlp0d	5.3.1			0.09

Table 8.3: Summary of the background samples. Except for the QCD and $\gamma + \text{jets}$ which are data-based, all of these use the PYTHIA MC generator. In the cases where there is a factor multiplying the cross section, it is due to the ratio of the full mass range to the limited mass range in which the production was done. For QCD and $\gamma + \text{jets}$ the entry under normalization is a scale factor.

Chapter 9

Event Level Selection

Enhancing the sensitivity of the analysis dataset is the aim of event level selections discussed in this chapter. Selection criteria exist which address both the geometric limitations of the detector, see Section 7.2 and the quality of the particle candidate reconstruction, see Section 7.4. After all of the acceptance and ID criteria are imposed there are very few fake particle candidates. Still, as detailed in Chapter 8 the dataset contains events with other physics processes or backgrounds, some fraction of which can be confused with $VLQ3$ pair production. The relative magnitudes of the various backgrounds shown in Figure 4.25 to our $VLQ3$ signal such that even if a given process only has a fraction of events which imitate our signal, that process can still overwhelm our signal. Event level selections are applied in the order listed. All efficiencies are listed in Table 9.1 and are evaluated for $VLQ3$ signal MC ($m_{VLQ3} = 320$ GeV/c^2).

9.1 Opposite Sign

The hadronic tau candidate and leptonic tau candidate are required to have opposite charge. The charge is determined by the curvature of the tracks in the COT and the specific requirement is $Q_\tau \times Q_{lep} = -1$.

9.2 Conversion Removal

Applied only to the $e\tau_h$ channel, this cut is intended to veto events in which the leading electron candidate is consistent with $\gamma \rightarrow e^+e^-$. A collection of conversion tracks are created during event initialization. Track quality is checked (3×3) as detailed in the electron ID Section 7.4.2. However, here only a single segment per superlayer is required. Tracks passing these requirements are checked pair wise against the requirements listed below. A pair of tracks passing these requirements are labeled conversion tracks and are entered into an array for later use. Not every event produces a set of conversion tracks. During conversion removal the track associated with the leading electron candidate is checked to make sure it is not on this list. If a match is found the entire event is vetoed.

The criteria used to assemble the conversion tracks list are:

- $|\Delta\theta_{COT}| \leq 0.4$
- $\Delta S_{xy} \leq 0.2$

Where θ_{COT} is the polar angle in the COT between the two tracks under consideration. S_{xy} is the distance between the two tracks at their closest point of approach. This closest point is calculated as $\sqrt{\Delta x^2 + \Delta y^2} - r_1 - r_2$, where r_i is the radius of curvature of track i to account for the track helicity. The specific criteria for conversion removal are from one of the standard sets used within

CDF. This particular set originates in [72] from concepts developed in CDF Run I [73].

Rather than use the standard conversion removal module from CDF software the same requirements are implemented in a slightly more complex algorithm in order to maintain compatibility with the R-parity violating top squark (RPV Stop) analysis [26] used to set limits on the 3rd generation Scalar leptoquark.

9.3 Cosmic Removal

Cosmic ray removal is applied only to the $\mu\tau_h$ channel. Sometimes, cosmic rays pass through and leave a track in the detector. This gives rise to an event topology resembling either a single muon candidate or a paired muon and 1-prong tau candidates. In order for a cosmic ray to fake our signature a cosmic ray event would need to pass both the acceptance and ID selection requirements and coincide with some jet activity. This is expected to be a small effect and in fact 100% of events remaining in the data stream pass the cosmic veto. We use the standard definition of cosmic rays implemented in *CosmicRayFinderModule*. Removal is implemented with a bit check against the cosmic bank created during production.

9.4 Z Mass Window Removal

Typically termed in other descriptions as "Drell-Yan Removal" this cut does not strictly speaking remove Drell-Yan backgrounds. This selection vetoes events which are consistent with a Drell-Yan process AND which lie with in the Z mass window, $76 < M(obj, e) < 106$ GeV/c^2. This cut is applied to both the $e\tau_h$ and

the $\mu\tau_h$ channels.

Events containing the process $Z \rightarrow e^+e^-$ are removed by calculating the invariant mass of the electron candidate with two separate classes of objects, hadronic tau candidates and CdfEmObjects. A tau candidate which passes the ID cuts and have an xy separation of from the electron candidate of $\Delta\phi(\tau, e) > 2.9$ are considered. A CdfEMObject passing $E_T^{corr} > 8$ GeV, and the $Had/Em < 0.12$ are also considered. Each is paired with the electron candidate and if the invariant mass falls within the mass window, $76 < M(obj, e) < 106$ GeV/c^2 the event is vetoed.

Events containing the process $Z \rightarrow \mu^+\mu^-$ are removed by checking the muon candidate against all tracks which pass the following. The track must match a muon stub, possess $p_T > 10$ GeV/c and has $|z_0^{trk} - z_0^{\mu}| < 5$ cm. If the invariant mass of the muon candidate and track falls within the mass window, $76 < M(obj, e) < 106$ GeV/c^2 the event is vetoed.

9.5 $\not\!\!E_T$ and $\not\!\!E_T$ Corrections

Events with $\not\!\!E_T^{corr}$ less than 10 GeV is are vetoed. Here $\not\!\!E_T^{corr}$ is adjusted for the presence of muons, electrons, jets and tau candidates in the event. The algorithm used to adjust $\not\!\!E_T^{raw}$ is discussed below.

The $\not\!\!E_T^{corr}$ requirement helps to suppress backgrounds such as $Z^0 \rightarrow \tau^+\tau^-$ and QCD that appear in the control regions but do not appear in the signal region. However, the cut preserves backgrounds which do appear in both regions. Also validation studies are assisted with this requirement.

During the validation stage of this analysis we ran into a very specific background not modeled by our current MC simulation. The events in question came

into view when some of the selection criteria for the hadronic tau candidates were loosened. Specifically, hadronic tau candidates which pass all acceptance and ID criteria except the $N_{prongs} = 1$ or 3 showed an unexplained excess for 1 or 2 jets. It was noted that the events fell off with increasing H_T (defined later in this chapter) and were entirely absent for higher values of the same parameter. The jet multiplicity, $N_{jets} \geq 2$, requirement also eliminates these events as of course, does a return to the $N_{prongs} = 1$ or 3 back in the tau ID stage. Therefore, while interesting for their own sakes these "two prong taus" are were judged to be irrelevant to our analysis. The addition of a $\not\!\!E_T^{corr} > 10$ GeV entirely eliminates this class of events even with the loosened criteria and was therefore included in the event level selections as an additional method of suppressing this background.

The raw missing transverse energy $\not\!\!E_T^{raw}$ is calculated for each event. The vector sum of all of the energy deposits in the calorimeters is calculated and the raw $\not\!\!E_T$ is simply the deficit of energy in the transverse plane. This $\not\!\!E_T$ is attributed to particles with little (muons) or no (neutrinos) interactions in the calorimeter as well as to gaps in calorimeter acceptance. There are however pieces of event information which can be used to arrive at a better estimate of the energy escaping detection. These corrections are for muon, electron, and jet candidates. The last correction to take place is for a change in the reconstruction of the tau candidates. In all cases the $\not\!\!E_{T\ i}$ $(i = x, y)$ in each of the equations below refers to the cumulative corrected value. The $\not\!\!E_{T\ i}$ in Equation 9.3 has already been corrected for either a muon candidate, Equation 9.1 or for an electron candidate, Equation 9.2.

In the $\mu\tau_h$ channel the transverse energy of the leading muon candidate is calculated and subtracted from $\not\!\!E_T^{\ raw}$. Unlike neutrinos, muons do deposit a small amount of energy in the calorimeters. Once the muon energy is subtracted

off this small contribution has to be added back in. The entire correction is summarized as follows:

$$\not{E}_{T\ i} = \not{E}_{T\ i} - p_i^{(\mu)} \left(1 - \frac{E_{HAD} + E_{EM}}{p}\right) \tag{9.1}$$

where the subscript i stands for the x and y components of the relevant quantities and p stands for the magnitude of the muon momentum.

In the $e\tau_h$ channel a correction is now applied for a transverse energy correction of the primary electron candidate.

$$\not{E}_{T\ i} = \not{E}_{T\ i} - p_i(ele)\,({f_T}^{corr}(ele) - 1) \tag{9.2}$$

where $f_T^{e\,corr}$ is a multiplicative factor used to arrive at $E_T^{corr}(ele) = f_T^{e\,corr} \times E_T^{raw}(ele)$. This is the same $E_T^{corr}(ele)$ used in the electron candidate acceptance.

The jet correction to $\not{E}_T$ takes the form:

$$\not{E}_{T\ i} = \not{E}_{T\ i} - \sum_{jets} p_i(jet)\,({f_T}^{corr}(jet) - 1) \tag{9.3}$$

Where the sum over jets refers to the collection of jets satisfying the requirements of Section 7.4.1. It should be noted that the $\not{E}_T$ is not being corrected for the electron twice. The jet primitive associated with the electron candidate is not present in the jet collection summed over. That collection of jets was assembled using a separation requirement from the lepton candidate. The factor ${f_T}^{corr}(jet)$ is the level 5 jet energy correction factor.

Lastly, there is an $\not{E}_T$ correction due to the tau reconstruction. The default tau reconstruction method, which plays into the calculation of $\not{E}_T^{raw}$ differs from the method used in the analysis. Default taus have a $E_T > 1$ GeV tower energy

threshold. The method used in this analysis is to include neighboring towers below threshold in order to account for the energy deposits which leak across tower boundaries. The correction uses only the primary hadronic tau candidate.

$$\not{E}_{T\ i} = \not{E}_{T\ i} - \left(p_i^{(\tau)}(\text{visible}) - p_i^{(\tau)}(\text{expanded cluster})\right) \tag{9.4}$$

9.6 Control Regions

Control regions are established as part of the "blind analysis" strategy. The event parameter space is divided into control regions in which we can examine data and background samples from data closely without fear of biasing the analysis with foreknowledge of what lies in the expected signal region of the parameter space.

The $VLQ3$ event parameter space is divided in to 5 regions, Figure 9.1. The control regions are labeled CRXJ, where $X = 0, 1$ or 2 jets. CR0J and CR1J lie entirely outside the signal parameter space. The portion of the parameter space with $N_{jets} \geq 2$ is further divided into a control region CR2J from $0 < H_T \leq 160$ GeV. The upper H_T boundary on CR2J corresponds to the H_T value that would result from a $VLQ3$ at the previous mass limit on the $VLQ3$. The SAFE region also within $N_{jets} \geq 2$ extends from $160 < H_T \leq 400$ GeV. The upper limit on the SAFE region corresponds to the optimized H_T cut value of 400 GeV. Lastly we have the signal region which is intended to remain unexamined or "blinded" until it can be demonstrated that all backgrounds are under control in the other regions.

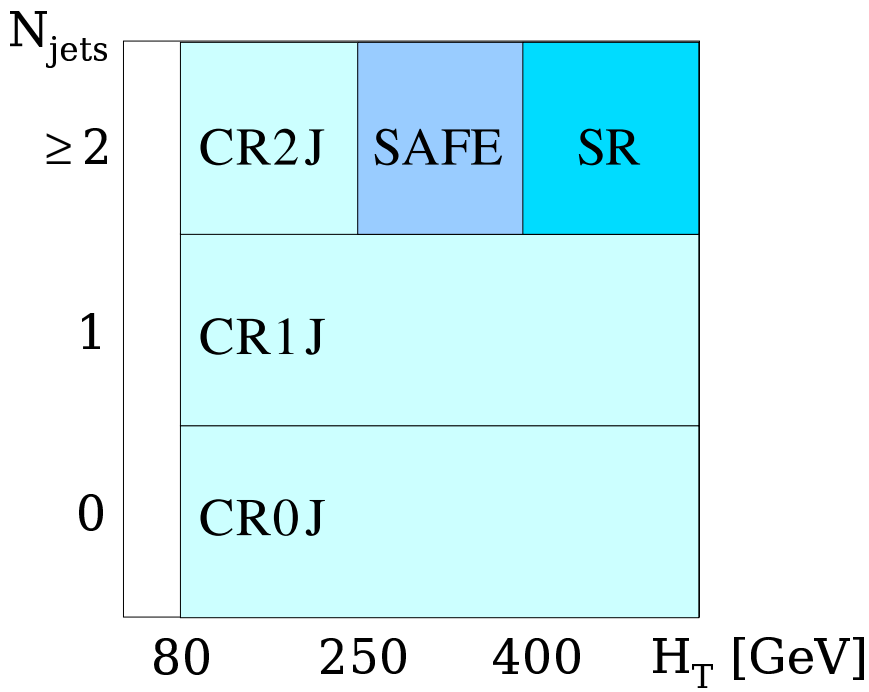

Figure 9.1: The $VLQ3$ event parameter space is divided in to 5 regions based on the number of jets and the kinematic variable H_T.

9.7 H_T Cut

The primary kinematic cut used for background suppression is called H_T. H_T is the sum over all available transverse energies,

$$H_T = E_T^{(lep)} + E_T^{(\tau_h)} + \not{E}_T^{corr} + E_T^{(jet_1)} + E_T^{(jet_2)}. \tag{9.5}$$

Here the $E_T^{(lep)}$ is replaced by p_T for the $\mu\tau_h$ channel. The two jet E_T refer to the two highest E_T jets which pass the requirements of Section 7.4.1.

Figure 9.2 shows the H_T distribution for $VLQ3$ MC ($m_{VLQ3} = 320$ GeV) and backgrounds. The distribution has imposed upon it an additional requirement of $N_{jets} \geq 2$. Both signal and backgrounds are displayed separately for the $e\tau_h$ and $\mu\tau_h$ channels. Figure 9.3 shows an unscaled version of the significance vs

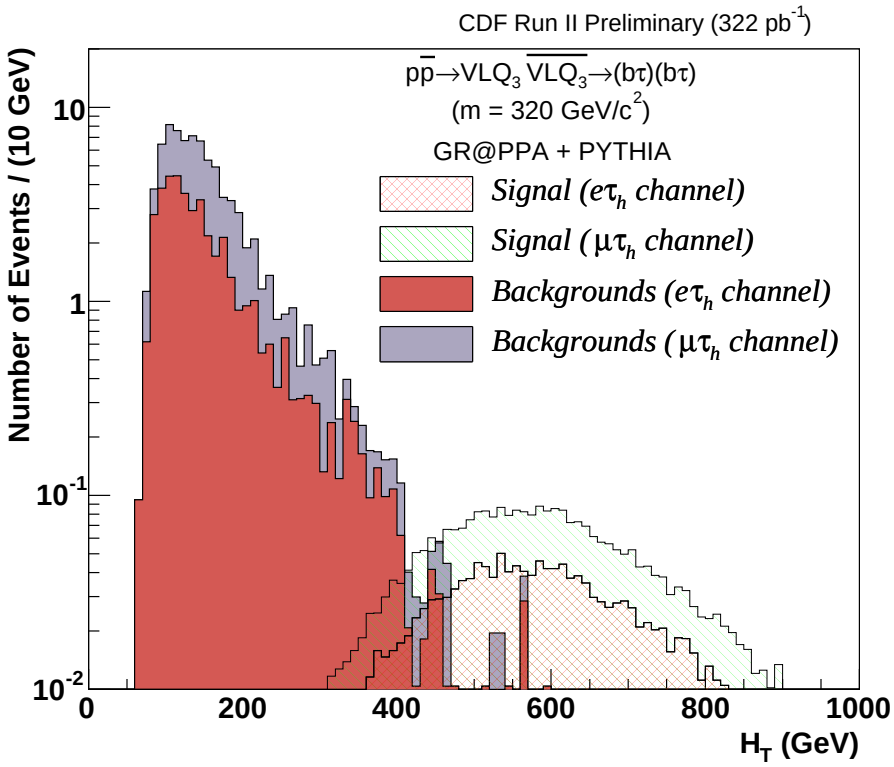

Figure 9.2: Stacked H_T distribution for 320 GeV$/c^2$ $VLQ3$ signal MC and background, both $e\tau_h$ and $\mu\tau_h$ channels are displayed separately. An additional requirement of $N_{jets} \geq 2$ is imposed on this distribution.

H_T. The optimized value of the H_T cut can be read off the plot as $H_T > 400$ GeV. It should also be noted that the maximum significance is to be found in a relatively flat portion of the curve. This means that the efficiency of this cut and the sensitivity of the analysis is not greatly affected by small variations around the selected H_T cut. The optimum H_T cut is mass dependent and is optimized for 320 GeV $VLQ3$. However, the analysis remains sensitive down to $m_{VLQ3} = 200$ GeV/c^2. The use of the H_T kinematic variable is the largest difference between this analysis and the R-parity violating top squark (RPV Stop) analysis [23] which used the variable Y_T. The quantity Y_T is defined as,

$$Y_T = p_T(\mu) + p_T(\tau_h) + \not{E}_T \quad . \tag{9.6}$$

For the electron channel the $p_T(\mu)$ is replaced by $E_T(electron)$. The change in choice of change in kinematic variable is motivated by the heavier $VLQ3$ which should produce relatively stiffer jets. In fact the significance of the H_T cut peaks at 1.23 for a value 400 GeV, where Y_T peaks at 1.12 at a cut value of $Y_T \geq 200$ GeV. We chose the cut with the higher significance. After this cut, the largest surviving background is $t\bar{t}$.

While background contributions to this analysis do not use extrapolated distributions (we use counting or Poisson Statistics) we investigated the effect that an exponential tail in H_T distribution for backgrounds would have on the analysis. The question arose in part because the low statistics in the region near the chosen H_T cut value ($H_T < 400$ GeV) see Figure 9.2. An exponential fit to the H_T distribution for both $e\tau_h$ and $\mu\tau_h$ are shown in Figures 9.4 and 9.5. The integral in the signal region is 0.42 events for $e\tau_h$ and 0.43 events for $\mu\tau_h$ respectively. These values are stable in that reasonable changes in the fit result in only small

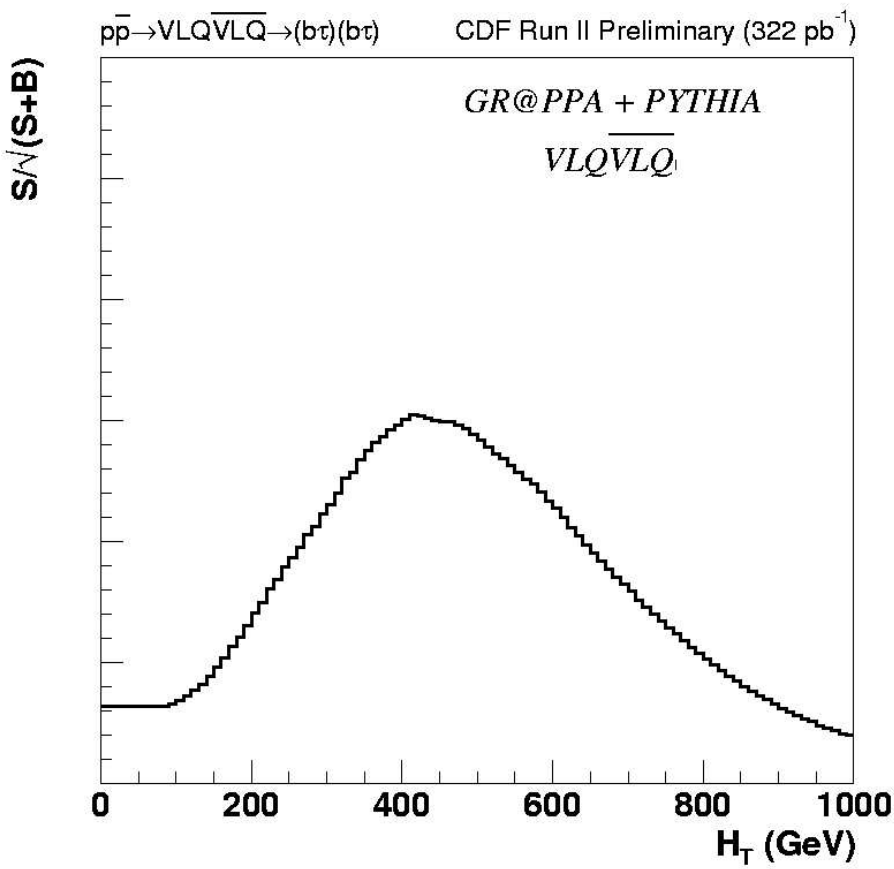

Figure 9.3: Significance variable $S/\sqrt{S+B}$ plotted against H_T cut showing a maximum at 400 GeV. The distribution is relatively flat showing that the analysis is not terribly sensitive to small variations around $H_T > 400$ GeV.

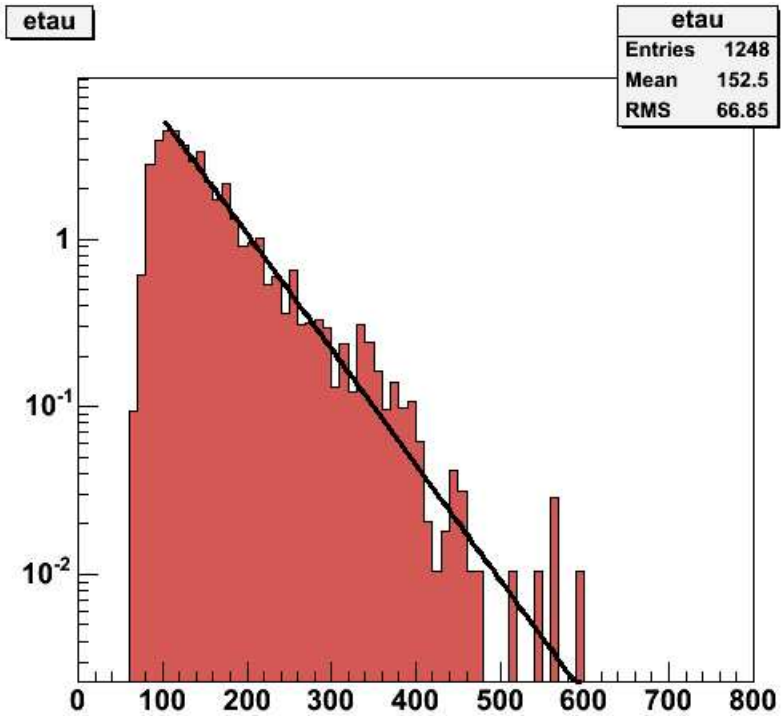

Figure 9.4: Low statistics in the background near the chosen H_T cut value inspired a study to estimate of the background contributions in the region $400 \leq H_T \leq 600$ GeVfor the $\tau_e\tau_h$ channel.

changes in the integrals. Compare this to the $e\tau_h$ channel the total background prediction is 0.25 +0.21/-0.06 (stat) +/- 0.05 (syst). In the $\mu\tau_h$ channel the total background prediction is 0.24 +0.22/-0.05 (stat) +/- 0.05 (syst). Even if the lack of statistics is obscuring an exponential tail in H_T for backgrounds the statistical uncertainty covers the amount of background.

9.8 Jet Multiplicity

The final event selection cut is on the number of jets. These jets are from the collection discussed in Section 7.4.1. We require at least two jets in an event, $N_{jets} \geq 2$.

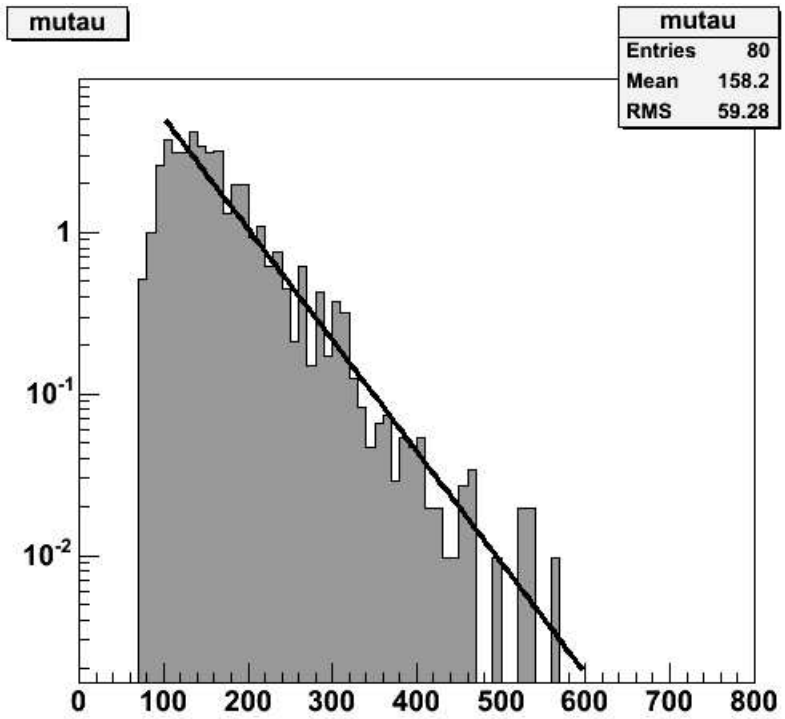

Figure 9.5: Low statistics in the background near the chosen H_T cut value inspired a study to estimate of the background contributions in the region $400 \leq H_T \leq 600$ GeVfor the $\tau_\mu \tau_h$ channel.

Requirement	$e\tau_h$ Efficiency (%)	$\mu_{CMUP}\tau_h$ Efficiency (%)	$\mu_{CMX}\tau_h$ Efficiency (%)
ℓ acceptance	46.3 ± 0.2	28.4 ± 0.1	9.1 ± 0.1
$\tau_{\rm h}$ acceptance	56.0 ± 0.2	56.7 ± 0.3	55.6 ± 0.5
$\ell - \tau_{\rm h}$ sep.	96.7 ± 0.1	96.3 ± 0.2	97.4 ± 0.2
Subtotal	$25.1 \pm 0.1 \pm 0.4$	$14.6 \pm 0.1 \pm 0.1$	$4.8 \pm 0.1 \pm 0.0$
$\ell -$ jet sep.	$90.3 \pm 0.2 \pm 0.0$	$88.5 \pm 0.3 \pm 0.0$	$90.8 \pm 0.4 \pm 0.0$
ℓ ID	$82.4 \pm 0.3 \pm 0.8$	$85.2 \pm 0.3 \pm 2.7$	$89.7 \pm 0.4 \pm 0.3$
ℓ iso.	$88.4 \pm 0.2 \pm 2.7$	$94.9 \pm 0.2 \pm 2.8$	$95.4 \pm 0.3 \pm 2.9$
ℓ trigger	$97.0 \pm 0.1 \pm 1.0$	$95.9 \pm 0.2 \pm 1.0$	$95.8 \pm 0.3 \pm 1.0$
$\tau_{\rm h} -$ jet sep.	$93.9 \pm 0.2 \pm 0.0$	$93.9 \pm 0.2 \pm 0.0$	$94.5 \pm 0.4 \pm 0.0$
$\tau_{\rm h}$ ID	$66.1 \pm 0.4 \pm 0.2$	$66.1 \pm 0.5 \pm 0.2$	$67.5 \pm 0.8 \pm 0.2$
$\tau_{\rm h}$ iso.	$79.1 \pm 0.4 \pm 2.4$	$79.2 \pm 0.5 \pm 2.4$	$79.8 \pm 0.8 \pm 2.4$
$\tau_{\rm h}$ trigger	$96.9 \pm 0.2 \pm 1.0$	$97.0 \pm 0.2 \pm 1.0$	$97.6 \pm 0.4 \pm 1.0$
Subtotal	$7.6 \pm 0.1 \pm 3.9$	$5.4 \pm 0.1 \pm 4.8$	$1.8 \pm 0.0 \pm 4.0$
Event level	78.4 ± 0.2	83.9 ± 0.2	83.3 ± 0.4
Grand total	$6.0 \pm 0.1 \pm 3.1$	$4.5 \pm 0.1 \pm 4.0$	$1.5 \pm 0.0 \pm 3.3$

Table 9.1: Summary of all efficiencies, including acceptances, separations, identification, isolations, trigger, and event level requirements. These apply to an $VLQ3$ with Yang-Mills couplings and $m_{VLQ3} = 320$ GeV/c^2.

Requirement	$e\tau_h$ Efficiency (%)	$\mu_{\rm CMUP}\tau_h$ Efficiency (%)	$\mu_{\rm CMX}\tau_h$ Efficiency (%)
Particle Selection	7.52 ± 0.08	5.17 ± 0.07	1.84 ± 0.04
Event Selection	81.73 ± 0.19	87.37 ± 0.25	85.83 ± 0.36
Total	6.14 ± 0.07	4.52 ± 0.07	1.58 ± 0.04

Table 9.2: Summary of efficiencies for $m_{VLQ3} = 360$ GeV/c^2, which is close to the observed mass limit. The row called particle selection is the summary of acceptances, separations, identification, isolations, and trigger efficiencies.

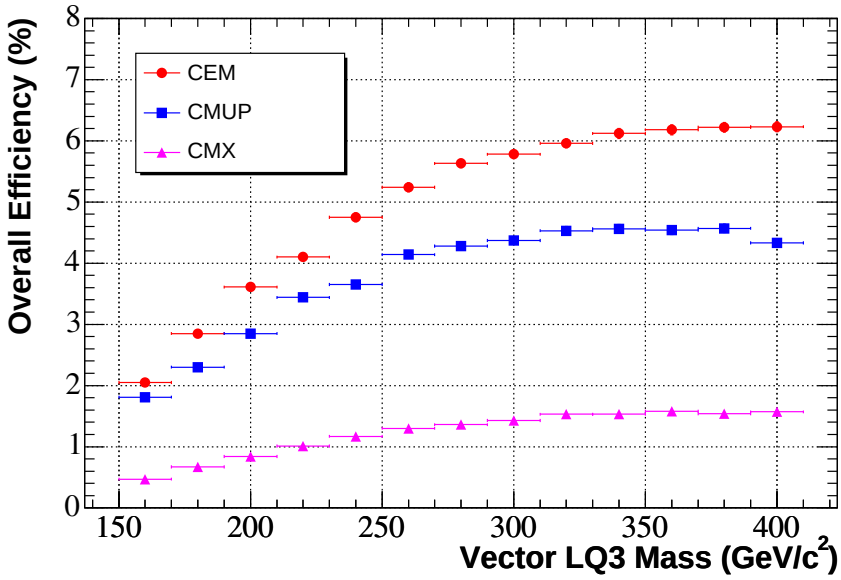

Figure 9.6: Mass dependence for full event selection acceptance is relatively flat in the expected signal region.

9.9 Control Region Checks

Figures 9.7 - 9.21 show a number of kinematic distributions for the control regions defined in Section 9.6. In these plots the distributions for the different trigger channels $e\tau_h$ and $\mu\tau_h$ are displayed in consecutive figures. In most cases, each set of plots CR0J, the zero jet control region, is the left-most plot. CR1J, the one jet control region, is in the center and CR2J, the two jet control region is on the right. The exceptions are the plots concerned with the highest and second highest jet E_T distributions. For the former, CR0J is simply not applicable, while for the latter only CR2J is applicable.

All of the histograms are stacked plots. $VLQ3$ signal MC was added to the distributions in order to test for signal leakage into the control regions. If displayed in color, the $VLQ3$ histogram is white with a red border, with no white

displayed. In all of the plots only the border is visible indicating zero signal MC contribution. In addition the $W + jets$ background, the lowest region displayed (yellow for color displays) is divided into two regions with a gray line. Above the gray line the W decays as $W \rightarrow e\nu$ for the $e\tau_h$ trigger channel and for $W \rightarrow \mu\nu$ for the $\mu\tau_h$ trigger channel. The region below the gray line displays the contribution from W decaying as $W \rightarrow \tau\nu$. Results of all event level cuts are shown for the $e\tau_h$, $\mu_{CMUP}\tau_h$ and $\mu_{CMX}\tau_h$ channels in Table 9.2.

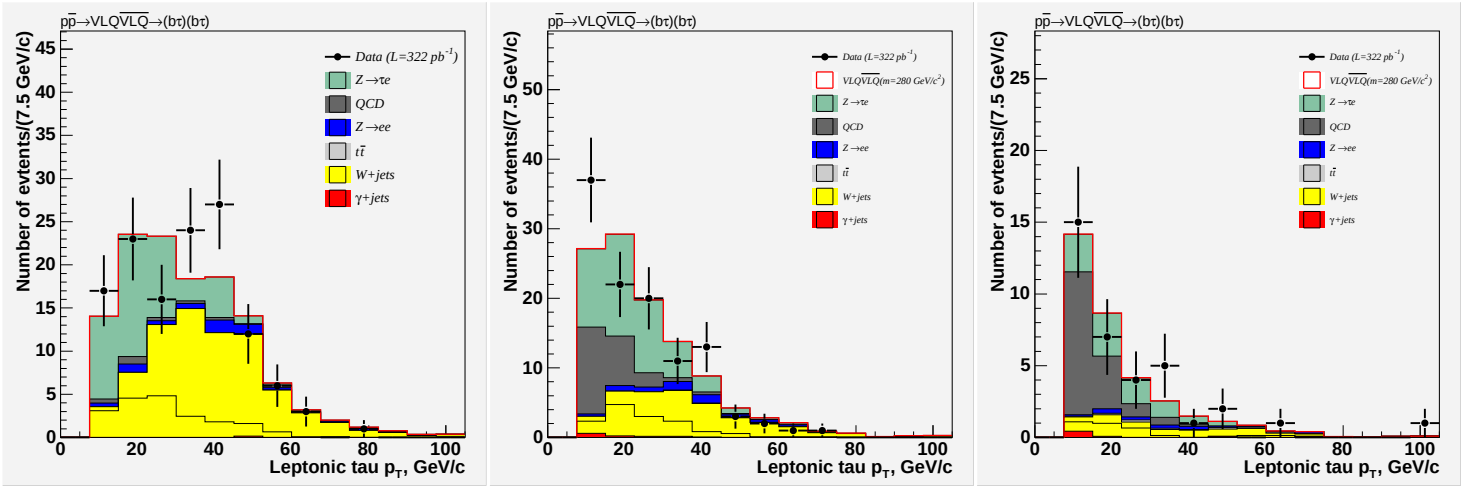

Figure 9.7: Distributions for electron E_T for control regions CR0J (left), CR1J (middle), and CR2J (right).

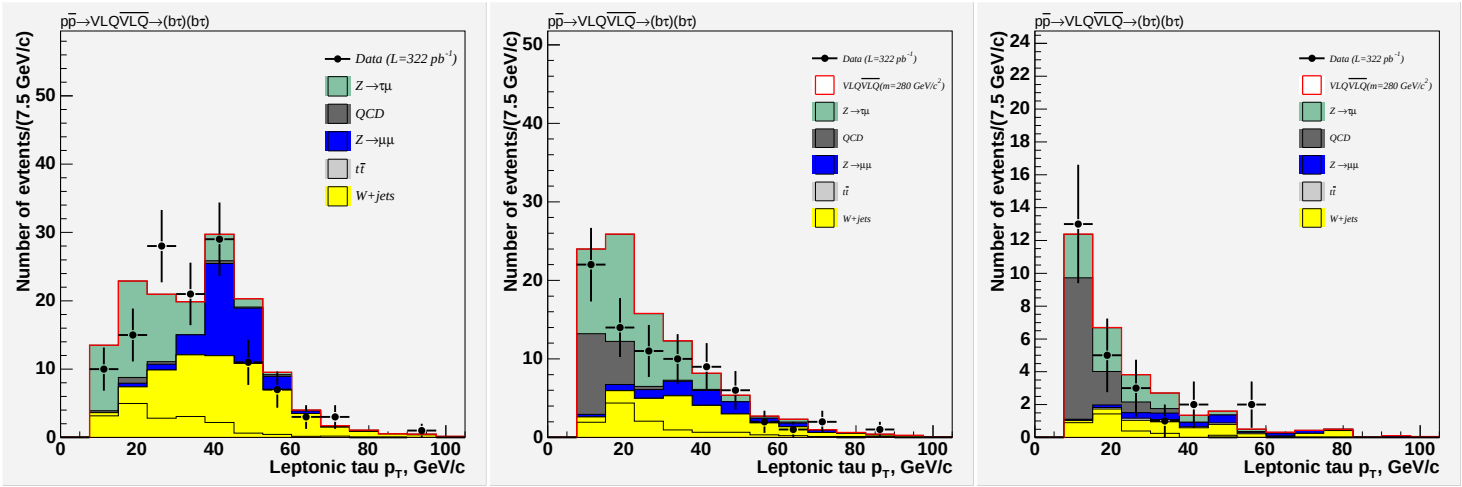

Figure 9.8: Distributions for muon p_T for control regions CR0J (left), CR1J (middle), and CR2J (right).

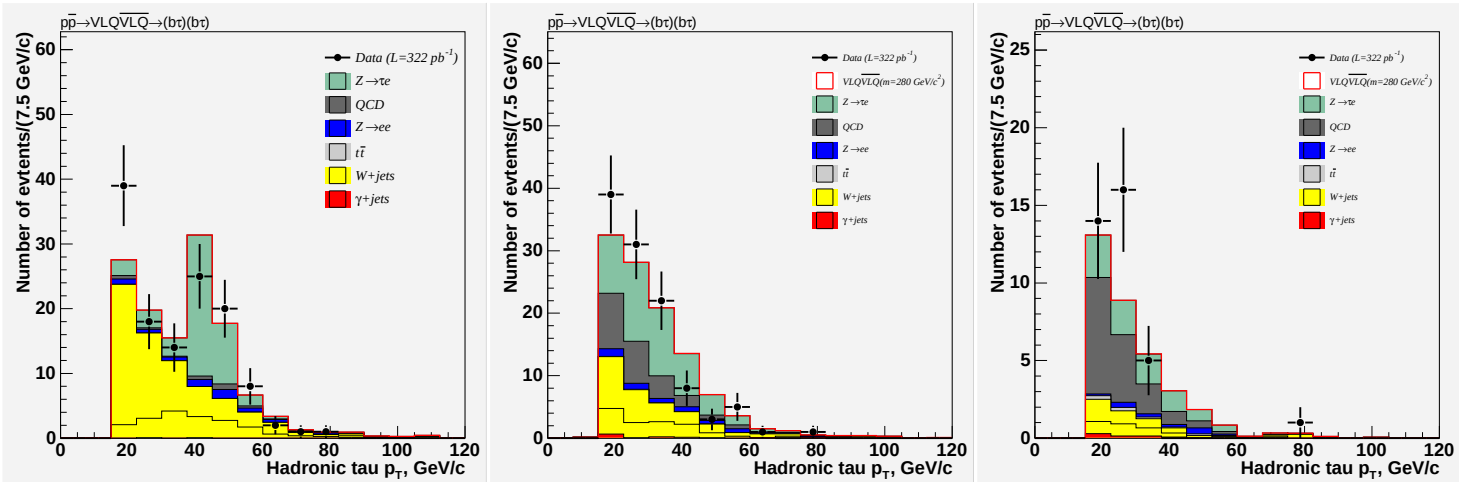

Figure 9.9: Distributions for hadronic tau p_T in the electron channel for control regions CR0J (left), CR1J (middle), and CR2J (right).

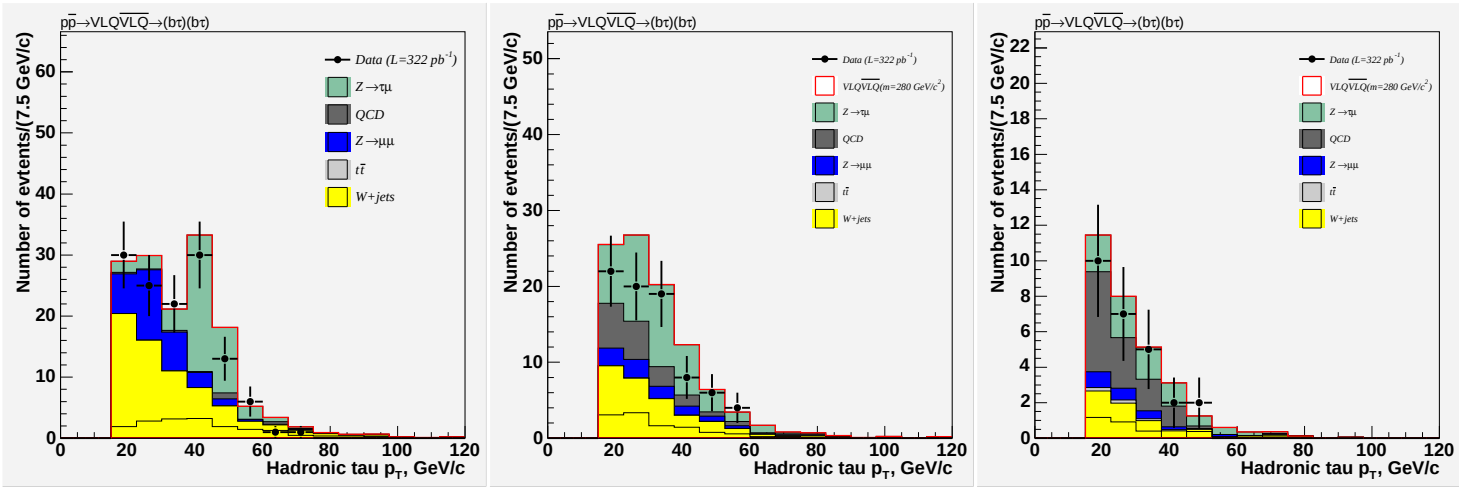

Figure 9.10: Distributions for hadronic tau p_T in the muon channel for control regions CR0J (left), CR1J (middle), and CR2J (right).

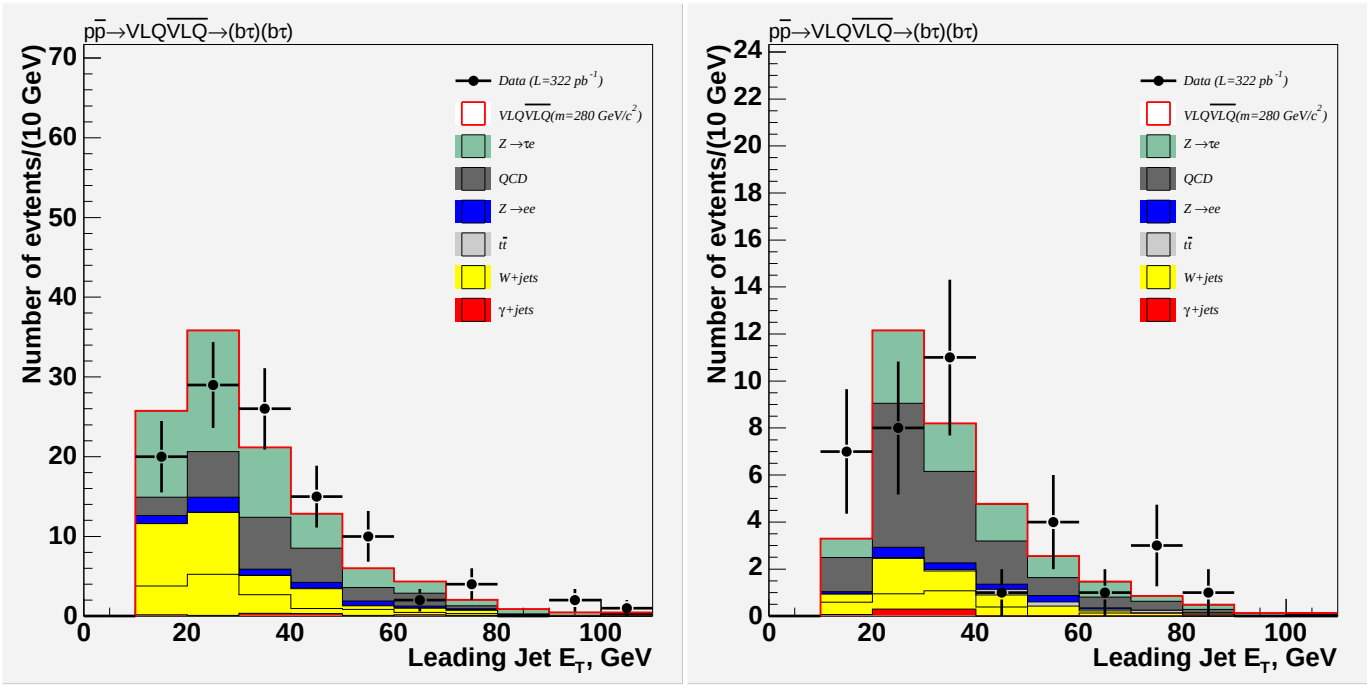

Figure 9.11: Distributions for leading jet E_T in the electron channel for control regions CR1J (left), and CR2J (right).

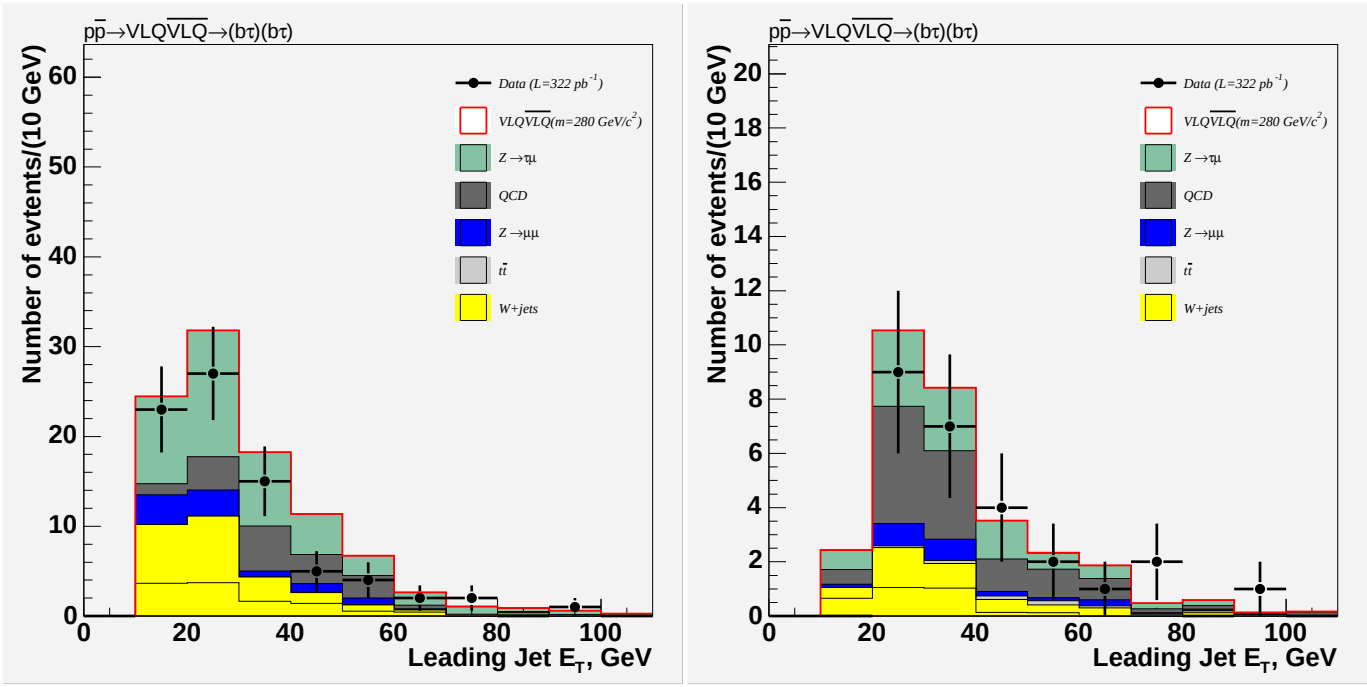

Figure 9.12: Distributions for leading jet E_T in the muon channel for control regions CR1J (left), and CR2J (right).

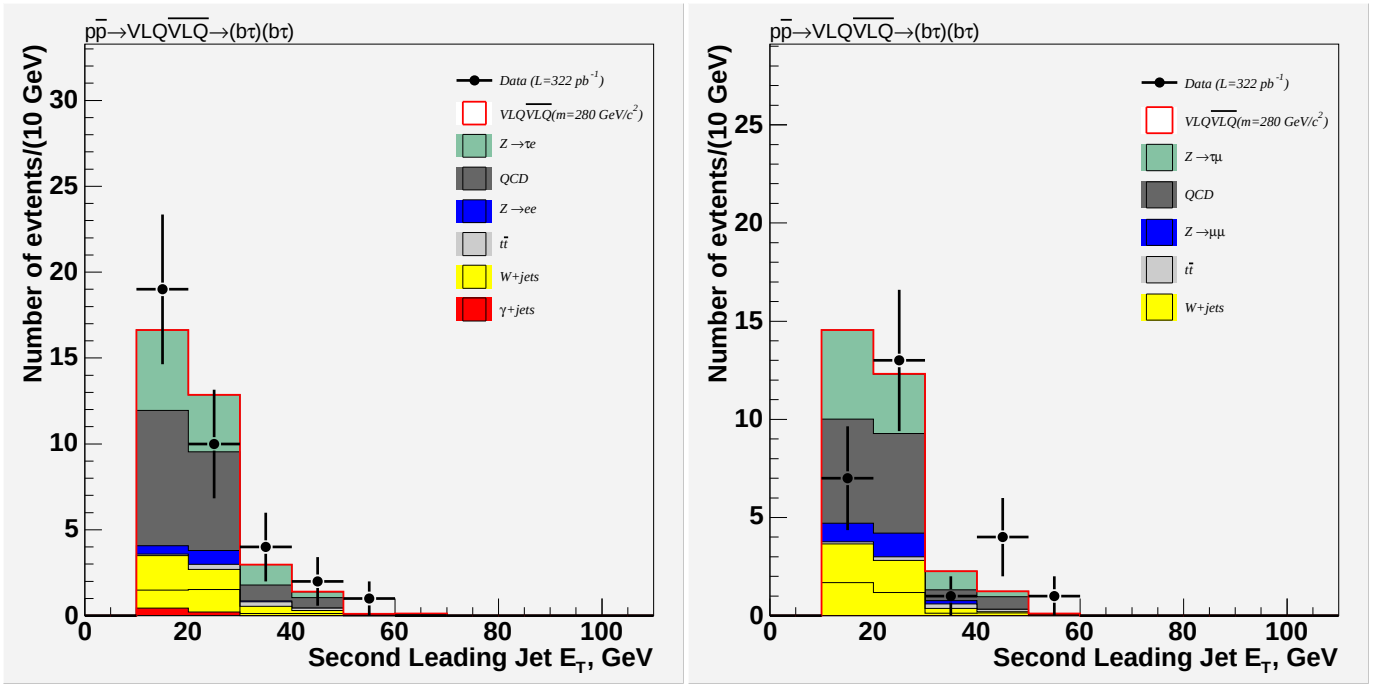

Figure 9.13: Distributions for second most leading jet E_T in the electron channel (left) and muon channel (right) for control region CR2J.

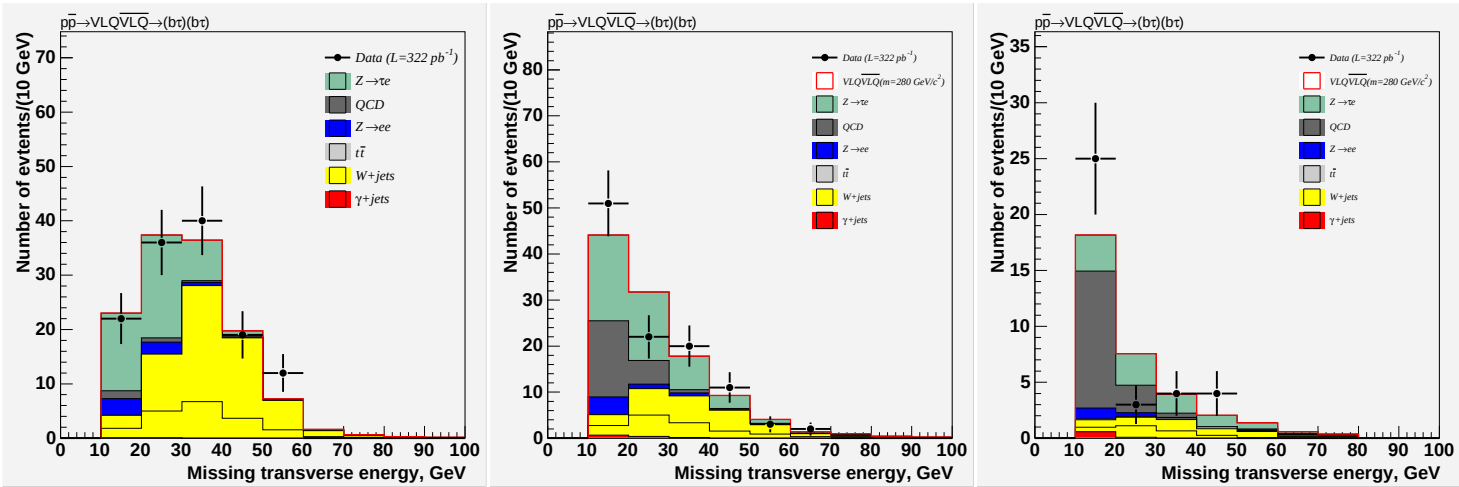

Figure 9.14: Distributions for $\not\!\!E_T$ in the electron channel for control regions CR0J (left), CR1J (middle), and CR2J (right).

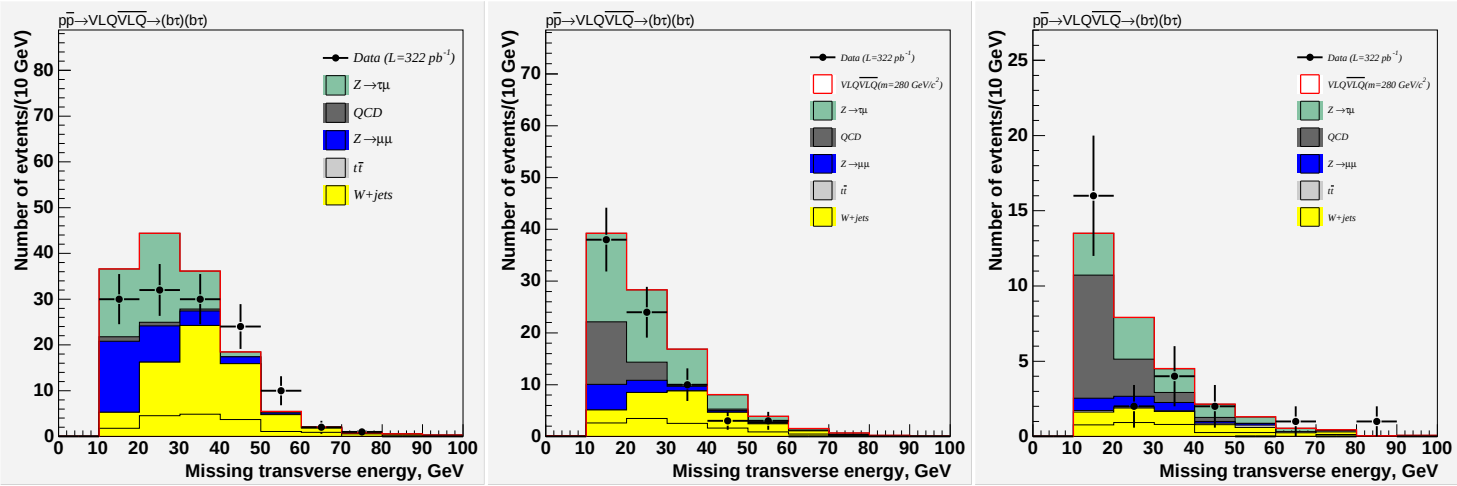

Figure 9.15: Distributions for $\not\!\!E_T$ in the muon channel for control regions CR0J (left), CR1J (middle), and CR2J (right).

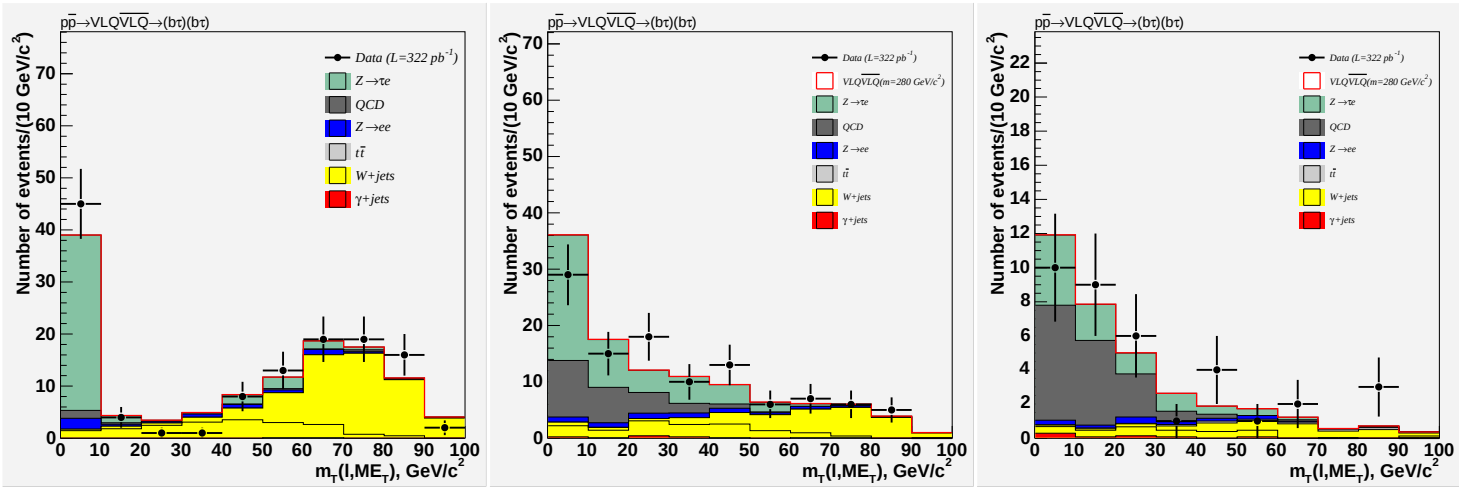

Figure 9.16: Distributions for M_T in the electron channel for control regions CR0J (left), CR1J (middle), and CR2J (right).

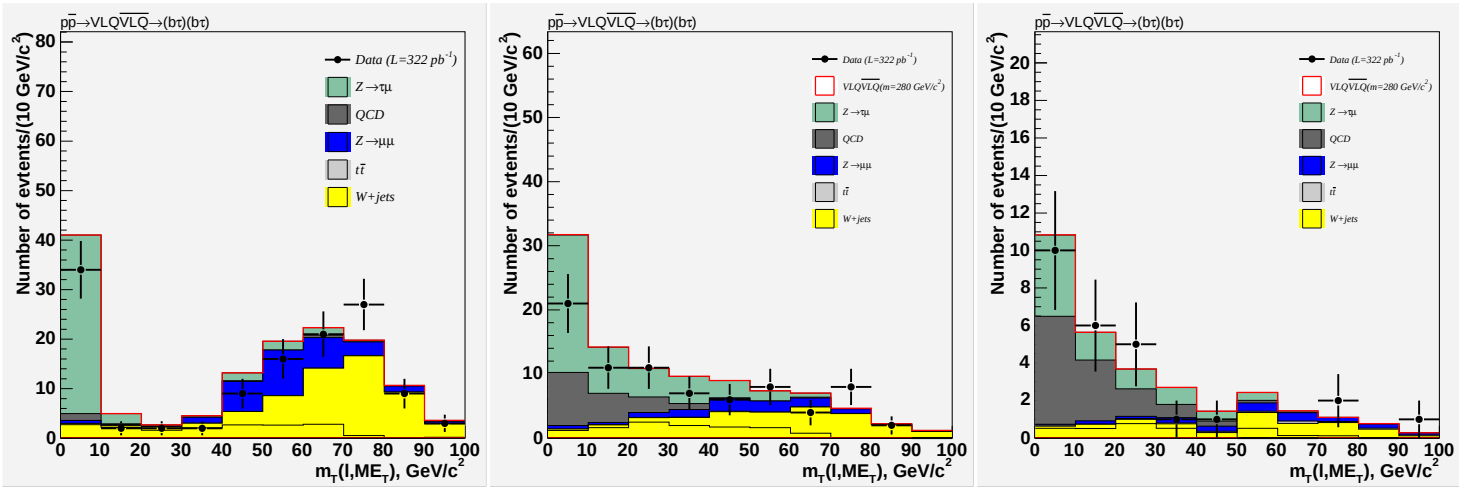

Figure 9.17: Distributions for M_T in the muon channel (bottom row) for control regions CR0J (left), CR1J (middle), and CR2J (right).

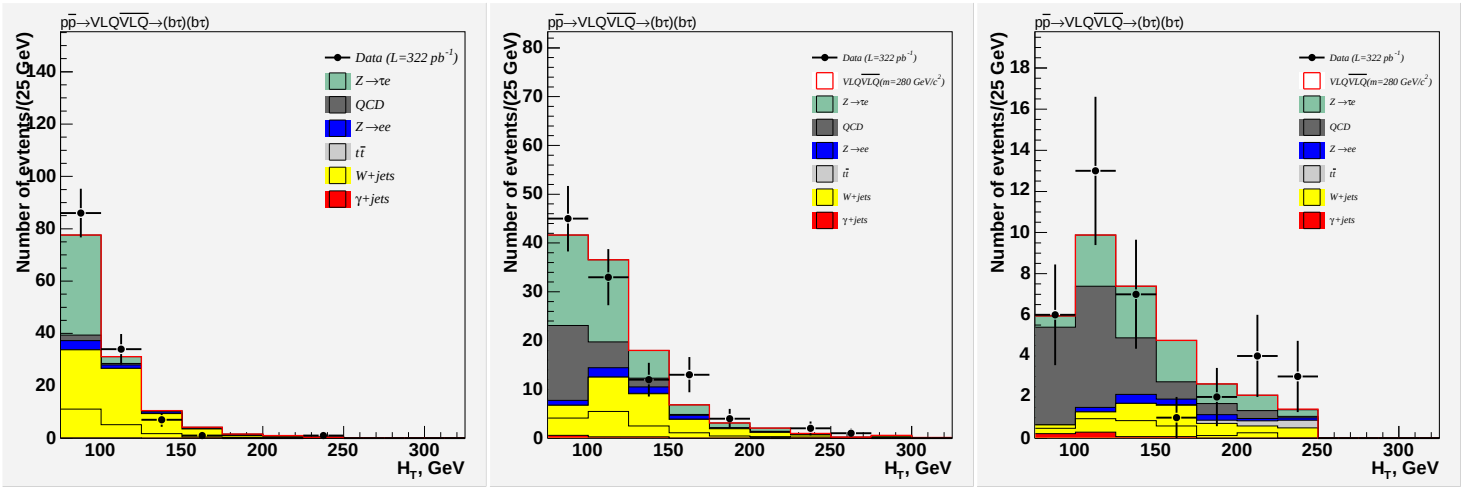

Figure 9.18: Distributions for H_T in the electron channel for control regions CR0J (left), CR1J (middle), and CR2J (right).

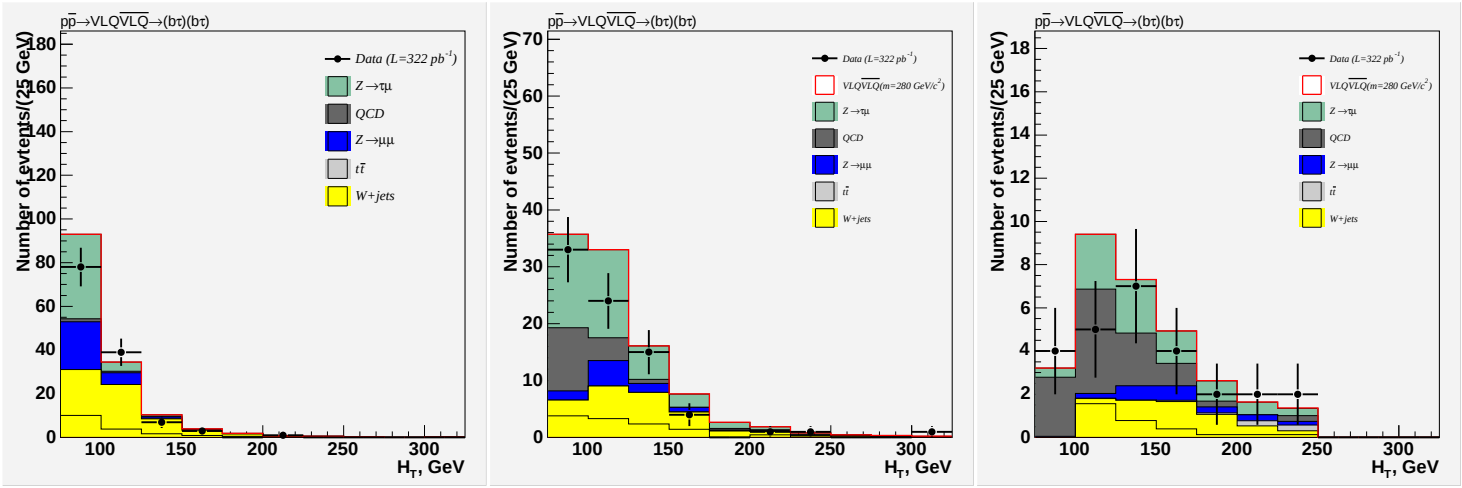

Figure 9.19: Distributions for H_T in the muon channel for control regions CR0J (left), CR1J (middle), and CR2J (right).

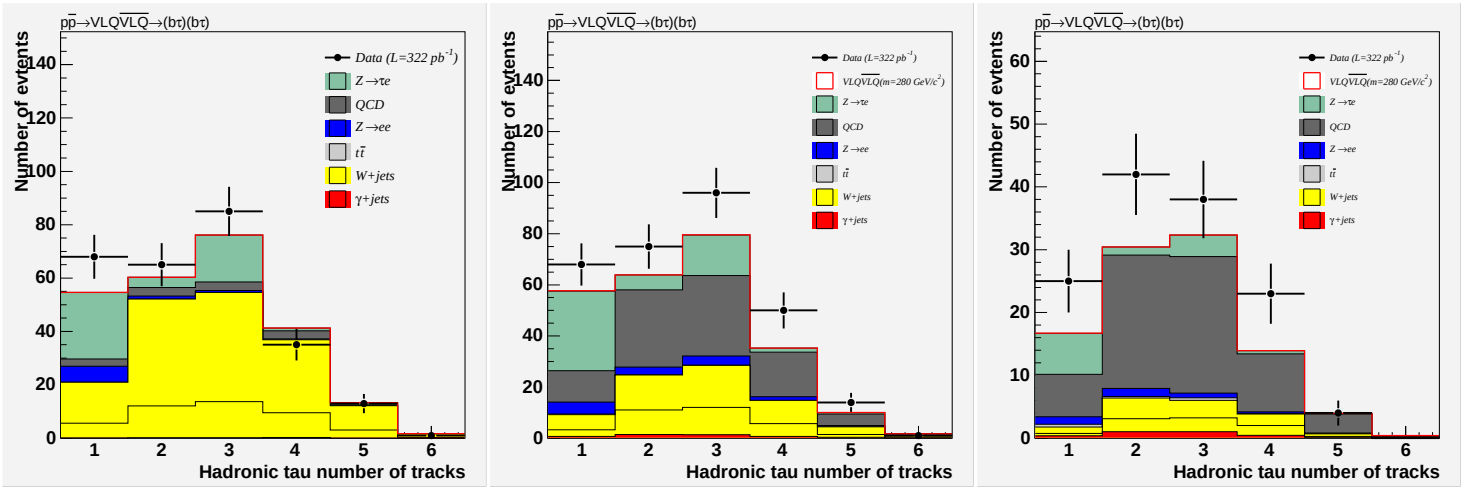

Figure 9.20: Distributions for N_{prongs} of the hadronic tau in the electron channel for control regions CR0J (left), CR1J (middle), and CR2J (right).

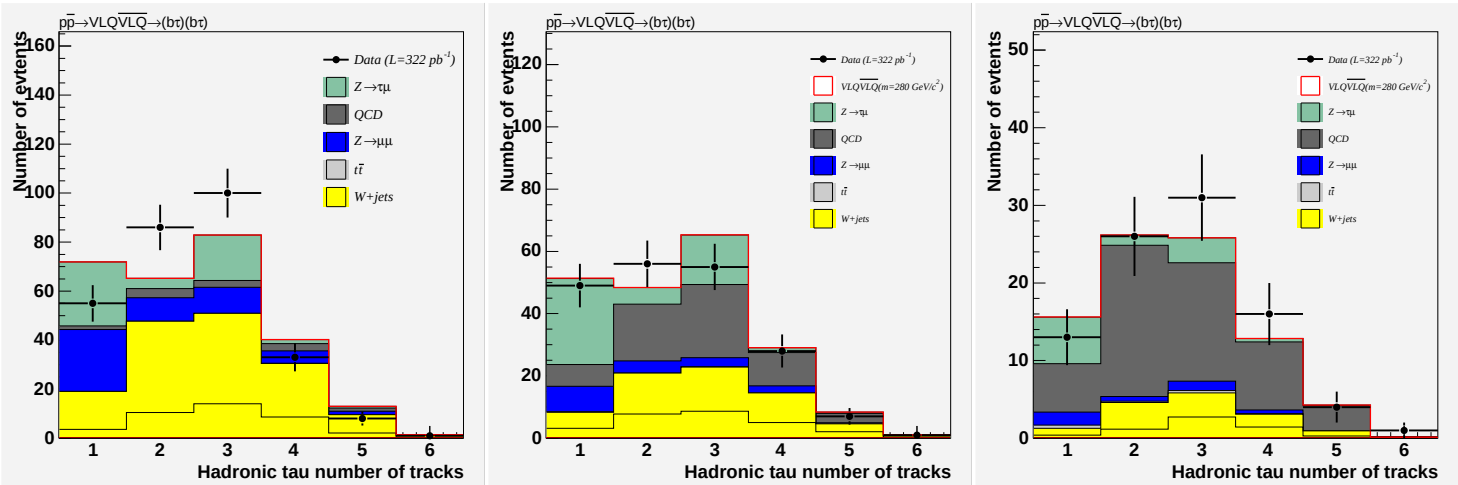

Figure 9.21: Distributions for N_{prongs} of the hadronic tau in the muon channel for control regions CR0J (left), CR1J (middle), and CR2J (right).

Chapter 10

Systematic Uncertainties

Information concerning the systematic uncertainties are aggregated in this chapter. Many of the systematics are derived from the R-parity violating top squark (RPV Stop) analysis [23] or are derived using similar techniques for this analysis.

10.1 Luminosity Measurement

The standard uncertainty of 6.0% is applied to the integrated luminosity [74].

10.2 Production Cross Section

The uncertainty in the $VLQ3$ production cross section is primarily due to the choice of the renormalization scale Q^2 and the Parton Distribution Functions (PDFs). The Q^2 value enters our analysis through the matrix element calculations, the addition of Initial State Radiation (ISR) by PYTHIA and through the momentum of the hard process. The results for both PDF variation and Q^2 choice are shown in Tables 10.1 and 10.2.

An estimate of the systematic uncertainty due to the choice of PDF on the cross section is arrived at by generating GR@PPA event files (which include a summary cross section) with the 40 eigenvalues of *CTEQ6M*. This set of PDFs is generated with small variations up and down its 20 parameters. Each of these is compared to the default cross section generated with *CTEQ5L*. Positive changes to the cross section $\sigma_i - \sigma_{default} > 0$ are considered separately from those changes which result in $\sigma_i - \sigma_{default} < 0$. In the event that the paired eigenvalues both result is a variation of the same sign the average of the two is added to the appropriate set, positive or negative. Both sets of variances are added in quadrature. This is very similar to the weighted event procedure used for estimating the effect of choice of PDF on the analysis is contained in Section 10.3. The difference is that only the change in cross section, rather than total acceptance is considered and of course there is no need to treat the decay channels separately.

The choice of the renormalization scale, $Q^2 = m_{VLQ3}$ is the same as used for previous searches at CDF Run II for leptoquarks in the first two generations, [75, 76, 77]. At higher masses this choice may not be the best but the approach is consistent with previous analyses. The MC simulation is L.O. and so the cross section is more sensitive to Q^2 than it might be for higher order calculations. The effect on the choice of Q^2 is studied by doubling $Q^2 = 2.0 m_{VLQ3}$ and having $Q^2 = 0.5 m_{VLQ3}$ the value and comparing the total acceptance of samples generated with the default Q^2.

10.3 Parton Distribution Functions

To assign an uncertainty to the particular choice of Parton Distribution Functions (PDF) we used a weighted MC technique. The procedure is described in [78] and

illustrated in [79].

Several PDFs are considered during this study. *CTEQ5L* is the default PDF for the signal MC generation. We also considered *MRST72, MRST75, CTEQ6L and CTEQ6L1* and a set of PDFs collectively labeled *CTEQ6M*. The method is simple, we consider variations in the total selection $N_{pass}/N_{considered}$ of samples produced with two varied PDFs with respect to the total selection of a sample produced with our default PDF, *CTEQ5L*. The PDF *CEQ6M* comes with 20 parameters each of which is varied upward and downward. The PDF *CETQ6L* and *CETQ6L1* are treated as a paired variation for a total of 42 variations. Positive weights or increases in the total selection are attributed to a positive set. Negative weights are likewise attributed to a negative set. If the variations in cross section are either both positive or both negative the mean square average of the two results is added to the appropriate positive or negative set of variations. In the end, the values in each set are added in quadrature. A symmetric result for the PDF uncertainty is obtained by averaging the positive and negative results. This result is then added in quadrature with the result from the uncertainty in α_s. The uncertainty in α_s is determined using a ratio of weights obtained from the use of the *MRST72* and *MRST75* PDFs.

Further study of the systematic uncertainties due to choice of PDF is prompted by the observed mass dependence (see Table 10.1) and when the uncertainties obtained are smaller than our experience with the RPV Stop analysis [23] would have lead us to expect. This could be in part due to the higher momentum fraction of the events we are studying. The RPV Stop analysis set production cross section limits up to 170 GeV/c^2, while the expected mass limit of the $VLQ3$ is expected to be in the 320 GeV/c^2 range. A look at Figure 3.1 also shows that at higher masses, the cross section for $VLQ3$ production from gluon-gluon

fusion drops off more rapidly than the $q\bar{q}$ annihilation channel. It is in the gluon-gluon fusion production channel that different PDF choices can have a greater impact. A cross check is applied and a PDF uncertainty for the $VLQ3$ mass = 100 GeV/c^2 is found to be 4.2%, which extends the range of the observed trend with mass and is comprable to the PDF uncertainness considered for the RPV stop analysis.

Systematic uncertainties associated with backgrounds are included as uncertainties on the scale factors associated with with each background. The uncertainty associated with the $Z + jets$ background was investigated because this background is the third highest source of background and the PYTHIA MC simulation of this background involve both jet multiplicity and $\not\!\!E_T$ systematic uncertainties. To estimate the impact of these systematic associated with $Z + jets$ was increased by 50% and a new fit was made to determine the impact on the final cross section and mass limits. The new fit with higher $Z + jets$ systematics is shown for the Yang-Mills coupling in Figure 10.1 and for the Minimal Coupling model in Figure 10.3. Reduced scale versions are shown in Figures 10.2 and 10.4.

10.4 Jet Energy Scale

The JET-USER package which handles jet energy corrections also allows for shifts in the jet energy scale. We use this capability to study the systematic uncertainty associated with jet energies. The jet energy scales are shifted up and down by $\pm 1\sigma$ and the percent change in events in the signal region is recorded. A symmetric result for the jet energy scale systematic is obtained by averaging the two results. Table 10.3 displays the result for a variety of $VLQ3$ masses and in both the $e\tau_h$ and $\mu\tau_h$ channels.

$e\tau_h$	160 GeV/c^2 [%]	200 GeV/c^2 [%]	260 GeV/c^2 [%]	320 GeV/c^2 [%]	360 GeV/c^2 [%]
Positive	1.5	1.0	0.7	0.4	0.4
Negative	2.6	1.8	1.2	0.7	0.5
Average	2.0	1.4	0.9	0.6	0.4
α_s	1.2	1.2	0.6	0.7	0.5
Total	2.4	1.9	1.1	0.9	0.7
$\mu\tau_h$	160 GeV/c^2 [%]	200 GeV/c^2 [%]	260 GeV/c^2 [%]	320 GeV/c^2 [%]	360 GeV/c^2 [%]
Positive	1.6	0.8	0.5	0.6	0.3
Negative	3.1	1.1	0.8	1.0	0.7
Average	2.3	0.9	0.7	0.8	0.5
α_s	1.3	1.2	0.7	0.7	0.0
Total	2.7	1.5	1.0	1.1	0.5

Table 10.1: Systematic uncertainties (in %) on full selection due to the choice of PDF, shown for the $e\tau_h$ and $\mu\tau_h$ channels. The prescription for calculating the positive and negative uncertainties is described in the text, and the two are averaged. The uncertainty due to α_s is combined in quadrature with the average to give the total.

	m_{VLQ3} GeV/c^2										
Source	160	180	200	220	240	260	280	300	320	340	360
PDF											
Positive	7.0	7.1	7.5	7.7	7.9	8.4	8.8	9.3	9.9	10.4	11.3
Negative	-10.9	-11.1	-11.3	-11.4	-11.7	-12.0	-12.4	-13.0	-13.6	-14.4	-15.0
Q^2											
$Q = 2m_{VLQ3}$	27.9	28.2	28.3	28.3	28.6	28.9	29.1	29.3	29.7	30.0	30.4
$Q = 0.5m_{VLQ3}$	-43.7	-43.6	-44.0	-44.2	-44.8	-45.1	-45.5	-46.3	-46.5	-47.3	-48.0
Total +	28.8	29.1	29.2	29.3	29.7	30.1	30.4	30.8	31.3	31.7	32.4
Total -	-45.0	-45.0	-45.5	-45.7	-46.3	-46.7	-47.1	-48.1	-48.5	-49.5	-50.3

Table 10.2: Summary of systematic uncertainties on the cross section, given in %.

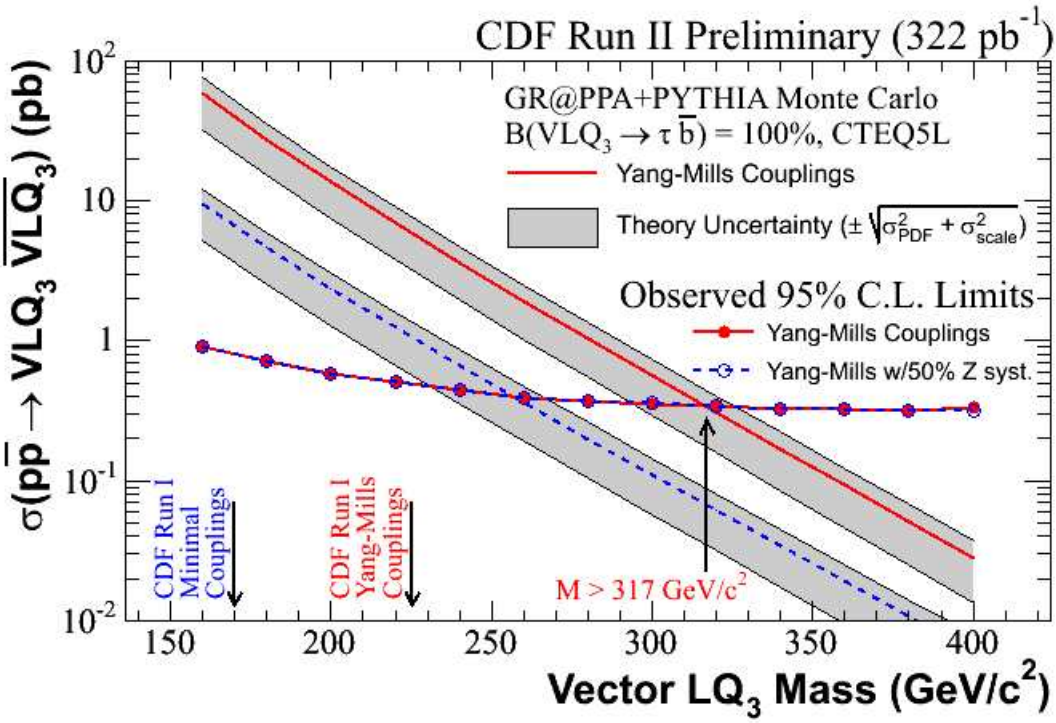

Figure 10.1: Cross section for increased Z + jets systematic for the Yang-Mill coupling case.

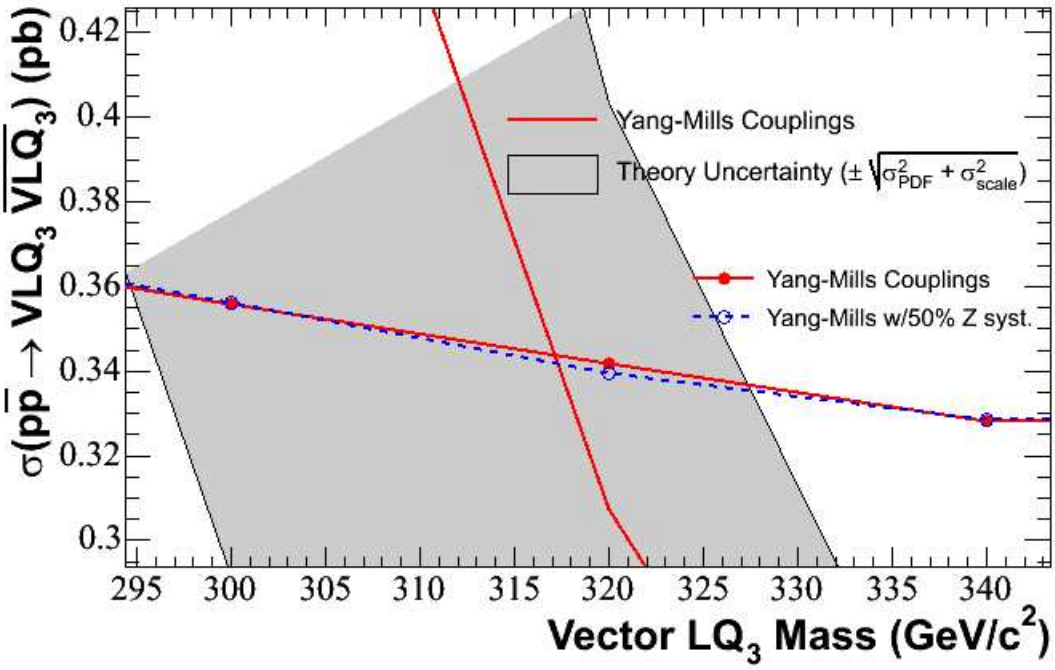

Figure 10.2: Cross section for increased Z + jets systematic for the Yang-Mill coupling case. The large gray area is the uncertainty $\sqrt{\sigma^2_{PDF}+\sigma^2_{scale}}$ associated with the theory curve.

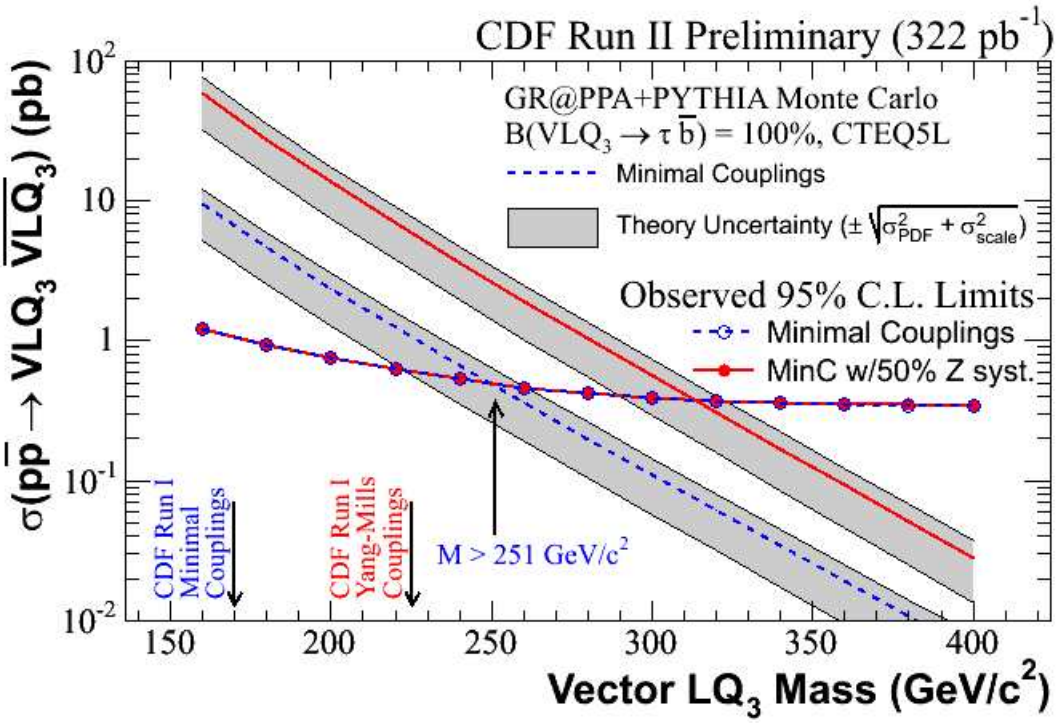

Figure 10.3: Cross section for increased Z + jets systematic for the minimal coupling case.

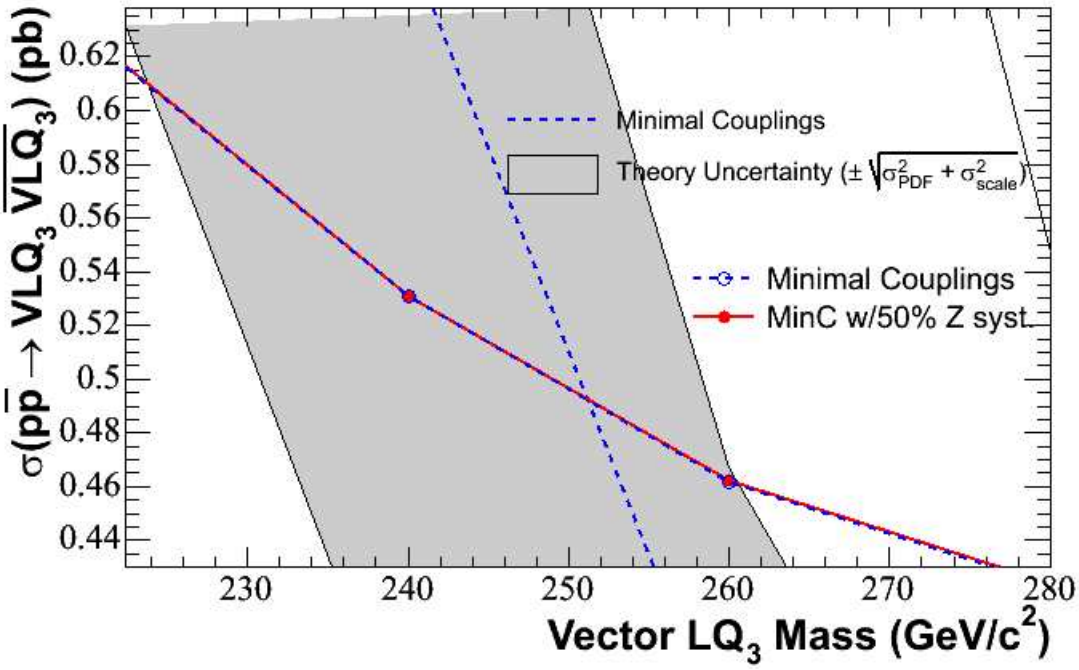

Figure 10.4: Cross section for increased Z + jets systematic for the minimal coupling case. The large gray area is the uncertainty $\sqrt{\sigma^2_{PDF} + \sigma^2_{scale}}$ associated with the theory curve.

10.5 Initial and Final State Gluon Radiation

In our MC framework GR@PPA models the event to the extent of specifying the parent quarks and gluons, the $VLQ3$ pair and the τb daughters along with their four vector momenta. The event is handed off to PYTHIA, which, among other things, adds Initial State Radiation (ISR) and Final State Radiation (FSR). This process is not exact and the associated systematic is estimated using reasonable variations in the amount ISR/FSR added to the event. ISR modified in PYTHIA by scaling the squared transverse momentum ($k_\perp^2$). This parameter, involved in the space-like parton shower evolution, is doubled and halved to determine the effect of ISR on the total acceptance. Similarly, FSR is modified by scaling a factor in the running evolution of α_s connected with the time-like parton shower evolution. This parameter is also doubled and halved. Because both processes ISR and FSR are related to the renormalization scale Q^2, the effect is mass dependent. See Tables 10.5 and 10.6 for the mass dependent result.

10.6 Missing Transverse Energy, $\not\!\!E_T$

Missing transverse energy is reconstructed and corrected as described in Section 9.5. The corrections include adjustments for the presence of jets and tau candidates in the event. Despite this, the method is still imprecise and a small systematic uncertainty must be assigned to $\not\!\!E_T$ reconstruction in the analysis. The correction for jets is already accounted for in the jet energy scale and is not double counted here. The systematic due to the tau correction is estimated by comparing the simple tau cluster momentum calculation, the default method to the improved "expanded tau cluster" method used in the analysis. The change

in the full selection, with respect to the defaults, yields the result shown in Table 10.4. The $e\tau_h$ and the $\mu\tau_h$ channels are considered separately.

10.7 Summary

A summary of systematic uncertainties is shown in Tables 10.5 and 10.6. The systematic uncertainty due to electron candidate acceptance and ID is 1.0%, see Section 7.4.2. For muon candidate acceptance and identification the systematic uncertainty is 3.0%, see Section 7.4.3. The systematic uncertainty due to tau acceptance and ID is 3.0% and is covered in Section 7.4.7. Isolation requirements have a conservative 3.0% uncertainty assigned to them, to cover differences between $Z^0 \to \tau\tau$ and data and between $Z^0 \to \tau\tau$ and $VLQ3$ Signal MC, Section 7.4.4.

$e\tau_h$	m_{VLQ3}												
	160	180	200	220	240	260	280	300	320	340	360	380	400
$+1\sigma$	7.2	5.8	5.1	4.6	3.6	2.4	1.7	1.4	1.2	0.9	0.7	0.4	0.4
-1σ	-7.7	-5.4	-5.3	-4.9	-4.4	-3.2	-2.6	-2.3	-1.4	-1.1	-1.1	-0.7	-0.8
Average	7.5	5.6	5.2	4.8	4.0	2.8	2.1	1.8	1.3	1.0	0.9	0.5	0.6
$\mu\tau_h$	m_{VLQ3}												
	160	180	200	220	240	260	280	300	320	340	360	380	400
$+1\sigma$	6.9	6.8	4.9	4.2	3.7	2.2	2.2	1.5	1.5	1.0	0.7	0.5	0.3
-1σ	-6.8	-6.8	-5.7	-4.7	-4.3	-3.3	-2.5	-2.1	-1.4	-1.2	-0.9	-0.7	-0.6
Average	6.8	6.8	5.3	4.4	4.0	2.7	2.4	1.8	1.4	1.1	0.8	0.6	0.4

Table 10.3: Systematic uncertainties (given in %) on full selection due to the jet energy scale.

	m_{VLQ3}												
	160	180	200	220	240	260	280	300	320	340	360	380	400
$e\tau_h$ channel	-0.1	0.1	-0.1	0.0	0.0	-0.1	-0.1	-0.1	0.0	0.1	-0.1	0.0	0.0
$\mu\tau_h$ channel	0.0	0.1	0.1	-0.2	-0.1	0.1	-0.1	0.0	-0.1	0.1	0.0	0.1	0.0

Table 10.4: Systematic uncertainties (given in %) on full selection due to the tau correction to the missing transverse energy, $\not{E}_T$.

	m_{VLQ3} GeV/c^2												
Source	160	180	200	220	240	260	280	300	320	340	360	380	400
PDF	2.4	2.1	1.9	1.6	1.4	1.1	1.0	1.0	0.9	0.8	0.7	0.7	0.6
ISR	3.6	3.6	3.6	3.6	3.6	3.6	3.6	3.6	3.6	3.6	3.6	3.6	3.6
FSR	3.7	3.7	3.7	3.7	3.7	3.7	3.7	3.7	3.7	3.7	3.7	3.7	3.7
Jet Scale	7.5	5.6	5.1	4.8	4.0	2.8	2.1	1.8	1.3	1.0	0.9	0.5	0.6
$\not\!\!E_T$	0.1	0.1	0.1	0.0	0.0	0.1	0.1	0.1	0.0	0.1	0.1	0.0	0.0
Acceptance	1.7	1.7	1.7	1.7	1.7	1.7	1.7	1.7	1.7	1.7	1.7	1.7	1.7
Lepton ID	1.0	1.0	1.0	1.0	1.0	1.0	1.0	1.0	1.0	1.0	1.0	1.0	1.0
Tau ID	3.0	3.0	3.0	3.0	3.0	3.0	3.0	3.0	3.0	3.0	3.0	3.0	3.0
Isolation	3.0	3.0	3.0	3.0	3.0	3.0	3.0	3.0	3.0	3.0	3.0	3.0	3.0
Total	10.5	9.2	8.9	8.6	8.1	7.6	7.4	7.3	7.1	7.1	7.1	7.0	7.0

Table 10.5: Summary of systematic uncertainties for the $e\tau_h$ channel, given in %.

	m_{VLQ3} GeV/c^2												
Source	160	180	200	220	240	260	280	300	320	340	360	380	400
PDF	2.7	2.1	1.5	1.3	1.1	1.0	1.0	1.0	1.1	0.8	0.5	0.5	0.4
ISR	3.7	3.7	3.7	3.7	3.7	3.7	3.7	3.7	3.7	3.7	3.7	3.7	3.7
FSR	3.6	3.6	3.6	3.6	3.6	3.6	3.6	3.6	3.6	3.6	3.6	3.6	3.6
Jet Scale	6.9	6.8	5.3	4.4	4.0	2.7	2.4	1.8	1.4	1.1	0.8	0.6	0.4
$\not\!\!E_T$	0.0	0.1	0.1	0.2	0.1	0.1	0.1	0.0	0.1	0.1	0.0	0.1	0.0
Acceptance	1.0	1.0	1.0	1.0	1.0	1.0	1.0	1.0	1.0	1.0	1.0	1.0	1.0
Lepton ID	3.0	3.0	3.0	3.0	3.0	3.0	3.0	3.0	3.0	3.0	3.0	3.0	3.0
Tau ID	3.0	3.0	3.0	3.0	3.0	3.0	3.0	3.0	3.0	3.0	3.0	3.0	3.0
Isolation	3.0	3.0	3.0	3.0	3.0	3.0	3.0	3.0	3.0	3.0	3.0	3.0	3.0
Total	10.4	10.3	9.2	8.7	8.5	7.9	7.8	7.7	7.6	7.5	7.5	7.4	7.4

Table 10.6: Summary of systematic uncertainties for the $\mu\tau_h$ channel, given in %.

Chapter 11

Results

Discovery of a new particle is, of course, the goal of any exotic particle search, but as a practical matter, the result of such a search is often the establishment of new limits on intrinsic mass and production cross section of the particular particle species under study. An exotic particle search therefore has two separate goals. The first is to extend the sensitivity of any search to establish the lowest feasible upper limit on the production cross section and the highest feasible lower limit on the intrinsic mass. This typically means that we craft our analysis to detect the highest possible invariant mass limited by the amount of data available and the efficiency of the analysis. The second goal, of which we must never lose sight, is to ensure sensitivity between the previous limit and the new upper limit, thus retaining the possibility of actually discovery.

The search for 3rd generation vector leptoquarks followed a *Blinded Analysis* procedure. Through the use of signal MC, we determined the portions of the parameter space most likely to contain our $VLQ3$ signature. Our event signature $\tau_{lep}b\tau_h b/$ led to parameterizing the phase space in two variables, total transverse energy, H_T, and the number of jets, N_{jets}.

Control regions are defined for $N_{jet} = 0$ and 1 without constraint on H_T. A control region for $N_{jet} \geq 2$ is defined for $H_T \leq 250$ GeV. The upper limit of H_T in this region corresponds to the value expected from a $VLQ3$ at the previous mass limit [80]. The remaining portion of the parameter space is divided into SAFE and SIGNAL regions.

Preliminary studies indicated that for 332 pb^{-1} of data we could hope to detect a $VLQ3$ of mass no more than ~ 320 GeV. This limit is based upon the best theoretical cross section generated with GR@PPA and on the total efficiency of the analysis. Studies of the value of H_T in background discrimination $S/\sqrt{S+B}$ led to setting the event level cut, $H_T \geq 400$ GeV. This H_T cut forms the boundary between the SAFE region and the SIGNAL region. While the highest sensitivity to a high mass $VLQ3$ signature lies in the SIGNAL region we need to maintain the ability to detect a $VLQ3$ of lower intrinsic mass. These events would be likely to produce lower values of E_T for the jets, τ_{lep} and τ_h and therefore of H_T in the SAFE[1] region. The SAFE region in this situation becomes the place where most of the power of the discovery measurement would come from. Two regions are complementary in that they are sensitive to high and low mass $VLQ3$ with the combination covering both possibilities.

The "Blind Analysis" procedure is then a self-imposed requirement that we not look at the kinematic distributions from data in either our SIGNAL or SAFE regions until we have established with confidence that we understand the kinematic distributions present in the control regions. Once the backgrounds are well understood the decision is made to "unblind" the SAFE region (January of

[1]The SAFE region is so named from "safety region" or a buffer between the previously excluded region CR2J and the new optimized SIGNAL region. We need to exclude the entire region $N_{jet} \geq 2$ and $H_T \leq 250$ GeV in addition to the SIGNAL region above the H_T cut. Even though our sensitivity to $VLQ3$ pair production in this region is at less than the optimal sensitivity, a discovery in this range could not "a priori" be excluded.

2006). The analysis group imposed a short hiatus, a period of two weeks, before unblinding the SIGNAL region (February 2006). This was done in order to resolve questions within the analysis group concerning the kinematic distributions revealed by unblinding the SAFE region.

11.1 SAFE Region

The the safety region ($N_{jets} \geq 2$ and $250 \leq H_T \leq 400$ GeV) contained 5 events in the $e\tau_h$ channel and 3 events in the $\mu\tau_h$ channel. The result is consistent with background. Kinematic distributions for the SAFE region are displayed in Figures 11.1 to 11.8.

11.2 Signal Region

After the results of the SAFE region are studied and understood to be within the expectation of the analysis the signal region defined as $N_{jets} \geq 2$ and $H_T > 400$ GeV is unblinded. No events are found in either the $e\tau_h$ or the $\mu\tau_h$ channels.

While it is tempting to regard a null result as disappointing, in respect we were extremely fortunate. Our total expected background in the control region was $\sim$ half an event. We could have, with nearly equal probability, ended up with one event in the signal region. This would have placed severe limits on our ability to set mass and cross section limits using the likelihood method detailed next.

11.3 Signal Extraction

The SIGNAL region definition is chosen to extend the sensitivity of the analysis to the highest feasible mass limit and the lowest feasible cross section limit. In the event of a discovery, a significant portion of the $VLQ3$ signal would have shown up in the SAFE region. For this reason the fit procedure treats the SAFE and SIGNAL region as separate bins in constructing the likelihood function

$$\nu_i = \nu_i^b + \nu_i^s. \tag{11.1}$$

Here the v_i are the full rates of signal v_i^s and background v_i^b and where the index i indicates one of four channels. There are separate channels for $e\tau_h$ $\mu\tau_h$ and for SAFE and SIGNAL regions, see Table 11.1.

The Poisson probability is used to model the probability of the true rates being within $d\nu_i$ of v_i given the number of observed events N_i:

$$d\mathcal{P} = \prod_{i=A1,B1,A2,B2} P(\nu_i, N_i) d\nu_i, \tag{11.2}$$

where $P(\nu_i, N_i)$ is the Poisson distribution for the expected rate ν_i. The variables are then transformed $(\nu_i) \rightarrow (\nu_i^s)$. At this stage, knowledge of background rates are modeled as exact. Uncertainties are included later, Equation 11.6.

	$250 < H_T < 400$	$400 < H_T < \infty$
$e\tau_h$ channel	A1	A2
$\mu\tau_h$ channel	B1	B2

Table 11.1: Definitions of the regions used in the log-likelihood fitting method.

Next, we use a physically meaningful cross section for the signal rate for each

of the bins,i.

$$\nu_i^s = \sigma_i \left(VLQ3\overline{VLQ3} \times L \times Br(\tau\tau \rightarrow \tau_{lep}\tau_h \times \alpha_i) \right) \tag{11.3}$$

Here, the factor L is the integrated luminosity, α_i is the selection efficiency in each of the regions. This latter value will be replaced with an expression which takes into account the systematics affecting the selection efficiency in a manner similar to the method used for handling the uncertainties associated with the backgrounds, Equation 11.6. The Jacobian of this transformation is proportional to $L^3 \prod \alpha_i$.

For the moment, this leads to four degrees of freedom in the effective cross section in each of the regions where we should only have one. This can be handled by requiring the cross section to be the same in all of the channels defined in Table 11.1. The four separate cross sections are reduced to one with a delta function of the form,

$$\delta(\sigma_{A1} - \sigma_{B1})\delta(\sigma_{A2} - \sigma_{B2})\delta(\sigma_{B1} - \sigma_{A2}). \tag{11.4}$$

Several of the backgrounds are obtained from MC and we have to take into account how these contributions scale with luminosity. We break each contribution into a luminosity dependent $\nu_i^{b''}$ and a luminosity independent $\nu_i^{b'}$ part.

$$\nu_i^b = \nu_i^{b'} + \nu_i^{b''} \frac{L - L_0}{L_0} \tag{11.5}$$

Here L is the same as the luminosity used in the signal rate estimation, Equation 11.3. A Gaussian shape to the backgrounds is introduced as an additional prior with negative rates cut off in the final integral.

Correlated systematic uncertainties for backgrounds are incorporated by re-

placing the background rates with:

$$\nu_i^b \rightarrow \nu_i^b + \sum x_k \delta_k \nu_i^b, \tag{11.6}$$

where x_k is a weight determining the degree of variation in the kth systematic with a weight of $x_k = 1$ on a Gaussian systematic corresponding to a 1 sigma variation. The factor $\delta_k \nu_i^b$ incorporates the effect of each systematic on the specific background rate. The same method is used to modify the selection efficiencies α_i to account for systematic uncertainties.

$$\alpha_i \rightarrow \alpha_i + \sum x_k \delta_k \alpha_i, \tag{11.7}$$

The parameters x_k are now additional integration variables in the final likelihood with a prior of the form $exp(-x_k^2/2)$.

All of the variables except σ are integrated over to form the likelihood which takes the form of a probability density. We use 95% C.L. highest posterior density intervals to determine the maximum allowed cross section value. The null result, e.g. no events observed, means that the integration is carried out over the range 0 to 95% of the full probability.

Figure 11.9 shows the result of a mass dependent fit to a 95% C.L. upper limit on the $VLQ3$ pair-production cross section. The plotted curves are color coded, the upper red curve is for Yang-Mills and lower or blue curve is for the Minimal Couplings curve. Theoretical predictions of the cross section are given as smooth curves and their respective uncertainties are given as a gray band surrounding each. Experimental data points are shown for specific mass points with solid red circles indicating the Yang-Mills and the open blue circles indicating

	$\sigma < (fb)$	$m_{VLQ3} >$ (GeV/c^2)
Yang - Mills	344	317
Minimal Coupling	493	251
For theoretical uncertainties applied in the least favorable manner.		
Yang - Mills	360	294
Minimal Coupling	610	223

Table 11.2: Results for $VLQ3$ pair production cross section upper limits and for the intrinsic mass m_{VLQ3} lower limits and for the 3rd generation vector leptoquark search conducted with 332 pb^{-1} of data at CDF in Run II. The results are shown for two models, Yang-Mills and for the Minimal Coupling case. Also shown are the Yang-Mills and Minimal Coupling cases with 1 σ varied theoretical uncertainties applied in a conservative manner reducing the mass limits and increasing the cross section limits.

the minimal coupling. The intersection of the experimental and theoretical for the same coupling type (same color) establishes the upper limit $VLQ3$ pair production cross section and the lower limit on the intrinsic mass at the 95% C.L. Limits that include a conservative -1σ theoretical uncertainty are obtained by observing the intersection of the experimental curve with that of the lower bound of the appropriate (same color) theoretical gray band.

11.4 Summary

This analysis has searched for a third generation vector leptoquark ($VLQ3$) in the di-tau plus di-jet channel using $322pb^{-1}$ of Run II data. The results are displayed in Table 11.2. Four different models are used, Yang-Mill coupling assumes $\kappa = \lambda = 0$ and the Minimal Coupling model assumes the values of κ and λ which give the lowest production cross section. All results are at 95% C.L. and Br(LQ3 $\rightarrow b\tau) = 1$ is used throught.

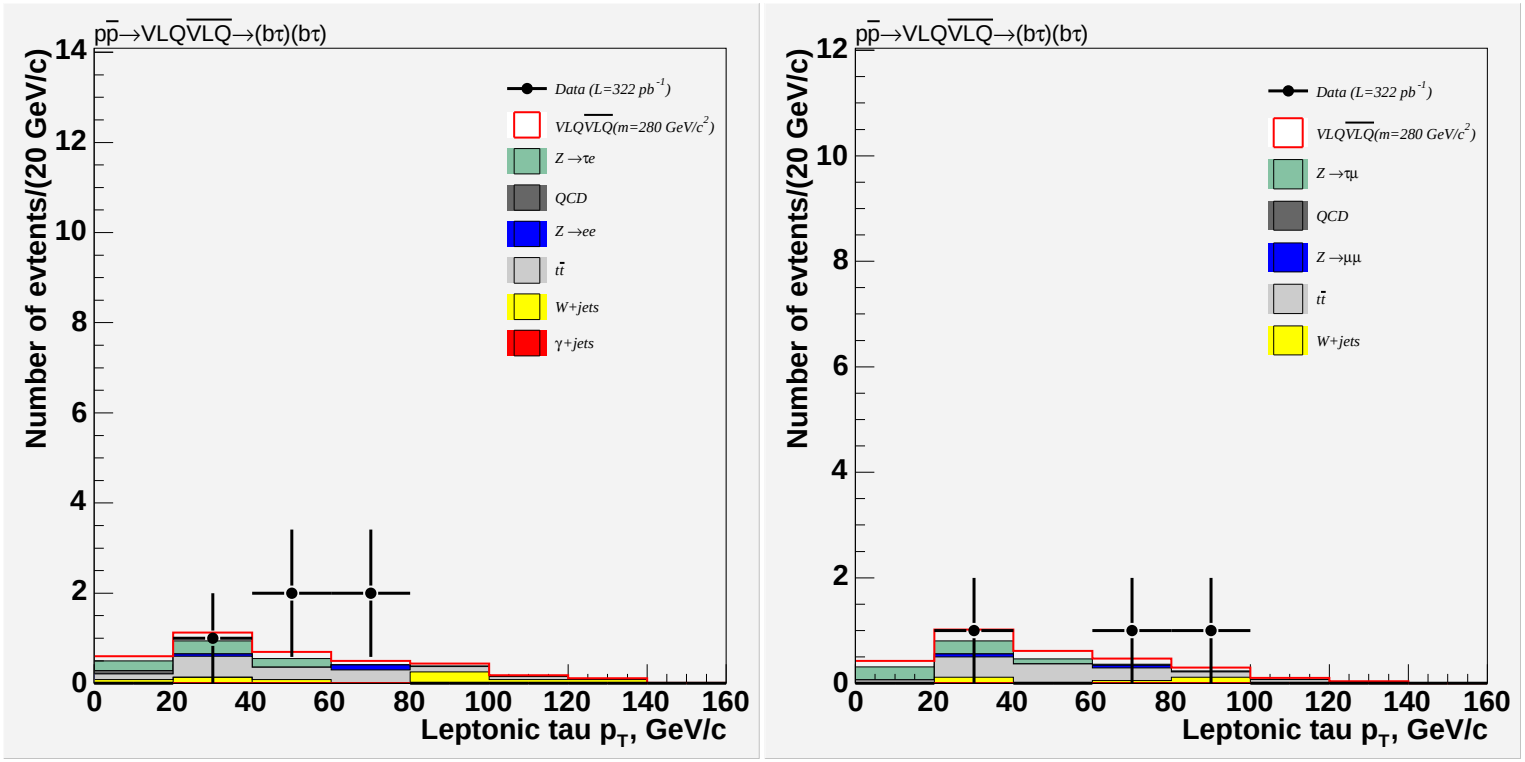

Figure 11.1: Distributions for electron E_T (left) and muon p_T (right) for the safety region.

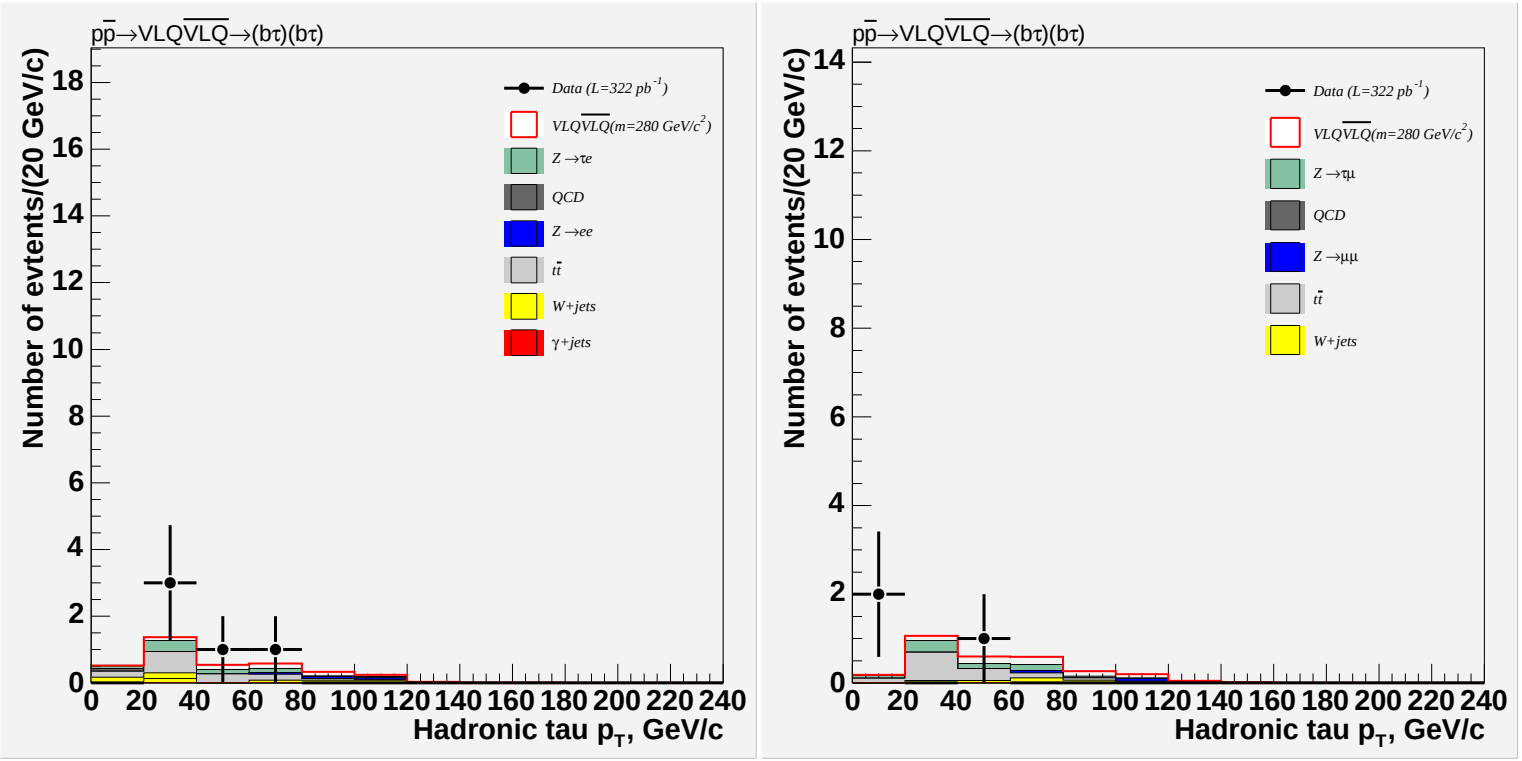

Figure 11.2: Distributions for hadronic tau p_T in the electron channel (left) and muon channel (right) for the safety region.

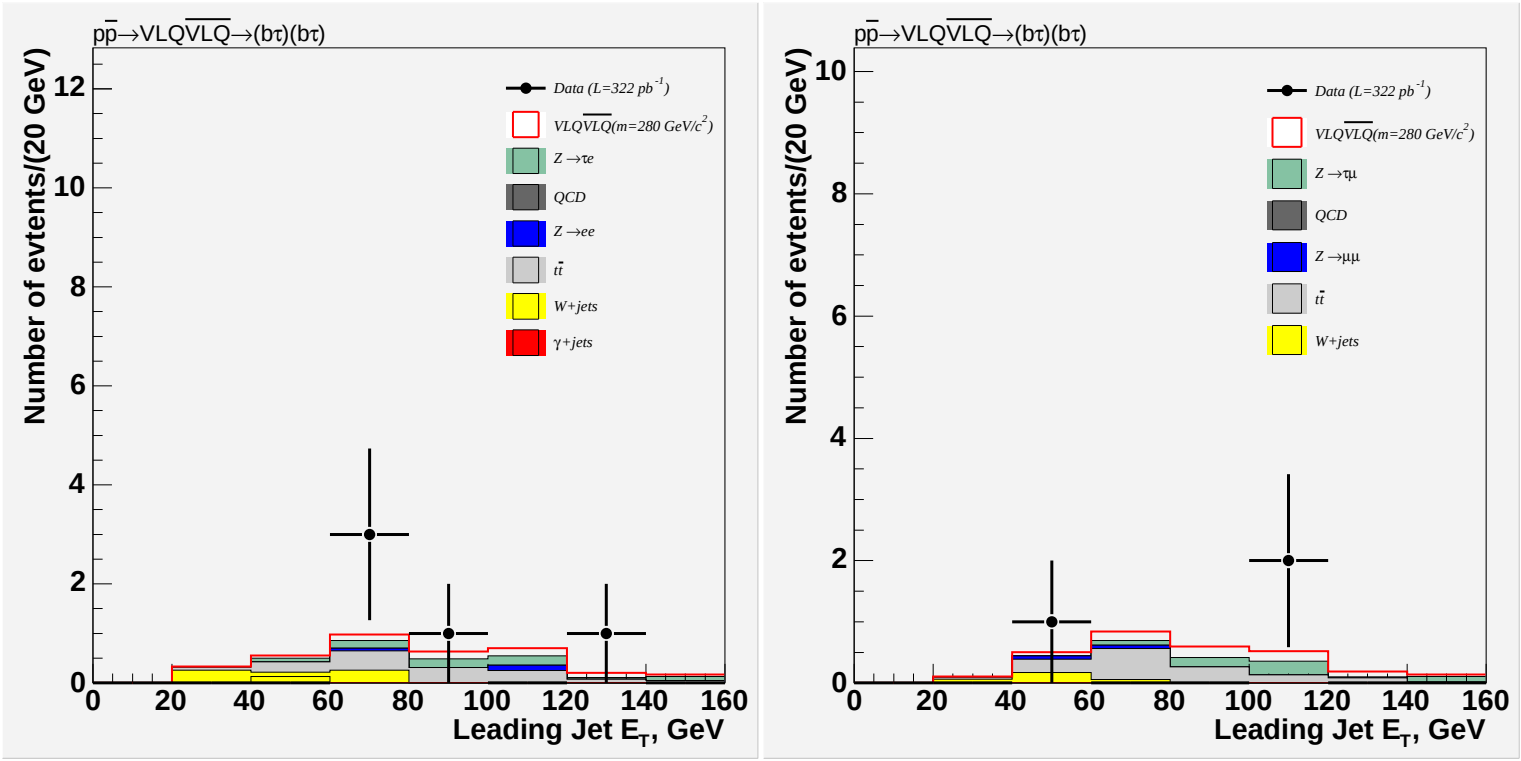

Figure 11.3: Distributions for the leading jet E_T in the electron channel (left) and muon channel (right) for the safety region.

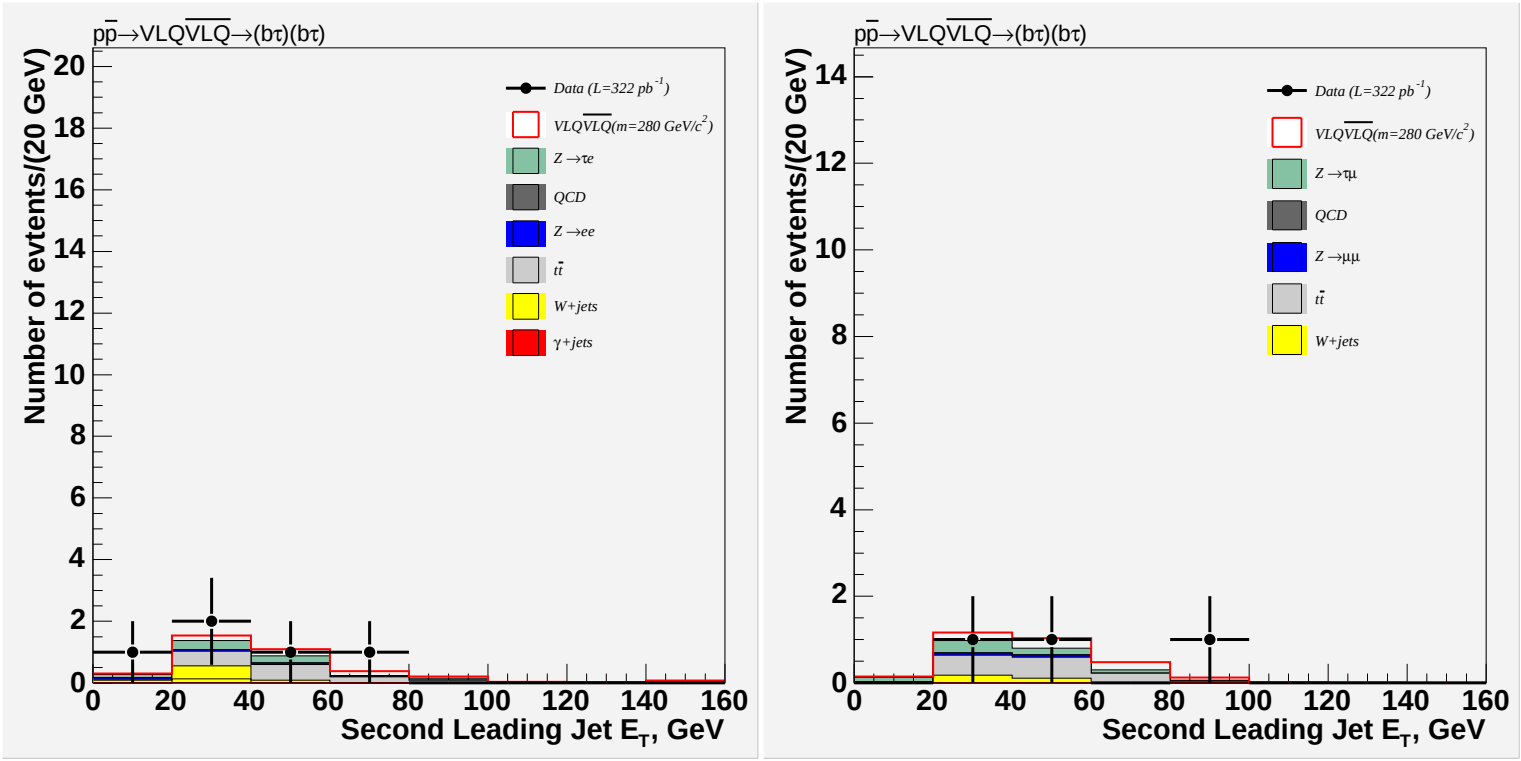

Figure 11.4: Distributions for the second jet E_T in the electron channel (left) and muon channel (right) for the safety region.

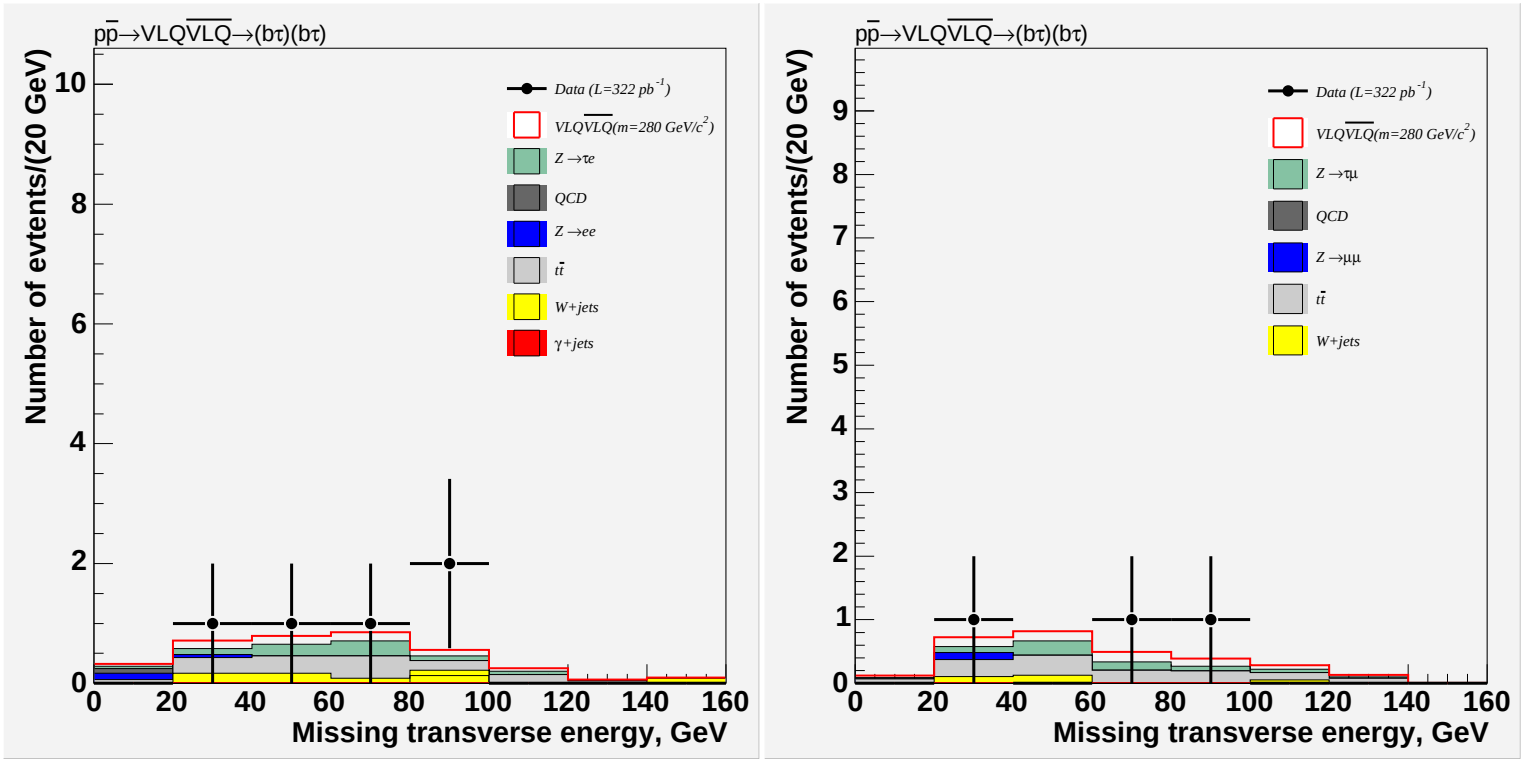

Figure 11.5: Distributions for $\not\!\!E_T$ in the electron channel (left) and muon channel (right) for the safety region.

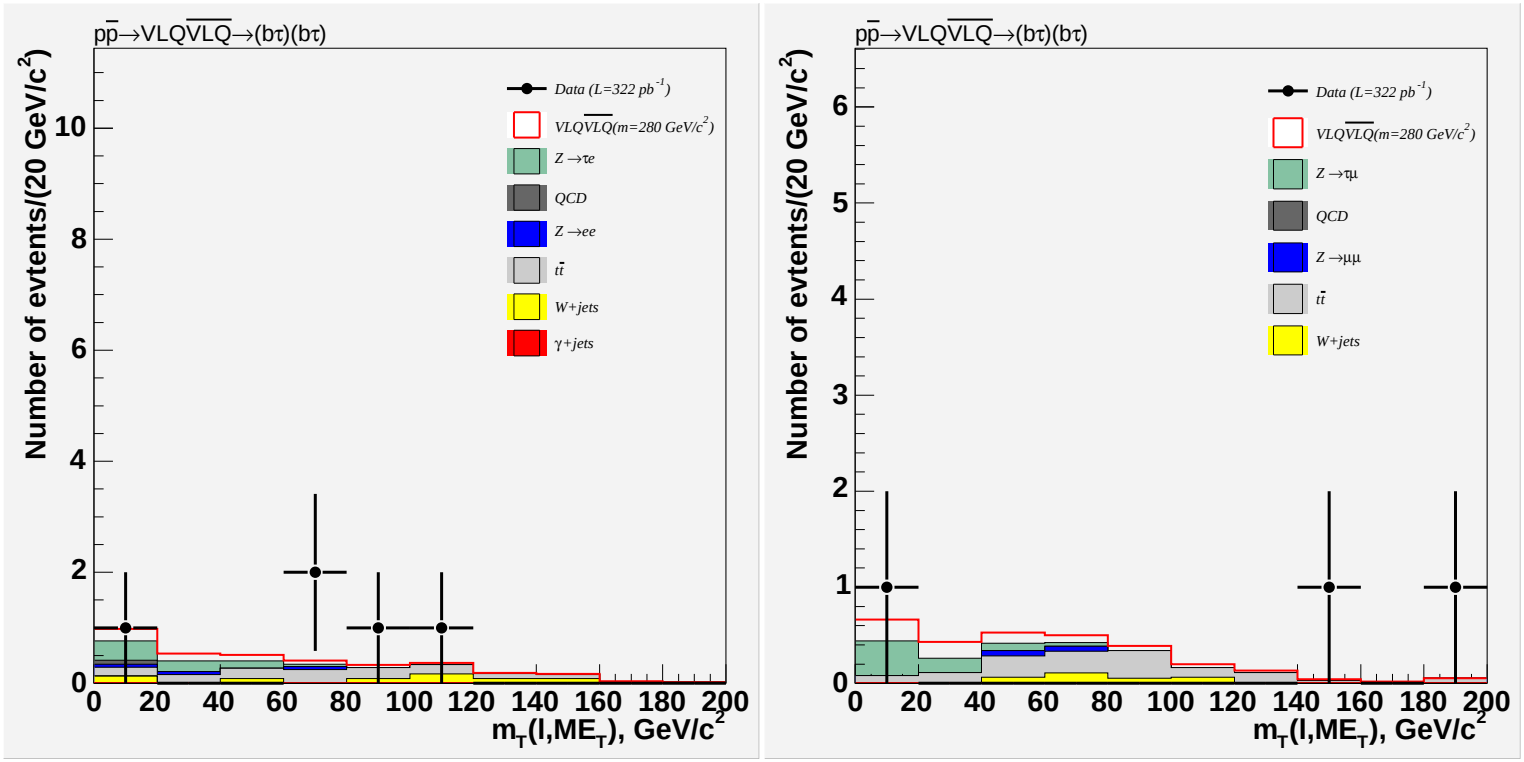

Figure 11.6: Distributions for M_T in the electron channel (left) and muon channel (right) for the safety region.

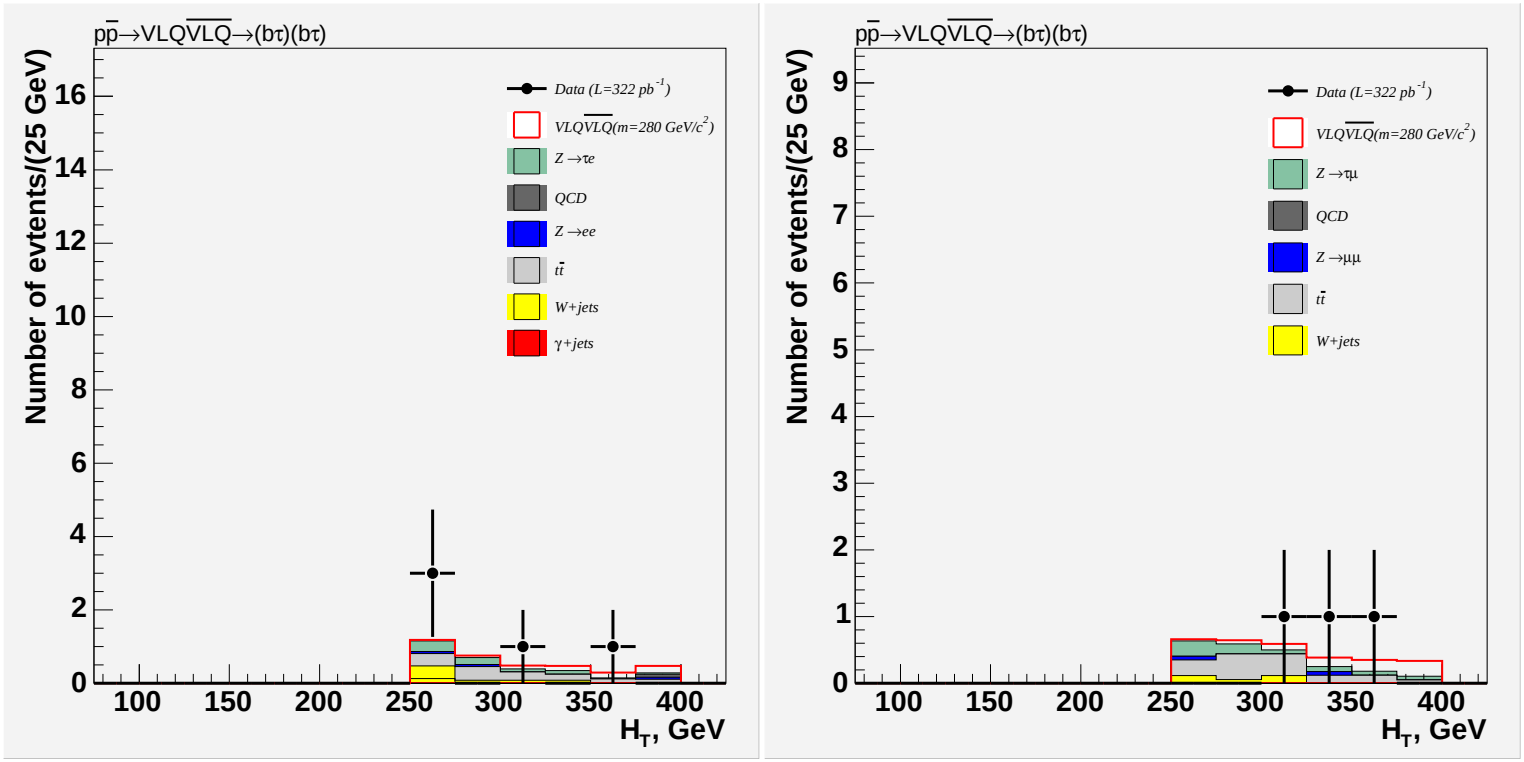

Figure 11.7: Distributions for H_T in the electron channel (left) and muon channel (right) for the safety region.

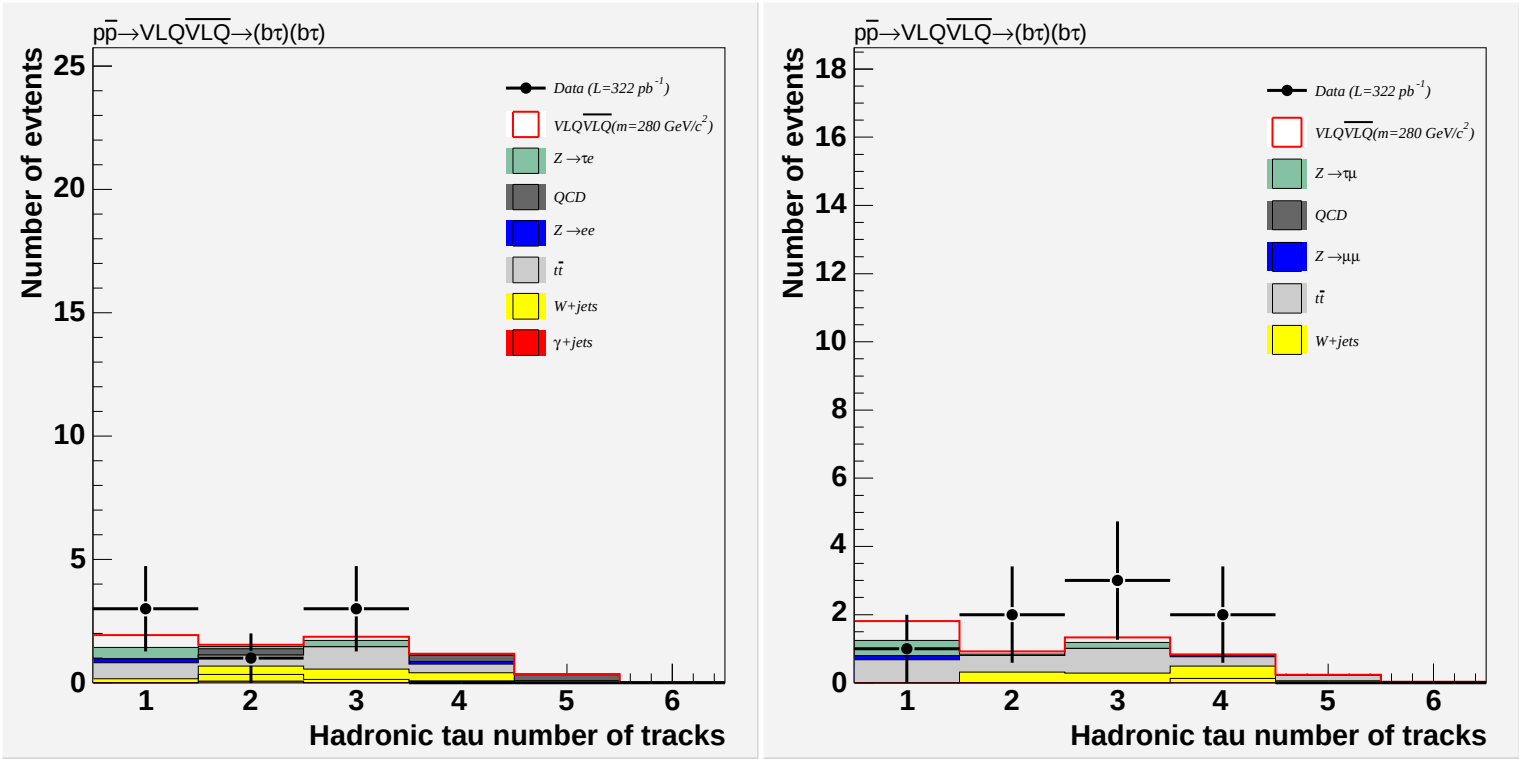

Figure 11.8: Distributions for N_{prongs} in the electron channel (left) and muon channel (right) for the safety region.

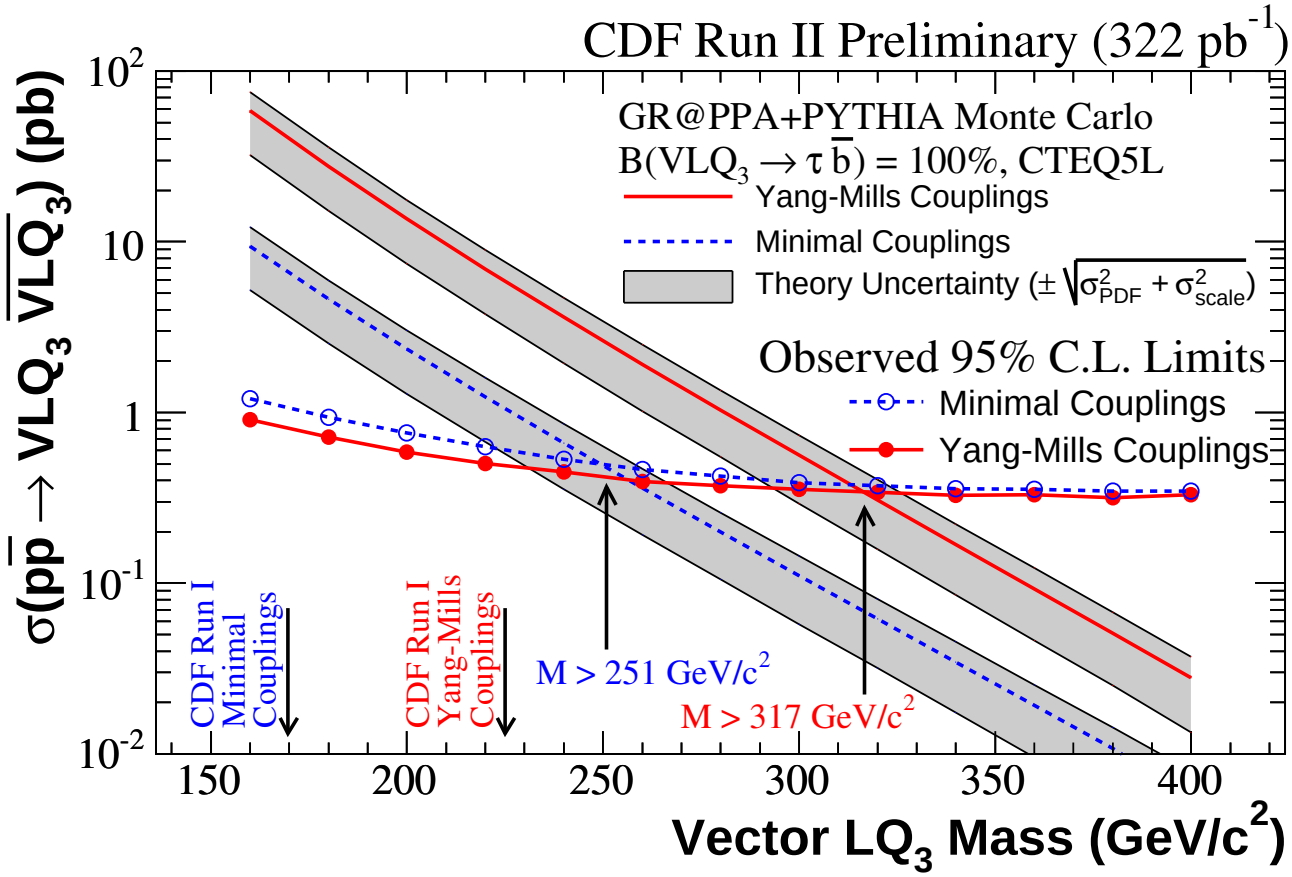

Figure 11.9: Pair production cross section as a function of LQ3 mass for experimental results (curves with data points) and theory predictions (solid curves) for the cases of Yang-Mills couplings (red) and Minimal couplings (blue). The band due to the uncertainty on the theoretical prediction (gray) is also shown, and includes the uncertainty due to the choices of PDF and Q^2 scale. The CDF Run I mass limits are also indicated in the lower left of the plot.

Chapter 12

Prospects

The prospects for future searches for vector leptoquarks is good. While this analysis was completed with $332pb^{-1}$ of data, CDF already has $1fb^{-1}$ written to tape as of early 2006. Projections of data to tape at CDF before 2009 are a conservative $2fb^{-1}$ and an optimistic $4fb^{-1}$. By 2009 the Large Hadron Collider (LHC) should be online taking data at rates and energies far outstripping CDF.

12.1 CDF at Large Integrated Luminosities

The *Lepton + Track* dataset used in this analysis totaled roughly half of all of the data written to tape during the relevant time period. This loss of runs from the "good run list" was due to a number of factors, including the reliability of various detector subsystems. Using one half as a rule of thumb approximation, this means setting new limits with datasets 1 and $2fb^{-1}$ in size. The smaller of these corresponds to a scaling of the dataset size by factor of 3. Absent any improved method of suppressing backgrounds, they should be expected to increase linearly with the size of the data set. Using the same strategy of control

regions based on H_T and N_{jets} this leads to a projected increases in backgrounds in the SAFE region to 15 events in the $e\tau_h$ channel and 9 events in the $\mu\tau_h$ channel. The corresponding background contamination in the SIGNAL region would rise to ~ 1.5 events in both channels.

That said, a new analysis will take advantage of the null result from this analysis to reoptimize the H_T cut for a higher mass $VLQ3$. These higher mass $VLQ3$ will produce stiffer distributions in the jet, τ_h and τ_{lep} candidate E_T. This would result in shifting the H_T distribution in Figure 9.2 to the right, changing the lower boundary defining the SIGNAL region. Without actually redoing the analysis it is difficult to say if the increased power of the H_T cut, given a similar increase in backgrounds is enough to improve background discrimination, but it is unlikely to do worse.

There are several supporting analyses which would need to be completed prior to repeating this analysis with a larger dataset. The trigger efficiencies at all three levels for *Lepton + Track* would need to be reevaluated over the new dataset and run range. Separate trigger efficiency studies for the electron, muon and tau-track legs of the event topology would need to be evaluated. For the medium p_T range, standard electron, muon and tau ID cuts and associated efficiencies would need to be evaluated and accepted by the collaboration. Background studies including MC generation and scale factor determinations need to be conducted. Finally, signal MC generation can, from experience, be estimated at taking 3 months. This includes 13 mass points with a similar number of events spread over a larger number of runs, along with MC sets to support ISR/FSR, PDF and coupling model studies.

The the previous mass limit, $m_{VLQ3} > 225$ GeV/c^2 set during Run I of the Tevatron, uses 110 pb^{-1}. This, however is also due to the advent of the *Lepton*

+ *Track* triggers. Our dataset is almost exactly three times that size and we improved the mass limit by 92 GeV/c^2. An increase in the size of the dataset to 1 fb^{-1} increases the dataset by roughly the same factor. Therefore, assuming no $VLQ3$ events are found, a < 90 GeV/c^2 increase in the mass limit is not an unreasonable expectation.

12.2 Large Hadron Collider

The Large Hadron Collider (LHC) is a 14 TeV center-of-mass pp collider located near Geneva, Switzerland. Operated by CERN, the European Center for Particle Physics, the collider straddles the French-Swiss border and when commissioned will be the highest energy colliding beam accelerator in the world. The design bunch crossing rate and luminosity are respectively 25 ns and $10^{-34} cm^{-2} s^{-1}$ leading to a projected eventual 100 fb^{-1} of data taken per year. Even a fractional achievement of these design criteria will supply exotic particle searches with enough data to quickly outstrip any existing analysis.

Higher energy searches for vector leptoquarks can commence once the LHC comes online and has taken a significant amount of data. Projections of late 2009 for this date are based on a conservative estimate of the commissioning sequence that any new collider/ detector complex will have to go through. Announcements as of November 2006 have pushed beam collisions back to November 2007 where they will commence at $\sqrt{s} = 1.8$ TeV. This initial beam energy is actually lower than the current beam energy at the Tevatron, but experience with the Tevatron suggests that full design performance of both the accelerator and detectors are best approached incrementally. With these caveats in mind, even modest simultaneous improvements in bunch crossing rate, luminosity and beam energy will be

sufficient to probe energies and cross sections beyond the reach of the Tevatron.

The two detectors at the LHC which we can expect to contribute to leptoquark searches are ATLAS and CMS. ATLAS stands for, "A Toroidal LHC Apparatus" while CMS stands for the "Compact Muon Solenoid". Similar to CDF, both instruments are designed to be general purpose detectors at which a number of research areas, including but not limited to, leptoquark searches will be advanced.

The primary difference for searches conducted at the LHC as opposed to the Tevatron is that the beams are $p - p$ rather than $p - \bar{p}$. The relative availability of antiquarks at the Tevatron leads to $q\bar{q}$ annihilation dominating gg fusion as the $VLQ3$ pair production mechanism. This will be reversed at the LHC.

While no studies specific to $VLQ3$ searches have been published there is a first and second generation vector leptoquark projected limit at 1.7 TeV [81] and a projected scalar leptoquark limit of 1.3 TeV [82]. The latter limit dates from 2004 using the ATLAS simulation (ALTFAST) and assuming 30 fb^{-1} of data taken after three years of running at low luminosity. This is a very conservative estimate of LHC/ATLAS performance, but is still a factor of 10 higher than the current $m_{scalar} > 129$ GeV/c^2 result [27].

Chapter 13

Conclusions

We have conducted a search for the $VLQ3$s pair produced in colliding $p\bar{p}$ beams operating at $\sqrt{s} = 1.96$ GeV in Run II of the CDF experiment. In the process, we have obtained the world's best mass and cross section limits for the $VLQ3$. We have established model dependent upper limits on the production cross section and lower limits on the $VLQ3$ mass. For the Yang-Mills coupling model, the $VLQ3$ pair production cross section limit is $\sigma < 344fb$ or with the least favorable treatment of the theoretical uncertainties, $\sigma < 360fb$. The corresponding mass limits on the $VLQ3$ are $m_{VLQ3} > 317$ GeV/c^2 and $m_{VLQ3} > 294$ GeV/c^2. For the Minimal Coupling model the pair production cross sections are $\sigma < 493fb$ or with the same least favorable treatment of the theoretical uncertainties $\sigma < 610fb$. Here the mass limits are $m_{VLQ3} > 251$ GeV/c^2 and $m_{VLQ3} > 223$ GeV/c^2.

Although the work done in this analysis was specifically for the U_1 type vector leptoquark, the model-independent nature of the matrix element generator means that the work is directly applicable to searches for other species of scalar and vector leptoquark. For the first time, a matrix element generator is used to preserve information on tau helicity needed to properly treat their decays.

Bibliography

[1] F. Abe *et al.*, Phys. Rev. Lett. **74**, 2626 (1995).

[2] S. Weinberg, Phys. Rev. Lett. **19**, 1264 (1967).

[3] A. Salam, *Elementary Particle Theory* (ed N. Svartholm, Stockholm: Almqvist and Wiksell, ADDRESS, (1968) 367).

[4] S. Glashow, J. Iliopoulous, and L. Maiani, Phys. Rev. D2 1264 (1970).

[5] D. Griffiths, *Introduction to Ekementary Particles* (Wiley, New York, 1987).

[6] L. H. Ryder, *Quantum Field Theory* (Cambridge University Press, Cambridge, 1985).

[7] M. Peskin and D. Schroeder, *An Introduction to Quantum Field Theory* (Addison-Wesley, New York, 1995).

[8] K. Hagiwara *et al.*, Phys. Rev. Lett. D **66**, 010001 (2002).

[9] D. I. Kazakov, Beyond the Standard Model (In Search of Supersymmetry), 2000.

[10] L. E. W. Group, http://lepewwg.web.cern.ch/LEPEWWG .

[11] T. C. Collaboration, Combined Upper Limit on Standard Model Higgs Boson at CDF for summer 2006, CDF Note 8403, (2006).

[12] H. Georgi and S. Glashow, Phys. Rev. Lett. **32**, 438 (1974).

[13] J. Elwood and A. Faragg, Exotic Leptoquarks from Superstring Derived Models, hep-ph/9704363.

[14] J. Pati and A. Salam, Phys. Rev. D. **10**, 275 (1974).

[15] B. Schrempp and F. Schrempp, Phys. Rev. B. **153**, 101 (1985).

[16] E. Farhi and L. Susskind, Phys. Rep. **74**, 227 (1981).

[17] E. Eichten, I. Hinchliffe, K. Lane, and C. Quigg, Phys. Rev. D. **34**, 1574 (1986).

[18] S. Adler *et al.*, Phys. Rev. Lett. **88**, 041803 (2002).

[19] O. Shanker *et al.*, Nucl. Phys. **204**, 375 (1982).

[20] W. Buchuller, R. Ruckl, and D. Wyler, Nucl. Lett. **B191**, 442 (1987).

[21] J. Blumlein *et al.*, hep-ph/9610408 (1996).

[22] The CDF Collaboration, FERMILAB-Pub-04-303-E (2004), (2004), submitted to Phys. Rev. Lett.

[23] M. Chertok *et al.*, Search for Pair Production of Stop Quarks Decaying to τ and a b, CDF Note 7704, Phys. Rev. Lett. in preparation.

[24] S. Tsuno, The GRACE matrix element generator, hep-ph/0501174 .

[25] S. Tsuno *et al.*, Comp. Phys. Comm. **151**, 126 (2003).

[26] M. Chertok *et al.*, Search for SUSY stop quark or 3rd Generation Scalar Leptoquark decaying to tau and a b-quark, CDF Note 7398, (2004).

[27] T. Akimoto *et al.*, Search for the 3rd Generation Vector Leptoquark, CDF Note 8154, (2006), Phys. Rev. Lett. in draft.

[28] J. Kim, T. Moulik, and P. Murat, CDF Run II Interface to TAUOLA an decay library for polarized τ leptons, CDF Note 5719, (2001).

[29] M.-T. Group, *GRACE Manual, KEK Report 92-19* (Minami-Tateya Group, ADDRESS, (1993)).

[30] S. Tsuno and J. R. Smith, Leptoquark Generator for Hadron Colliders, CDF Note 7937, Comp. Phys. Comm. article in preparation.

[31] Fermilab Operations Rookie Books, Accelerator Division.

[32] D. Kaplan, Fixed-Target CP-Violation Experiments at Fermilab, hep-ex/9509009.

[33] I. Stancu *et al.*, Technical Design Report for the MiniBooNE Neutrino Beam, May 13, 2001.

[34] The NuMI-MINOS Technical Design Report.

[35] S. van der Meer, Rev. Mod. Phys. **57**, 689 (1985).

[36] J. A. MacLachlan *et al.*, Prospectus for an electron cooling system for the recycler, FERMILAB-TM-2061.

[37] L. R. Prost and A. Shemyakin, Efficiency of the Fermilab electron cooler's collector, To appear in the proceedings of Particle Accelerator Conference (PAC 05), Knoxville, Tennessee, 16-20 May 2005.

[38] R. C. Fernow, *Introduction to Elementary Particle Physics* (Press Syndicate of the University of Cambridge, 32 East 57th Street, New York, N.Y. 10022, USA, 1986).

[39] P.Squillacioti *et al.*, Particle Identification by combining TOF and dEdx information, CDF Note 7488, (2005).

[40] S.Worm *et al.*, SVXII Silicon Strip Sensor Specifications and Conformance Testing, CDF Note 3713, (1996).

[41] G.Bolla and D.Bortoletto, Silicon Sensors for the SVX II Upgrade, CDF Note 4667, (1998).

[42] S. Hou, Nucl. Instrum. Meth. A511: 166-170, 2003.

[43] T. Affolder *et al.*, Nucl. Instrum. Meth. A526: 249, 2004.

[44] Allspach *et al.*, Aging in the Large CDF Axial Drift Chamber, CDF Note 7406, (2004).

[45] R. Blair *et al.*, The CDF II Detector Technical Design Report, FERMILAB-Pub-96/390-E, Nov 1996. 234pp., (1996).

[46] C. Hays *et al.*, COT Momentum Scale for the W Mass Analysis, CDF Note 7852, (2005).

[47] Y. S. for the CDF Collaboration, CDF Calorimeter and Its Upgrade, FERMILAB-Conf-95/001-E, (1995).

[48] S. Klimenko *et al.*, The CDF Run II Luminosity Monitor, CDF Note 4330, (1999).

[49] J.Elias *et al.*, Luminosity monitor based on Cherenkov counters for ppbar colliders, CDF Note 5003, (1999).

[50] N. Bachetta *et al.*, Report of the Silicon Operations Review Committee, CDF Note 7648, (2005).

[51] G. Bolla *et al.*, Nuclear Instruments and Methods in Physics Research A **518**, 277 (2004).

[52] M. Weber and the CDF Run IIb Silicon Group, The CDF Run IIb Silicon Detector: Design, Preproduction, and Performance, CDF Note 7891, (2005).

[53] J. Mathews *et al.*, Bulk Radiation Damage in Silicon Detectors and Implications for SVX II, CDF Note 3408, (1995).

[54] S. Baroiant *et al.*, Selection of tau leptons with the CDF Run II trigger system, Nucl. Instrum. Meth. A 518:609-611, 2004.

[55] S. Tsuno and A. Thompson, LesHouchesModule: A CDF-interface module for Les Houches Accords, CDF Note 6333,, (2003).

[56] T. Sjöstrand *et al.*, High-Energy-Physics Event Generation with PYTHIA 6.1, 2000.

[57] V. Martin, High-Pt Muon ID Cuts and Efficiencies for use with 5.3.1 Data and 5.3.3 MC, CDF Note 7367, (2005).

[58] J.-F. Arguin *et al.*, Generic Jet Energy Corrections for Run II data used for the Winter Conferences, CDF Note 6280, (2003).

[59] C. Hill, J. Incandela, and C. Mills, Electron Identification in Offline Release 5.3, CDF Note 7309, (2004).

[60] T. Akimoto *et al.*, Electron ID Efficiencies for Intermediate p_T Using Upsilon $\rightarrow$ e+e- Events, CDF Note 7713, (2005).

[61] V. Martin, High-Pt Muon, recommended cuts and efficencies for release 5.3, CDF Note 7031, (2004).

[62] M. P. Giordani and S. Lammel, Dilepton Triggers for Exotic Searches at CDF II, CDF Note 6074, (2002).

[63] S. Baroiant *et al.*, Measurement of Level 3 Trigger Efficiency for 8 GeV Inclusive Electron Trigger Using Conversions, CDF Note 6324, (2003).

[64] S. Baroiant *et al.*, Measurement of Electron Trigger Efficiencies for Level1 and Level2 8 GeV Triggers, CDF Note 6257, (2003).

[65] A. Anastassov *et al.*, Muon Trigger Efficiencies for v5.3 Tau Data, CDF Note 7837,, (2005).

[66] S. Baroiant *et al.*, XFT Efficiency for the Isolated Track Leg of the Electron+Track Trigger, CDF Note 6510, (2003).

[67] S. Baroiant *et al.*, Lepton+Track Triggers: Measurement of the Level 3 Trigger Efficiency for Taus, CDF Note 6553, (2003).

[68] S. Baroiant *et al.*, Measurement of the Z $\rightarrow$ tau tau Cross-Section -Electron Channel, CDF Note 6552, (2005).

[69] M. Griffiths, B. Heinemann, and G. Manca, Fake Rate For Low-p_T Leptons, CDF Note 7470, (2005).

[70] S. Tourneur and A. Savoy-Navarro, A method to estimate the tau fake rate: from dijet to W+jets, CDF Note 8208, (2006).

[71] S. Baroiant *et al.*, Understanding the $Z^0 \rightarrow \tau_e\tau_h$ Signal in Run II Data: Backgrounds, CDF Note 6498, (2003).

[72] E. Halkiadakis, C. Hays, M. Tecchio, and W. Yao, A Conversion Removal Algorithm for the 2003 Winter Coferences, CDF Note 6250, (2003).

[73] D. Gerdes, Study of Conversion Removal For the Leptons + Jet Sample, CDF Note 2903, (1994).

[74] For sources used in luminosity uncertainty, see:
http://www-cdf.fnal.gov/ koningb/lum_official_page.html and
http://www-cdf.fnal.gov/ koningb/TotalLumUncertainty-04-09-15.pdf.

[75] S. Rolli *et al.*, Search For First GenerationScalar Leptoquarks, CDF Note 7181, (2004).

[76] D. Tsybychev, Search For First Generation LeptoQuarks In The Jet and Missing Transverse Energy Topology In Proton-AntiProton Collisions At Center-Of-Mass Energy 1.96 TeV, (Ph.D diss., University of Florida, 2004.).

[77] D. Ryan, Direct Searches for Scalar Leptoquarks at the Run II Tevatron, (Ph.D. diss., Tufts University, 2004.).

[78] See http://cdfrh0.grid.umich.edu/%7Emiller/pdf/pdf-acceptance.html.

[79] O. Gonzales and C. Rott, Uncertainty due to the PDFs for the gluino-sbottomsearch, CDF Note 7051, (2005).

[80] T. Baumann, M. Franklin, C. Gay, and J. Troconiz, Search for Third Generation Leptoquarks in the DiTau + DiJet Channel, CDF Note 3597, (1996).

[81] D. Acosta and S. Blessing, Ann. Rev. Nucl. Part. Sci. **49**, 389 (1999).

[82] V. A. Mitsou, N. C. Benekos, I. Panagoulias, and T. D. Papadopoulou, Czech.J.Phys. 55 (2005) B659-B666 .